UNIVERSIDADE DE LISBOA
FACULDADE DE CIÊNCIAS

Nucleon knockout of 11Be
from the collision with a proton target at high energies

Doutoramento em Física

Ana Isabel Martinho Henriques

Tese orientada por:
Professor Doutor Daniel Galaviz
Professora Doutora Raquel Crespo

Documento especialmente elaborado para a obtenção do grau de doutor

2017

UNIVERSIDADE DE LISBOA
FACULDADE DE CIÊNCIAS

Nucleon knockout of 11Be from the collision with a proton target at high energies

Doutoramento em Física

Ana Isabel Martinho Henriques

Tese orientada por:
Professor Doutor Daniel Galaviz
Professora Doutora Raquel Crespo

Júri:
Presidente:
- Doutor José Manuel de Nunes Vicente e Rebordão

Vogais:
- Doutora Manuela Rodriguez Gallardo
- Doutor Thomas Aumann
- Doutor José Pedro Miragaia Trancoso Vaz
- Doutor Luís Filipe dos Santos Garcia Peralta
- Doutor Daniel Galaviz Redondo

Documento especialmente elaborado para a obtenção do grau de doutor

2017

To my family
Laura, António e João

Abstract

The special features of the ^{11}Be neutron halo, a closed shell structure with an additional loosely binded neutron, allows us to study the neutron knockout of loosely bound valence and deeply bound nucleons. The neutron breakup of the ^{11}Be halo nucleus has been studied in inverse kinematics at the R3B/LAND setup at the GSI-Helmholtz Centre for Heavy Ion Research (Darmstadt, Germany).

The different detectors placed at the R3B/LAND setup allow to measure position, energy loss and time of flight, before, around and after the target, allowing to characterize the projectile and heavy reaction fragment. Surrounding the target the Crystal Ball 162-NaI crystal array is used for γ ray and proton detection in its forward hemisphere.

This work considered two analysis procedures related with the detected particles emerging from the collision process: (i) particle inclusive neutron knockout where only the heavy fragment is detected, ^{11}Be(p,X)^{10}Be; (ii) particle exclusive neutron knockout where the light particles and heavy fragment are detected, ^{11}Be(p,pn)^{10}Be.

For the particle knockout study the momentum width FWHM was determined (44.0±2) MeV/c for the CH_2 target, and after the proper background subtraction, the cross section was obtained for a proton target, (52±5) mb. The second approach considered the neutron knockout measured in coincidence with two nucleons, in the high energy branch of Crystal Ball. The measured reaction cross section is (37±15) mb, considering a detection efficiency of (15.2±6.1)%, provided by simulations.

The measured and calculated cross sections were compared using the Faddeev/AGS reaction formalism assuming that other channels are negligible. This interpretation allowed to evaluate the contribution from the valence and deeply bound nucleon knockout, for both particle inclusive and exclusive measurements.

In addition, the gamma spectrum of ^{10}Be was obtained for both analysis procedures. A significant signature of γ-rays stemming from the excitation of ^{10}Be is seen in the inclusive spectrum. It was also studied the effects of emitting the two nucleons in coplanarity. The results indicate that the reaction process has two clear and differentiable components.

Keywords: nuclear physics, halo nuclei, neutron knockout, cross section

Resumo

As características especiais do núcleo halo ^{11}Be, uma estrutura completa à qual está fracamente ligado um neutrão, torna este núcleo um caso interessante para estudar as contribuições da remoção de um neutrão fraca e fortemente ligado.

O estudo da remoção de um neutrão do núcleo halo ^{11}Be foi realizado em cinemática inversa no aparato experimental R3B/LAND no laboratório GSI-Helmholtz Centre for Heavy Ion Research (Darmstadt, Alemanha). Os detectores do setup experimental permitiram medir posições, energia depositada e tempo de voo, antes, depois e em torno do alvo. Em redor do alvo, o detector Crystal Ball, composto por 162 cristais de NaI permitiu detectar os raios gama e nucleões emitidos resultantes da reacção.

Neste trabalho a reacção em estudo foi abordada de duas formas distintas: (i) inclusiva, é identificando o fragmento pesado resultante da interacção do projéctil com o alvo, ^{11}Be(p,X)^{10}Be (ii) exclusiva, onde são adicionalmente detectados os fragmentos leves, ^{11}Be(p,pn)^{10}Be.

No estudo inclusivo, foi obtida a FWHM da distribuição de momento de (44±2) MeV/c para o alvo de polipropileno e (52±5) mb para a secção eficaz considerando um alvo de protões. A segunda abordagem considerou a detecção do fragmento em coincidência com os dois nucleões na Crystal Ball, obtendo-se uma secção eficaz de (37±15) mb para uma eficiência de detecção de (15±6)%.

As secções eficazes medidas foram comparadas com os valores obtidos através de cálculos utilizando o formalismo de reacções Faddev/AGS, assumindo que apenas o canal de knockout é relevante. A interpretação dos resultados permitiu avaliar a contribuição da remoção de um neutrão de uma camada de valência ou interior para ambas as análises consideradas.

O espectro gama do ^{10}Be foi estudado para ambas as análises. Verificou-se um maior número de contagens relevantes no espectro inclusivo. Adicionalmente, foi estudado o contributo para este espectro de eventos em que os nucleões são emitidos segundo o mesmo plano. Os resultados mostraram que existem duas componentes distintas no processo de reacção.

Palavras chave: física nuclear, remoção de neutrão, knockout, halo

Contents

List of Figures

List of Tables

Abbreviations

ADC	**A**nalog to **D**igital **C**onverter
ALADIN	**A L**arge **DI**pole mag**N**et
DAQ	**D**ata **A**c**Q**uisition
DSF	**D**own **S**cale **F**actor
FRS	**FR**agment **S**eparator
GFI	**G**roess **FI**iber Detektor
INCL++	Liège **I**ntranuclear **C**ascade
LAND	**L**arge **A**rea **N**eutron **D**etector
PSP	**P**osition **S**ensitive **P**in diode
POS	**PO**sition detector
QDC	Charge to **D**igital **C**onverter
QFS	**Q**uasi **F**ree **S**cattering
R3B	**R**eactions with **R**elativistic **R**adioactive **B**eams
SCI	**SCI**ntillators present at the FRS
SIS18	GSI Heavy Ion **S**ynchrotron
SST	**S**ilicon **S**trip **T**racker
TDC	**T**ime to **D**igital **C**onverter
TFW	**T**ime of **F**light **W**all
tof	**t**ime **o**f **f**light
UNILAC	**UNI**versal **L**inear **AC**celerator

Chapter 1

Introduction

The ^{11}Be halo is an unique nucleus. Provided by a closed shell structure, with an additional loosely bound neutron, it allows to investigate simultaneously the dominant reactions mechanisms for the knockout of loosely bound valence and deeply bound nucleons. In this work we shall present the first experimental comparison between total cross sections and momentum distributions for particle inclusive (where only the heavy fragment is measured) and particle exclusive (measuring in addition the emitted light fragment) analysis.

This first chapter introduces the main concepts of the physics behind the study of halo nuclei and focuses in ^{11}Be, a one neutron halo nucleus.

The chapter starts with a brief description of the nuclear properties such as the mass and therefore, the binding energy. The concept of dripline in the nuclear chart where the so-called exotic nuclei are located will be introduced. Aiming to reproduce the nuclear properties, nuclear models were developed. It should be highlighted that the models failed to describe the properties of the nuclei encountered at the driplines. As a matter of fact, the properties seen in stable nuclei change for exotic nuclei. Structure nuclear models and its shortcomings are briefly described.

Of particular interest found at the driplines are the halo nuclei such as ^{6}He, ^{11}Li, ^{11}Be and ^{15}C. The features of these quantum systems are covered as well as the tools that have been used to probe them. Particular focus is then given to ^{11}Be, the nucleus of interest in this study, and the studies that have been performed to reveal its properties.

Finally, it is introduced how this work aims to contribute to gain further insight to the structure of ^{11}Be by means of the study of the collision with a proton target at high energies.

1.1 The atomic nucleus

The birth of Nuclear Physics can be attributed to the discovery of radioactivity by Becquerel in 1896, or to the discovery of the atomic nucleus by Rutherford in 1911 [1]. Since then many atomic nuclei have been studied.

The atomic nucleus is defined by its number of protons and atomic mass number, the sum of protons and neutrons, and described by different properties: mass, radius, relative abundance, decay mode, half-life, magnetic and electric moments, spin and excited states.

Nowadays, the known nuclear chart, presented in Figure 1.1, includes around 2900 different nuclei. In this chart, nuclei are presented according to their number of protons and neutrons.

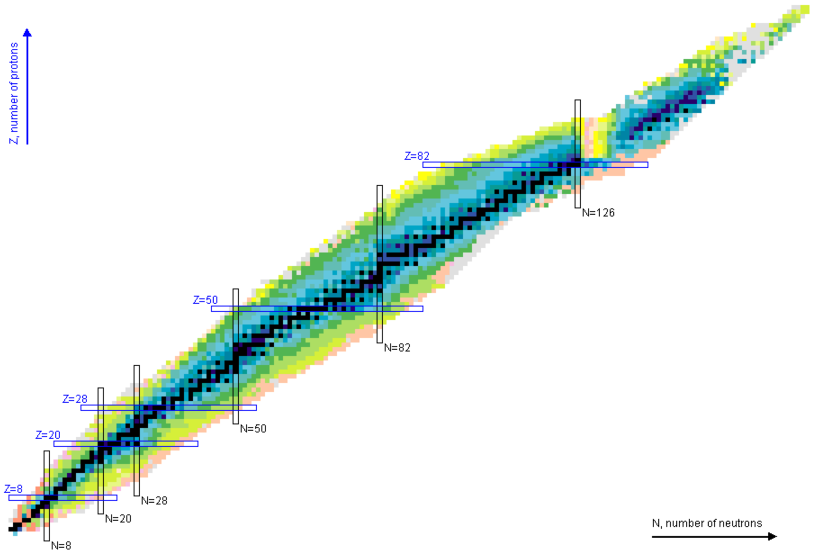

FIGURE 1.1: Chart of nuclei presenting the number of protons (vertical) versus number of neutrons (horizontal). The different colors represent different scales of half-life of the nuclei. The black squares are stable nuclei and form the β valley of stability [2].

The limited number of nuclei that are long-living isotopes are presented as black squares and form the β valley of stability. To the left of the valley are neutron deficient nuclei which mostly decay by β^+-decay, α-decay (dominant for nuclei with a large number of protons and neutrons) and electron capture. On the other side of the valley are nuclei that contain an excess of neutrons and decay mainly by β^--decay or spontaneous fission.

The stability of nuclei is related to the forces binding the nucleons (protons and neutrons) together. The nucleons interact mainly through strong (nuclear) interaction. This interaction is attractive at the internucleon distance and becomes less significant when nucleons are femtometers apart. The repelling Coulomb interaction that governs the interaction between protons makes the number of protons smaller than the number of neutrons in the nucleus, in particular for heavy nuclei. In addition, the nucleus is a quantum mechanical system and according to the Pauli and uncertainty principles cannot exhibit a very dense configuration.

The density of a nucleus is closely tied to its radius. The nuclear radius and the nuclear potential follow a similar spatial description: constant over short distances after which it drops rapidly to zero. The measurement of the radius is not trivial and depends on the experiment. In fact, different experiments addressed the nuclear charge and matter distributions. Nevertheless, the matter and charge radii, R, reveal a dependence $R = 1.1 \cdot A^{1/3}$ for stable nuclei.

Another properties of nuclei are the mass and binding energy. These two properties are tied together in the semiempirical mass formula $m(N, Z) = N\, m_n + Z\, m_H - \frac{1}{c^2}B(N, Z)$, where N and Z and the number of neutrons and protons, respectively, $m(N, Z)$ is the atomic mass, m_n and m_H the neutron and hydrogen masses and $B(N, Z)$ the binding energy. In a rough description the binding energy is the energy gained by the nucleus for keeping the nucleons together. Considering the nucleus an homogeneous sphere, like a drop, the binding energy expression is given by five terms:

$$B = a_v A - a_s A^{2/3} - \frac{1}{2} a_{sym} \frac{(N-Z)^2}{A} - \frac{3}{5} \cdot \frac{Z^2 e^2}{4\pi\epsilon_0 R_c}$$

The first term, $B_v = a_v A$, where a_v is a constant, results from the attractive behaviour of the strong force and implies that each nucleon interacts with its nearest neighbours. The second term, $B_s = a_s A^{2/3}$, proportional to the surface area and where a_s is a constant, reflects the contributions of nucleons at the surface of the nucleus, surrounded by fewer neighbours. The following term, $B_{sym} = \frac{1}{2} a_{sym} \frac{(N-Z)^2}{A}$ accounts for nucleon pairing as nuclear forces favor equal number of protons and neutrons. Finally, the last term reflects the electrostatic energy of a charged sphere of radius R_c and takes into account the repulsion between protons.

The neutron separation energy (S$_n$) is the energy required for neutron removal from a nucleus and accounts the difference in binding energy between the initial and the final nucleus. The same concept is applied for protons, and is defined as the proton separation energy (S$_p$). These concepts help to define the boundaries of the nuclear chart in Figure 1.1. The neutron dripline can be defined as

$$\left(\frac{\partial B}{\partial N}\right)_{Z=const} = 0$$

and represents the heaviest isotope attainable with Z being constant. Similarly for the proton dripline one has $\left(\frac{\partial B}{\partial Z}\right)_{Z=const} = 0$.

It is at the neutron dripline, that neutron rich exotic nuclei can be found, and among them the nucleus of interest for this work, ^{11}Be. This region of the nuclear chart is very interesting as it allows to study the properties that are well established for stable nuclei and to check its validity at the neutron dripline.

The features of the different nuclear properties are taken into account in the nuclear structure models. These aim to reproduce the already known properties and predict new ones.

Nuclear Structure Models

To obtain precise information of the energy associated with every nucleon the Schroedinger equation must be solved. The time-dependent Schroedinger equation for a single non-relativistic particle and a central interaction is shown in Equation (1.1).

$$i\hbar\frac{\partial}{\partial t}\psi(\mathbf{r},t) = \left[-\frac{\hbar^2}{2m}\frac{\partial^2}{\partial x^2} + V(\mathbf{r})\right]\psi(\mathbf{r},t), \tag{1.1}$$

Solving the Schroedinger equation for nuclei with a considerable amount of nucleons is very challenging as the number of variables describing position and momentum escalates quickly and it becomes a complex mathematical problem with increasing mass number. In addition, the exact nature of the nuclear force is unknown, represented in Equation (1.1) in the nuclear potential, $V(\mathbf{r})$, the second term of the Hamiltonian.

Instead of determining the exact solution considering all individual nucleons and their description, several nuclear models were proposed. These models fall into two major categories, the shell and the collective description of the nucleus. Any of the models needs to reproduce the already known nuclear properties such as radius and binding energies and also to predict new ones.

In 1936, H. Bethe and R. Bacher [3] proposed the liquid drop model in which the nucleus was described as a drop of incompressible matter binded by the nuclear force. Such model was able to explain the density of the nucleus and its binding energy. However, the liquid drop model failed to describe the existence of favored combinations of number of protons and neutrons in the nucleus, the so-called magic numbers (e.g Z or N= 2, 8, 20, 28, etc), first summarized by M. Goeppert Mayer [4]. These magic number nuclei exhibit high abundance and larger nuclear binding energy when compared to their neighbours and exhibit deviations from the predictions of the semiempirical mass formula. This clearly revealed the existence of a discretized structure of shells inside the nucleus.

Closely tied to the atomic physics shell model for electrons, the Nuclear Shell Model (SM) was first proposed for the nucleus by Ivanenko and Gapon in 1932 [5]. In this model each nucleon occupies a single-particle quantum state and moves independently under a central potential created by all other nucleons. This potential is known as mean-field potential.

The mean-field potential can be modelled, as a first approach, using the harmonic oscillator or a more realistic Woods-Saxon potential [6]. Considering a Woods-Saxon potential:

$$V(\mathbf{r}) = \frac{V_0}{1 + exp(\frac{\mathbf{r}-R}{a})}$$

where $a \approx 0.6fm$, $R \approx 1.2A^{1/3}$ and a central depth of $V_0 = -50$ MeV can be considered. The neutron single particle energy levels obtained with the Woods-Saxon and harmonic oscillator potentials are shown in Figure 1.2. These approaches quantized the energy states occupied by the nucleons following the Pauli's exclusion principle, and introduced the quantum numbers n and l (orbital and angular momentum, respectively) which are responsible for the degeneracy of the energy states.

The total number of nucleons required to fill up to a given level are presented in Figure 1.2. In this picture, N and l represent the radial and angular quantum number, respectively. The later is usually represented using spectroscopic notation, s, p, d, f, g, h, i and j for l=0, 1, 2, 3, 4, 5, 6 and 7, respectively. The spectroscopic notation came from the observations of the atomic spectral lines: s-sharp, p-principal, d-diffuse. The occupation number is given by $2(2l + 1)$ as each l value can have $2l + 1$ states and each state can have a proton or neutron with spin $\pm\frac{1}{2}$.

The Woods-Saxon potential gives the correct three first magic numbers (2, 8 and 20), however, it fails, to predict higher values. The inclusion of the spin-orbit coupling to the mean-field potential overcomes this issue [7].

The spin-orbit coupling includes in the potential the interaction between the orbital and the spin angular momentum. While in atomic physics the correction is small, in nuclear physics it has a significant impact and is responsible for the crossing over of energy levels into different shells. The spin-orbit coupling splits the $2(2l + 1)$ level into two levels which are labeled by $nl_{l+\frac{1}{2}}$ and $nl_{l-\frac{1}{2}}$. This effect can be seen on the right side of Figure 1.2 for the Woods-Saxon with spin-orbit potential.

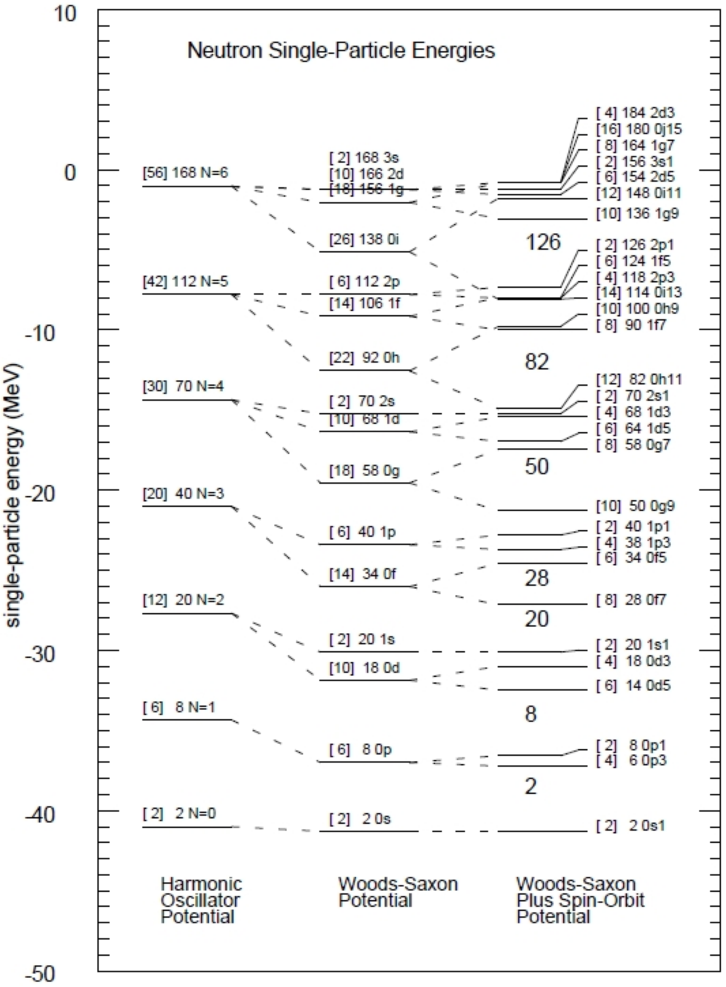

FIGURE 1.2: Neutron single-particle energy levels considering an harmonic oscillator, Woods-Saxon and Woods-Saxon with spin orbit coupling potentials. The spectroscopic notation is used to classify the different energy levels.

Nevertheless, the SM presented before is a simplified version, but is sufficient to predict the nuclear spin and parity, the magnetic dipole and electric quadrupole moments around the valley of stability.

Closer to the driplines where larger asymmetries of proton-neutrons exist, exotic nuclei reveal a structure that falls outside the mean-field description used in the SM [8, 9].

During the eighties, fast radioactive beams obtained from the fragmentation of heavy ions allowed the study of the evolution of shell properties of unstable nuclei by means of nuclear reactions [10, 11]. Far from stability new quantum features arise, leading to shifts and new order of the energy levels, some magic numbers even disappear and unexpected ones are revealed. This was verified when the number of neutrons N is equal to 20, and this region of the nuclear landscape is called the island of inversion [9]. The region where the neutron number is $N = 8, 14, 20, 28$ and 40 reveal a breakdown of the expected nuclear properties [12, 13].

When approaching the neutron driplines where the shell inversion can be observed, new quantum systems are found and among them the halo nuclei [14–17]. One of these halo nucleus is ^{11}Be which will be discussed in more detail in this chapter.

The study of shell properties can be achieved by means of nuclear reactions. In a nuclear reaction, two nuclei interact with each other, the projectile (a) impinges on another that is at rest, constituting the target (A). The reaction produces the residual particles b and B. Equation (1.2) presents the notation that is usually applied.

$$A + a \to B + b \text{ or } A(a, b)B \tag{1.2}$$

For simplicity, we shall use the same notation for both direct and inverse kinematics.

This work focuses on direct reactions. These reactions are peripheral, with large impact parameters and usually involve one or two nucleons. These are key reactions to study the shell structure of the nucleus [18, 19]. The following section is dedicated to these reactions.

1.2 Direct Reactions

Since their first use in the 1940's, direct reactions have been carried out to probe the single particle components of the nuclear wave function. Direct reactions are rather peripheral reactions, mostly surface dominated. In fact, only a few nucleons participate in the reaction and the other nucleons are spectators [18, 19]. One can identify several main processes of direct reactions: elastic, inelastic, transfer and knockout [20].

- Elastic scattering: the projectile (a) and target (A) suffer no internal change and there is no energy release due to the reaction process.
- Inelastic scattering: this reaction leaves one or all the fragments (b and B) in an excited state. The energy released in such reactions corresponds to the energy required for the excitation
- Transfer: a nucleon or a cluster is transferred from the projectile to the target or from the target to the projectile. In these reactions the projectile has a relatively low energy (in the range 20-30 MeV/nucleon).

- Knockout reactions: in this reactions one nucleon or a light cluster is removed from the projectile, rather than the addition and usually involve the interaction with light targets. These reactions are very powerful tool in structure studies [19]. This type of reaction is more relevant to this study and therefore, it will be presented in more detail.

1.2.1 Nucleon Knockout

The study of knockout reactions provides insight on the properties of the removed nucleon in the process, such as its angular momentum.

The extraction of shell structure information from these reactions with light targets, have been often analyzed using the Glauber reaction framework that relies upon the eikonal and the adiabatic approximation. The adiabatic is assumed to be valid when the energy of the projectile is very high compared with the internal motion of the nucleons. This motion can be disregarded and nucleons are considered *frozen*. This feature implies that, in the centre of mass, the momentum of the heavy fragment is equal, but with opposite direction, to the removed nucleon. Therefore, it allows to access the wave function of the removed nucleon, because the momentum distribution is related to the Fourier transform of the radial wave function. The radial wave function exhibits different shapes according to the orbital angular momentum. This follows Heisenberg's uncertainty principle. Thus, the lower the orbital angular momentum, the narrower is the momentum distribution.

The eikonal approximation entails that the resulting nucleus is not deflected and the reaction takes place at forward angles [18].

The knockout studies resulting from the collision with a light target, have been inclusive and include several components that contribute for the single-particle (sp) cross section, which is given by:

$$\sigma_{sp} = \sigma_{st} + \sigma_{dif} + \sigma_{Coul}$$

where σ_{st}, σ_{dif} and σ_{Coul} are the single-particle cross sections due to stripping, diffraction and Coulomb processes, respectively.

In the stripping process, also referred as inelastic breakup, the strucked nucleon interacts with the target, the former being scattered to large angles and leaving the target excited. Diffraction or elastic breakup refers to reactions where the removed nucleon is emitted at forward angles and leaving the target in the ground state. The

Coulomb dissociation refers to electromagnetic elastic breakup and is only relevant when heavy targets, such as lead, are used.

The total theoretical cross section, σ_{theo}, is standardly calculated as the sum all of *all bound* states, as shown in Equation (1.3).

$$\sigma_{theo} = \sum_{j} C^2 S(I_\pi, nlj)\, \sigma_{sp}(nlj) \tag{1.3}$$

where C^2S is the spectroscopic factor associated to the particle state, and therefore is the weight of a given configuration of the incident projectile ground state wave function.

The contributions to the single-particle states can be obtained experimentally from the measurement of the γ-rays originated from the deexcitation of the fragment, when measured in coincidence.

The ratio between the experimental (σ_{exp}) and theoretical (σ_{theo}) cross sections is defined as the reduction factor, R_s [17].

$$R_s = \frac{\sigma_{exp}}{\sigma_{theo}} \tag{1.4}$$

Its interpretation cannot be simply explained due to factors like correlations between three body forces and coupling to the continuum. From 1.3 the total cross section is the sum of all terms, therefore one cannot associate to a specific spectroscopic factor.

In particular, special attention must be paid if there is a sum of contributions as Equation 1.3. The departure of this reduction factor from unity can be evidence for the need of a revision of the reaction or nuclear structure model.

In summary, knockout reactions are very important in structure studies. Through the momentum distributions of the fragment and the cross-section of the reaction channel, it is possible to access the wave function of the projectile. In addition, the coincidence measurement of the fragment with γ-rays stemming from the fragment allows to determine the contribution of each single-particle state to the wave function of the projectile.

1.2.2 Quasi-free Scattering Mechanism

The quasi-free Scattering (QFS) reaction mechanism refers to the knockout of a nucleon or light particle from a nucleus resulting from the collision with a proton target. It consists of one of the most common experimental tool to study single-particle properties in nuclei [21, 22].

The kinematics of the quasi-free process, it is represented in Figure 1.3, where p, 1, 2, and 3 refer to the projectile, the removed nucleon from target and projectile and remaining part of the impinging particle, respectively. The target nucleus has initially A nucleons and A-1 nucleons in the end of the process. The strucked nucleons (1 and 2) are characterized by the corresponding polar (θ) and azimuthal (φ) angles. From these, one defines the opening angle ($\Delta\theta = \theta_1 - \theta_2$) and the azimuthal difference ($\varphi_{12} = \varphi_1 - \varphi_2$).

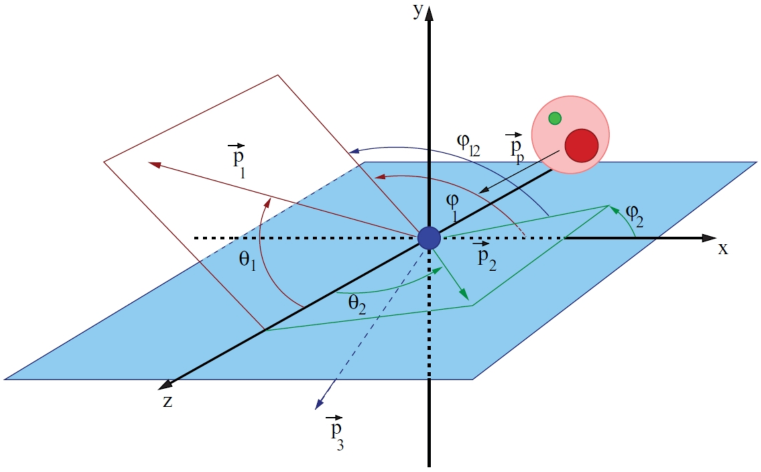

FIGURE 1.3: Kinematic angles in inverse kinematics for knockout reactions in the lab frame. The figure was extracted from [23].

In such reaction mechanism, the interaction between the projectile and the target is expected to be dominated by free nucleon-nucleon (NN) scattering, and thus, one expects an azimuthal coplanar scattering and an opening angle between the knockout particle and proton close to 90°.

In 1952 at the Berkeley Laboratory, the first quasi-free scattering reaction mechanism was observed in direct kinematics by O. Chamberlain and E. Segré [24]. In this experiment a light lithium target was bombarded with a proton beam of 350 MeV. After the reaction two protons emerged with an opening angle of approximately 90°. This angular correlation is expected if both protons (the projectile and the knockout proton from the nucleus) are considered as free particles. In fact, the opening angle is not exactly 90°. This can be explained with the fact, that the removed proton which is part of a nuclear system in which the proton is not at rest but has a momentum distribution [24, 25].

The knockout reaction in which the QFS is the dominant mechanism is a powerfull tool to study the nuclear structure of the nucleus. In particular to study the validity of the mean field shell model approach. Besides the angular correlations, there is an energy correlation associated with the binding energies of the nuclear shells [25].

1.3 Halo Nuclei

In the mid-eighties, the development of radioactive beam facilities allowed the study nuclei far from stability. Although the proton dripline is experimentally known, the location of the neutron dripline is only known for light nuclei. It is on this part of the nuclear chart that we can find the one-neutron halo nucleus ^{11}Be. Other examples of neutron halo nuclei are ^{6}He (2-neutron halo), ^{11}Li (2-neutron halo), ^{19}C (1-neutron halo).

The inclusion of more neutrons in a nucleus can result in a loosely bound neutron system with singular features. Due to tunneling effects, the wave function of the loosely bound neutrons extends to classical forbidden regions, forming a halo structure around a well-defined core. In other words, halo nuclei are spatially large systems, their radius of interaction does not follow the $R = R_0 A^{1/3}$ behaviour, revealing a considerable larger radius compared to their closest bound neighbours. Many review articles have summarized properties and probing tools of halos [26–34].

In 1985, Tanihata [14] observed for the first time evidence of the ^{11}Li 2-neutron halo nucleus. The term “neutron halo” was introduced by P. Hansen and B. Johnson. In [15], they established the connection between the halo neutron long density distribution and the small neutron binding energy.

The theoretical description of a halo can be simply put in terms of a potential model. Considering a nucleus with one loosely bound neutron and disregarding the spin orbit interaction, the wave function of the neutron outside a potential of width R is given by:

$$\psi(r) = \left(\frac{2\pi}{k}\right)\left(\frac{-e^{kr}}{r}\right)\left(\frac{e^{kr}}{(1+kR)^{1/2}}\right)$$

Keeping in mind $\rho(r) = |\psi(r)|^2$, at larger distances (r) of the centre of the nucleus, the density distribution, for a neutron outside a square potential well, has an exponential behaviour

$$\rho(r) \propto \frac{e^{-2k}}{r^2}$$

where the parameter k determines the slope of the tail of the distribution and is related to the neutron separation energy (S_n) and effective mass (μ) by

$$(\hbar k)^2 = 2\mu S_n$$

While for stable nuclei $S_n \sim 6-8$ MeV, in neutron halos, S_n must be small because of the large radius like proposed by [15]. In another way, when S_n decreases k becomes smaller and thus, the tail of the density distribution becomes larger.

The momentum distribution, f(p), of the neutron is expressed by the Fourier transform of the wave function:

$$f(p) = \frac{C}{p_i^2 + k^2}$$

where p_i is the Cartesian components of the momentum. The distribution shows a dependence with k. In contrast with the density distribution, the smaller the neutron binding energy S_n, the smaller the width of the distribution. This is due to the Heisenberg principle, when the distribution in coordinate space is wide, in momentum space is narrow.

In addition, the slope of the density distribution depends on the orbital angular momentum. Longer tails correspond to lower orbital angular momentum. The later occurs because high angular momentum states (l≠0) will contribute to a centrifugal potential that pushes the halo particle(s) inside the core [27, 30, 34].

Several experimental measurements have shown evidence of the exotic structure of halo nuclei. The following paragraphs describe some key features of halo nuclei focusing on neutron halos.

- Interaction cross sections

  The interaction cross section was the first observable to be measured in halos and clearly showed an enhancement for these nuclei [14]. Such enhancement can be explained due to the dominant contribution of the NN interaction, in opposition to compact systems in which the nucleons “shadow” each other and exhibit smaller cross sections [32]. It was due to these measurements that halo radii was extracted [14, 35, 36].

- Ground state properties

  Mass measurements are of particular interest because they provide information on the binding energy of the last nucleon. In the case of halo nuclei the binding energy is very low, below 1 MeV. The masses of halos were first measured by means of nuclear reactions and more recently using penning traps [37], which achieved higher precision measurements [38].

  The measurement of interaction cross sections allows to determine the nuclear size of unstable nuclei, i.e the mass and charge distributions. The difference between these distributions for neutron halos indicate the presence of extended matter distribution beyond the charge radius. Figure 1.4 shows the increase of the root mean square (rms) radius for ^{11}Li when compared to its neighbours [14]. This type of measurement is very important to the characterization of the core [35, 36].

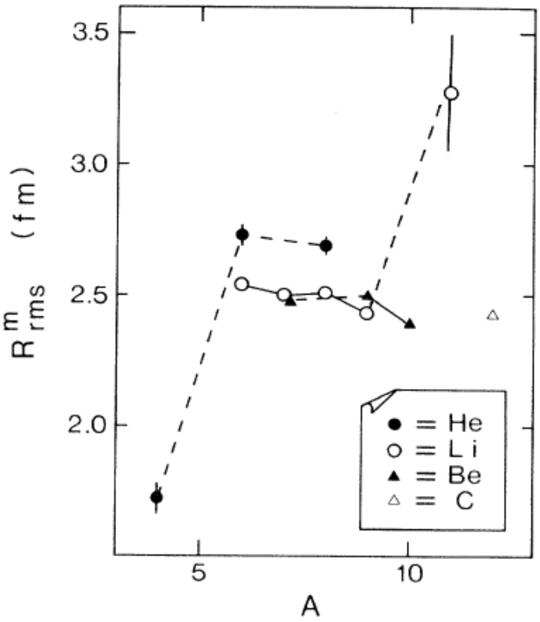

FIGURE 1.4: Matter rms radius for several neutron rich nuclei (He, Li, Be and C). A larger radius is observed for the ^{11}Li nucleus [14].

One must also mention the existence of other systems that also reveal an asymmetry between matter and charge distributions, the so-called neutron skins. There are several definitions for these systems, however they have a larger number of neutrons than halos and show an abundant distribution of neutrons at the nucleus surface.

The magnetic dipole and electric quadrupole moments have also been studied for halo nuclei. The magnetic moment should reflect the configuration of the ground state wave function. The presence of the intruder $2s_{1/2}$ into the p-shell for the ^{11}Be halo nucleus has been shown in the work of [39]. This is a novel feature from what is expected from the SM picture.

- Beta decay

  Beta decay can provide information on nuclei far from stability. It gives complementary information to other studies [40–42]. At the dripline the mirror transitions expected for the beta decay have different strengths, e.g. ^{9}C and ^{9}Li. According to the reduced Gamow-Teller matrix element for the beta transition, the decay strength is related to the spectroscopic configuration of the initial and final particle state.

- Breakup reactions and momentum distributions

  Due to their weakly bound nature, halo nuclei are easy to breakup and often used to study these weakly bound systems [27, 32]. In addition, the measurement of momentum distributions of the fragments resulting of the breakup provide a well-established method to study halo nuclei [43–45]. These distributions can be either transverse/perpendicular or longitudinal/parallel to the beam direction. They characterize the properties of the halo nucleus [28].

- Electromagnetic processes

  Coulomb or electromagnetic dissociation reactions consist on an important tool to study halo nuclei. The description of the electromagnetic transitions have a dependence on the core-halo distance [31, 32]. In addition, they can be used as a spectroscopic tool as described in [46].

  Electromagnetic dissociation occurs when the virtual photon field, created by the target, excites the projectile leading to its breakup. The interaction cross section of such process revealed an enhancement for nuclei with a smaller separation energy of the last neutron [47], as this is the case of halo nuclei. Also, heavy targets were shown to be more favourable to reveal this enhancement [48]. This phenomena was observed for several halos, such as ^{11}Li, ^{11}Be, ^{15}C and ^{19}C [46, 48, 49].

One-neutron halo ^{11}Be

We now discuss in particular the ^{11}Be nucleus which will be studied in the present work.

^{11}Be has 4 protons and 7 neutrons and is located at the right side of the β-stability valley where neutron rich nuclei can be found, shown in Figure 1.5.

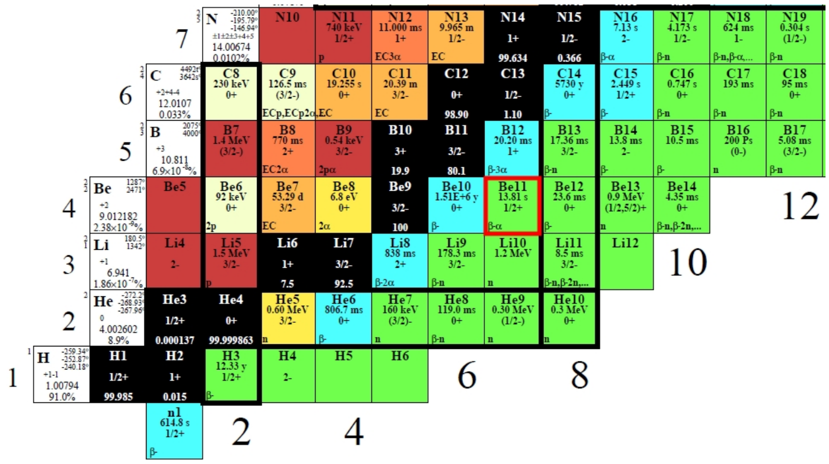

FIGURE 1.5: Low mass region of the nuclear chart highlighting the 1n-halo ^{11} [50]

As mentioned previously, when approaching the driplines the shell gaps change. This is clear when analysing the ^{11}Be 1n-halo ground state. For this nucleus, within a shell model picture, it is expected that the 7^{th} neutron occupies the $p_{1/2}$ orbit, however this is not the case. The ground state of ^{11}Be contains a dominant contribution of one neutron on the s-orbit ($J^{\pi} = 1/2^{+}$) due to an inversion between the $s_{1/2}$ and $p_{1/2}$ levels. Therefore, as the $1p_{1/2}$ exhibits a higher energy a shell gap appears at N=6 (according to standard shell model this would be at N=8). This feature provides ^{10}Be with a closed shell structure, with an additional loosely bound neutron in a s-shell forming the 1n-halo ^{11}Be.

As expected of a halo nucleus, ^{11}Be revealed a small neutron separation energy, an extremely strong E1 transition [51], a large matter radius [52], large interaction [52, 53] and Coulomb dissociation cross sections [46, 54, 55] and narrow momentum distributions for breakup reactions [56–58].

The 1n-halo ^{11}Be nucleus became of interest due to its simplified structure when compared to 2n-halos such as ^{11}Li. Throughout the years many experiments and theoretical works have been devoted to the study of the properties of the ^{11}Be nucleus considering different beam energies, reaction targets and observables. A list of the experimental studies performed is presented in Appendix A.

The 1n-halo ^{11}Be nucleus is assumed to be well described by a dominant contribution of ^{10}Be core, in its ground state, and a valence neutron in a 1s shell with a separation energy of 501.6 keV. There is also a significant core excited component, ^{10}Be(2^{+}) coupled a to neutron on an $0d_{5/2}$ orbital. The ^{11}Be ground state wave function can be written as:

$$\left|{}^{11}Be_{gs}\right\rangle_{1/2^{+}} = \alpha \left|{}^{10}Be(0^{+}) \otimes \nu 2s_{1/2}\right\rangle + \beta \left|{}^{10}Be(2^{+}) \otimes \nu 1d_{5/2}\right\rangle_{1/2^{+}} . \tag{1.5}$$

This description was proposed due to the observed narrow distribution of the ^{10}Be fragment resulting from the one-neutron knockout of ^{11}Be [56].

First evidence of core excitations in the breakup of ^{11}Be were found recently [59, 60]

Another interesting fact about ^{11}Be is the one bound excited state ($J^{pi} = 1/2^{-}$) due to the population of a p-shell which lies at 320.0 keV, bellow the 501.6 keV neutron separation energy.

$$\left|{}^{11}Be^{*}\right\rangle_{1/2^{-}} = \gamma \left|{}^{10}Be(0^{+}) \otimes \nu 1p_{1/2}\right\rangle_{1/2^{-}} \tag{1.6}$$

The spectroscopic factors (α, β an γ) quantify the admixtures of the different valence orbits. A selection of experimental and theoretical values of spectroscopic factors for the ground state and excited states of ^{11}Be can be found in [61]. Also [62] presents a systematic collection of the spectroscopic determined for the $\left|^{10}Be(0^{+}) \otimes \nu 2s_{1/2}\right\rangle$ component. In any case, the configuration of the ground state of ^{11}Be is very ambiguous, the theoretical and experimental results range from 0.4 to 0.9 depending on the reaction study performed and theoretical interpretation.

The one-neutron knockout of ^{11}Be on a Be target, at a mid-target energy of 60 MeV/nucleon shed some light on this subject [57]. The results supported the description of ^{11}Be ground state given in Equation (1.5), i.e the wave function of the ground state of ^{11}Be has two components, both considering a ^{10}Be core coupled to a neutron in a different state. In this representation, each component is weighted by α and β and according to [57], these were evaluated to be 0.85 and 0.15, respectively.

Nevertheless other experiments aiming to obtain the spectroscopic factors of the ground state took place [62, 63] and revealed different values.

1.4 This Work

Up to now the 1n-halo nucleus ^{11}Be has been studied using light and heavy targets, mostly at mid range energies. In this work we aim to study the knockout of valence and inner shells neutrons from the interaction with a proton target at high energies. This measurement also aims to shed light on the reaction mechanism. With such purpose, the study of the ^{11}Be(p,pn)^{10}Be reaction was performed in inverse kinematics at 457 MeV/u at the the GSI laboratory [64].

The S393 experiment [65] was carried at the R^{3}B setup [66], in the Summer of 2010, at the GSI Helmholtzzentrum für Schwerionenforschung in Darmstadt, Germany. In this experiment neutron rich nuclei, ranging from 4<Z<10 and 1.5< $^{A}/_{Z}$ <3, were studied through different reaction channels. Different targets (Pb, CH$_2$, C) were also used in order to investigate different reaction channels. Several of the large number of nuclei produced during S393 have been studied, and first results have been published [67–73].

This thesis has been organized in six different chapters. After describing the theoretical concepts of experimental techniques used to investigate the structure of the atomic nucleus and presenting the key features of halo nuclei, in particular of ^{11}Be, chapter 2 introduces the experimental setup. This chapter describes mainly the R^{3}B experimental setup and also the GSI facility, providing particular information for the S393 experiment. The third chapter contains the calibration procedures performed on the obtained data by the author. This work was mainly on the beam diagnostic detectors and the Silicon array surrounding the target. Chapter 4 contains the analysis procedures followed. Chapter 5 presents the simulations that were carried out to study signatures of the response to protons and neutrons in the Crystal Ball detector, and also an efficiency study for the (p,pn) reaction. The last chapter presents the results as well as their interpretation, focusing on the comparison between total cross sections and momentum distributions for particle inclusive and particle exclusive knockout reactions.

Chapter 2

Experimental Apparatus

The experimental proposal entitled “Neutron-rich nuclei at and beyond the dripline in the range Z=4 to Z=10, studied in kinematically complete measurements of direct reactions at relativistic energies” [65] was approved by the Proposal Advisory Committee (PAC) of the GSI Helmholtzzentrum für Schwerionenforschung GmbH [64] and received the acronym S393 which will be used from now on.

The S393 experiment was performed at the GSI laboratory during August and September 2010. The experimental campaign aimed at studying light neutron-rich nuclei (Z=4 to Z=10) using inverse and complete kinematic measurements at relativistic energies. One of the main physics topics was the study of knockout reactions to investigate the evolution of shell structure close to and beyond the dripline. During the 21 days of experiment, data were recorded at the LAND/R^{3}B setup acronyms for Large Area Neutron Detector and Reactions with Relativistic Radioactive Beams.

In this chapter, it is described the experimental facility and setup used. The description is focused on the S393 experiment and therefore the examples given are for this experiment. Nevertheless, other situations are also feasible at this facility. First, it will be given an overall description of the setup in order to provide the reader with the general idea of the setup. Following this superficial description, is a detailed description of the detector systems used in the experimental hall.

2.1 The GSI accelerator facility

The GSI laboratory is located in Darmstadt, Germany. This heavy ion accelerator facility strives to study and comprehend nature through the production of beams of stable and exotic nuclei at velocities close to the speed of light. The research fields cover nuclear and atomic physics, plasma, materials research, biophysics and cancer therapy [64].

At the GSI accelerator, it is possible to prepare ion beams of all elements, up to and including uranium and accelerate them to a significant fraction of the speed of light. A schematic view of the of the facility is shown in Figure 2.1.

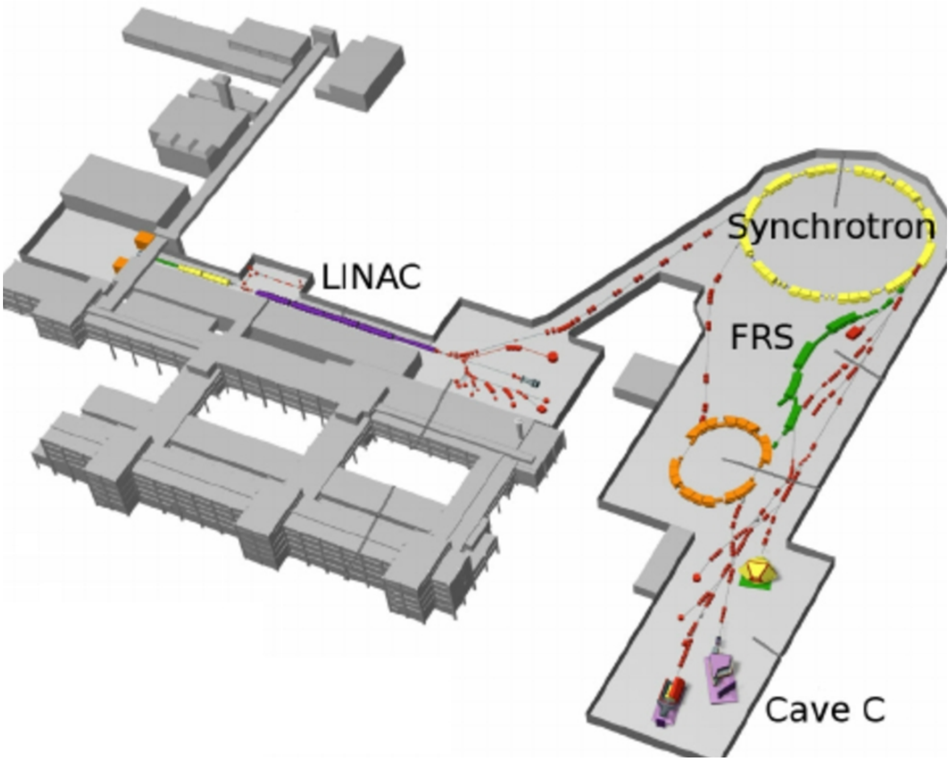

FIGURE 2.1: GSI accelerator facility. Ion beams are produced at the ion source and accelerated by the LINear ACcelerator UNILAC . These are used for low energy experiments or injected into the SIS18 synchrotron to be further accelerated. Fragmentation on a primary target produces radioactive ions. From the FRS the beam can be delivered to several experimental halls in the case of experiment S393, CAVE C.

A primary beam is produced in one of the available ion sources and delivered to the linear accelerator, the so-called UNILAC (UNIversal Linear ACcelerator). In the case of the S393 experiment, the primary beam was ^{40}Ar. After being accelerated up to 18 AMeV, the primary beam was injected into the GSI Heavy Ion Synchrotron, the SIS18. In the synchrotron, ions are accelerated up to 600 MeV/u to be then delivered to the FRagment Separator (FRS) [74]. The FRS is a high resolution forward spectrometer. Placed at its entrance is a Beryllium production target (4.011 g/cm^2) where the primary beam impinges. The fragments resulting from the nuclear fragmentation form the secondary beam, a relativistic beam of different stable and exotic nuclei with approximately 500 MeV/u. Figure 2.2 shows a schematic drawing of the FRS.

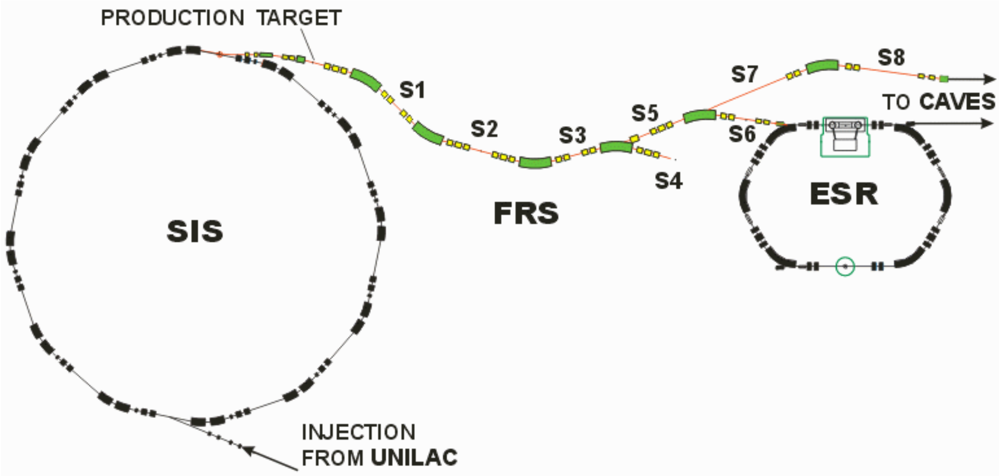

Figure 2.2: Fragment Separator. The ion beam from the SIS is fragmented on the primary target and the produced secondary ions are selected according to their magnetic rigidity through a set of magnetic dipoles.

In Figure 2.2 are drawn magnetic dipoles (yellow) and quadruples (green) that allow to deflect and focus the secondary beam. In addition, at the different S stations it is possible to perform position and time-of-flight (tof) measurements and there are also wedged-shaped degraders that slow down the fragments in proportion to the square of their nuclear charge.

The different isotopes present in the secondary beam are separated according to their mass-to-charge ratio (A/Q) by the FRS dipole magnets. In fact the charge (Q) can be replaced by the atomic number (Z), because all the isotopes are fully stripped. Different settings of the FRS allow to select nuclei of different regions of the nuclear chart.

The resulting *cocktail beam*, characterized by its A/Z ratio, is delivered to Cave C, the experimental hall of the LAND/R^{3}B setup .

2.2 The LAND/R^{3}B setup

The LAND/R^{3}B experimental setup was housed in Cave C and was used to study reactions in inverse kinematics on event-by-event basis. A schematic drawing of the setup is shown in Figure 2.3.

At the entrance of the experimental hall, the beam is characterized by several detectors which measure time, position and energy loss, allowing to distinguish the different nuclei present. These are the so-called beam diagnostic detectors. The first detector positioned along the beam line is the POS detector. This detector provides time information together with other time measurements from other scintillators upstream in the

FRS, which can be used to determine the tof of the incoming ions. The tof information is crucial to resolve the different nuclear masses present at the entrance of the setup. The active collimator ROLU (Rechts, Oben, Links, Unten) determines the beam spot size. After ROLU is the the Position Sensitive Pin diode (PSP) detector, a silicon detector. The energy deposited by an ion passing through PSP is related to the atomic charge of the nucleus by the Bethe-Block formula [75].

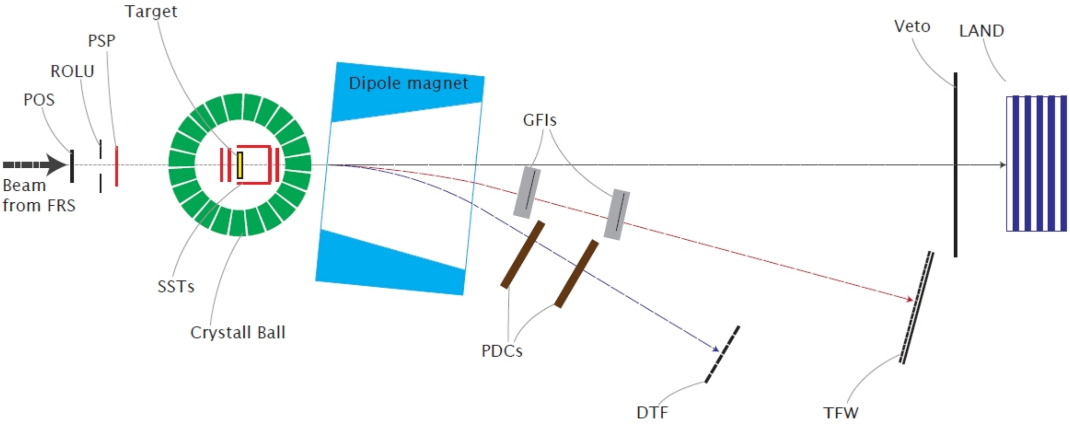

FIGURE 2.3: Schematic view of the LAND/R^{3}B setup for the S393 campaign. This setup performs reactions in inverse kinematics and aims to characterize all particles involved in the reactions.

The incoming beam impinges on the target, which is surrounded by the Crystal Ball [76], a 4π NaI gamma detector. This detector is also prepared to measure the energy deposit of scattered protons in its forward hemisphere, with respect to the beam direction. Enclosed by the Crystal Ball are eight Silicon Strip Detectors (SSTs) [77, 78] used to track charged particles.

After the collision with the target, the resulting fragments (mostly focused along the direction of the beam) will go through the dipole magnet ALADIN (A Large DIpole magNet) and will be deflected according to their magnetic rigidity into different branches.

Straight ahead is LAND (LArge Neutron Detector), a 2 x 2 x 1 m^3 neutron detector composed of sandwiched iron and scintillator layers. This detector performs tof measurements of neutrons. At an angle of 15° with respect to the incoming beam axis, the heavy fragments resulting from the reaction pass through the GFI (Grosse FIber Detektor) detectors [79], scintillating fiber detectors used for position determination. The heavy fragments are finally characterized by a scintillator TOF Wall, the TFW (Time of Flight Wall). The characterization of the ^{10}Be fragment is achieved in this branch.

Similarly, the protons deflected by ALADIN are detected by two drift chambers and another scintillator TOF Wall [66].

2.2.1 Detection system before the target

The detection systems placed before the target are used to identify, in charge and mass, the different isotopes present in the cocktail beam. Following the beam, placed before the target are the S8, POS, ROLU and PSP detectors.

Located at the end of the FRS, there is the S8 detector, a plastic scintillator. It is composed by one paddle which is read by two photomultipliers placed opposite to each other. The S8 detector provides time signals used for time-of-flight (tof) measurements.

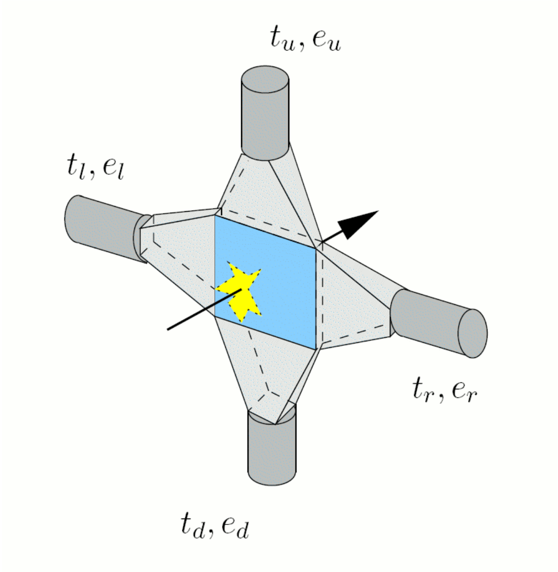

FIGURE 2.4: Schematic view of the POS detector. The time and amplitude signals provided by the four photomultipliers allows to determine tof, position and energy loss.

The POS detector is a 5×5 cm^2 plastic scintillator of 200 μm thickness. Its time and amplitude signals are readout by four photomultipliers placed at each side of the scintillator. The POS timing signal is used as the start for the tof measurements. A schematic view of the POS detector is presented in Figure 2.4.

Following the beam line inside Cave C, after the POS detector is the ROLU detector, a schematic view of ROLU is presented in Figure 2.5. This detector inherits its name from the four movable plastic scintillators that compose it: Rechts, Oben, Links, Unten. This detector is used to define the beam position and spot size and also acts as a veto in case an ion hits one of the its scintillators.

The PSP detector is a Position Sensitive silicon Pin diode of squared shape (4.5×4.5 cm^2). This detector has a thickness of 300 μm and in its front side are four anodes. These provide position information. The reverse of the detector acts as the cathode and provides information on the deposited energy of the passing ion. This signal allows the charge identification of the ion. A schematic drawing of the PSP detector is shown in

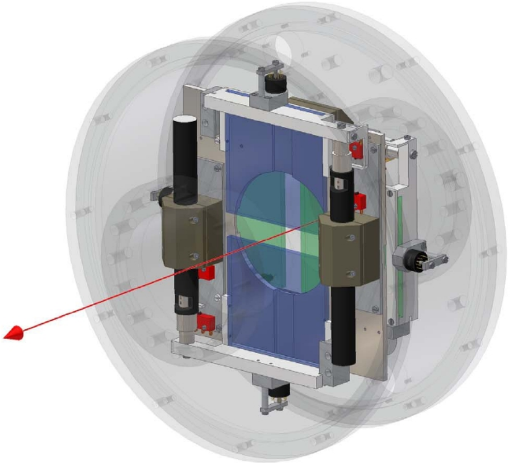

FIGURE 2.5: Schematic view of the RULO detector with its four plastic scintillators. By adjusting the position of the scintillators the beam spot size can be modified. The direction of the beam is also represented.

Figure 2.6. Regarding the position information of a passing ion, its determination is dependent of the calibration of the PSP with a scintillating mask, placed in front of the anode. This mask of 21×21 pixels did not work for the S393 experiment. Thus, the position information from the PSP could not be evaluated.

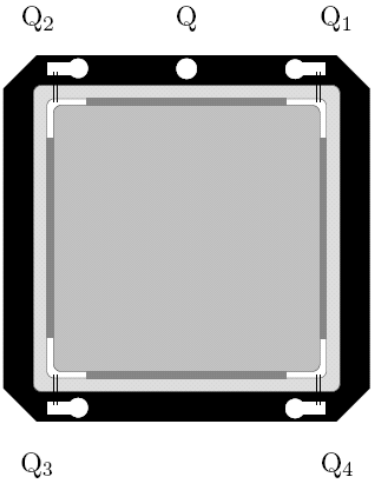

FIGURE 2.6: Schematic view of the PSP detector with its four anodes (Q_1, Q_2, Q_3, Q_4) and one cathode (Q). The energy deposited in the cathode allows to access the charge of the passing ion via Bethe-Bloch formula.

2.2.2 Detection system surrounding the target

Inside a vacuum reaction chamber, the target is surrounded by eight Silicon Strip Detectors (SSTs) responsible for charge and angular measurements. Enclosing the chamber are 159 NaI(Tl) crystals of about 20 cm length, dedicated to the detection of γ-rays, protons, neutrons and light charged particles. These two detection systems are further described in the following subsections.

Silicon Strip Detectors

The Silicon Strip Detectors (SSTs) in the LAND/R^{3}B setup surround the target. In particular, for the S393 experiment 8 detectors were used: 2 in front, 2 after the target and 4 arranged in a box. Figure 2.7 presents a schematic drawing of the layout of the SSTs in the setup.

The SSTs are used to track charged particles like protons and heavy ions. In addition, they also provide energy loss information which is used to perform charge identification.

These detectors are 72 mm x 40 mm in size and 0.3 mm thick. The SSTs are double sided silicon strip detectors in which the longer edge, the S-side, has 640 strips and a readout pitch of 110 μm and only one in four strips is a readout strip. The shorter side, the so-called K-side, has 384 strips with an implantation pitch of 105 μm, and each strip is a readout strip. Each detector has in total 1024 strips [77].

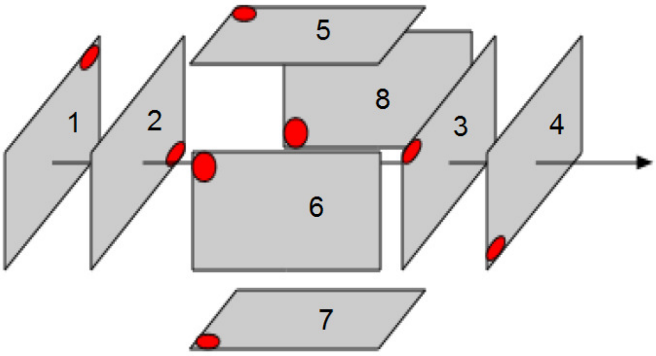

Figure 2.7: Silicon strip detectors schematic drawing. The arrow indicates the direction of the beam and the red dots the origin of the first strip.

The in-beam SSTs (1, 2, 3 and 4) are used to provide charge and angular information of the incoming beam and the heavy fragments that proceeded with the same direction as the incoming beam. The box detectors (5, 6, 7 and 8) allow to obtain precise angular information of charged particles that after will deposit their energy in Crystal Ball.

The relative z-axis position of the in-beam SSTs regarding the target is presented in Table 2.1. The values presented were obtained from a photometric measurement, these were corrected after performing an relative alignment of the in-beam SSTs.

SST	Position (cm)
1	-6.40
2	-3.70
3	11.06
4	13.62

TABLE 2.1: Relative z-axis positions of the in-beam SSTs considering the target at z=0.

Crystal Ball

In the experimental setup, a 4π calorimeter called Crystal Ball surrounds the target as represented in Figure 2.8. This detector is composed of 162 NaI(Tl) individual crystal scintillators coupled to photomultipliers. Each crystal has ∼20 cm length and is inside an aluminum case of 600 μm. The purpose of Crystal Ball is to detect the γ-rays, protons and neutrons that emerge from the reaction with the target [76].

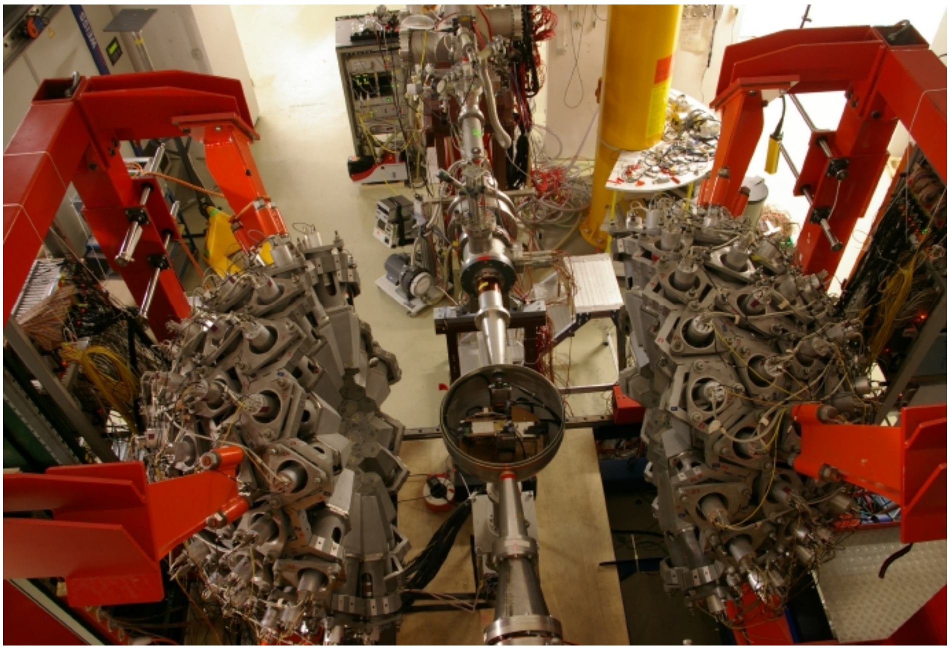

FIGURE 2.8: Photograph of the Crystal Ball detector opened. The reaction chamber is visible in the center.

Out of the 162 crystals that form Crystal Ball, only 159 were used, leaving the space for the structure support and the beam to pass through. Of the 162 crystals, 12 have pentagonal geometry and 150 of hexagonal of three different shapes. Despite the different geometries, each crystal covers the same solid angle of approximately 77 msr.

A particular feature of Crystal Ball is its high energy readout in the crystals of the forward hemisphere (2π). In fact this readout corresponds to the signal before the last stage of amplification in the photomultipliers. This feature allows for the detection of charged particles and neutrons expected to be emitted in the quasi-free scattering process.

2.2.3 Detection system after the target

After the target, the reaction heavy fragments continue focused in the forward direction due to beam high energy. These will be deflected according to their magnetic rigidity by the ALADIN dipole magnet. Its angular acceptance is ±60 mrad.

ALADIN (A Large Acceptance DIpole magNet) deflects the reaction fragments into three different branches: neutron, heavy fragment and proton.

Neutron arm

From the interaction with the target, nuclei can be excited and decay or breakup by emitting neutrons. In such a case, the neutron can be detected by LAND (Large Area Neutron Detector) [80]. This detector is at 0° in respect to the incoming beam direction and positioned approximately 13 m after the target. LAND allows for position (x, y, z), tof and energy measurements of neutrons ranging from 100 to 1000 MeV.

LAND is formed by 200 paddles distributed in ten planes. Each plane is perpendicular to the next allowing the x and y position reconstruction. Each paddle is 200 cm × 10 cm × 10 cm in length, width and depth and contains 10 layers of iron sandwiched with 10 layers of 5 mm thick scintillator material. The iron layers covering the detector are 2.5 mm thick , while the inner layers ate 5 mm. Overall, LAND is composed of 50% iron and 50% plastic scintillator. Figure 2.9 is a picture of a real LAND paddle revealing its sandwich structure.

The layer structure follows the detection principle, the impinging neutron will interact with the iron producing charged particles, mainly protons, that produce light in the scintillator layer which is then readout by two photomultipliers, one at each extremity of the paddle.

Heavy fragment arm

The forward focused heavy fragments resulting from the reaction will be deflected by ALADIN with a deflection angle of approximately 15°. In their path the heavy ions will pass through three detectors: the GFI detectors and the TFW. These perform position, energy and tof measurements.

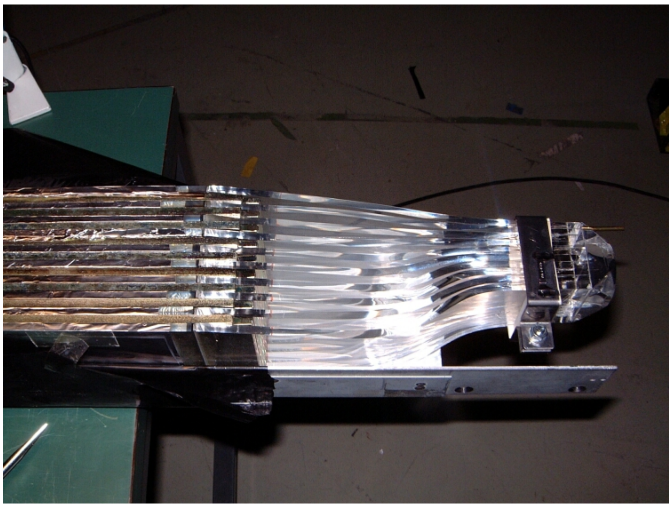

Figure 2.9: LAND paddle layer structure. The iron layers are sandwiched between scintillator layers.

There are two GFI (Große FIber Detektor) [79] detectors along the heavy fragment branch. Each GFI is composed of ∼500 scintillating fibers that cover an active area of 50×50 cm^2. A schematic view of the GFI detector is shown in Figure 2.10.

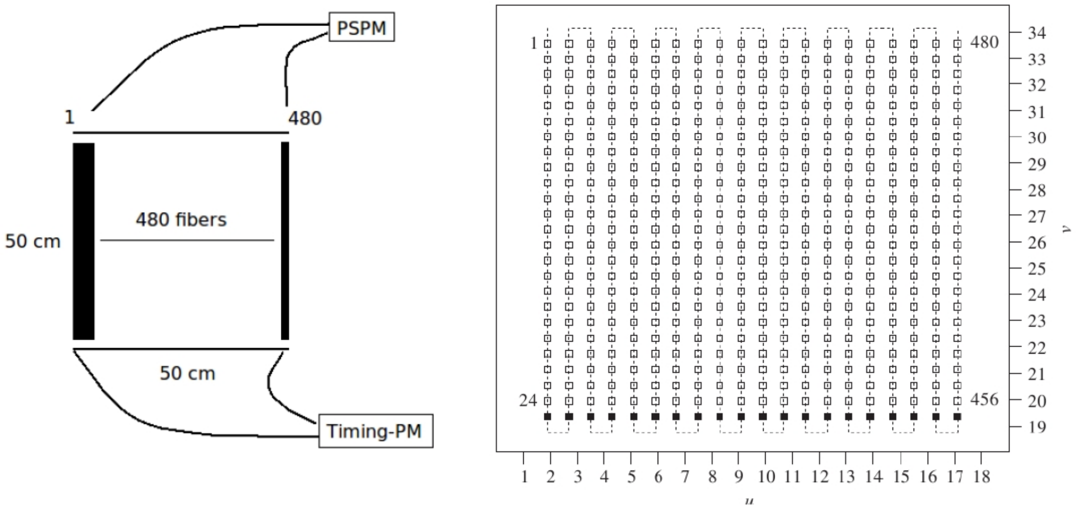

Figure 2.10: Schematic view of the GFI detector and the its mask. The later is used to connect the fibers to the PSPM.

The fiber present a square cross-section of 1×1 mm^2 and are coated by a lower refraction index material for light guiding purposes. An additional white coating is used to avoid cross talk. The extra coating materials reduces the geometric efficiency of the detector to slightly bellow 90% for perpendicular impinging particles.

By means of a mask, each fiber is connected sequentially to the position-sensitive photomultiplier (PSPM) on one end and to a regular photomultiplier on the other. The information collected from the later can be used for timing purposes (not used in the S393 experiment).

At the PSPM each fiber is associated with a specific (u,v) coordinate. The PSPM is formed by a photocathode, 16 mesh-type dinodes and a anode with 18 wire in the x-direction (u) and 16 wires in the y-direction (v). The distance between the anode wires is about 3.7 mm.

The light produced in the fibers from a passing ion is guided to the mask. The position of the light in the photocathode is used to determine the fiber and thus the x-position of the ion trajectory in the detector. More information on the position reconstruction from the detector (u,v) coordinates to the x-position in the laboratory frame can be found at [81].

Following the heavy fragment arm, the Time of Flight Wall (TFW) is used to collect energy loss and tof information of the passing ions. While the energy loss can be used to reconstruct the charge, the tof information allows to determine the nominal velocity β of the ions.

TFW is comprised by 32 plastic scintillator paddles, each readout with photomultipliers at both extremities. The paddles form two planes perpendicular to the beam direction. The first plane holds 14 vertical paddles of 147 cm and followed by 18 horizontal paddles of 189 cm. Each paddle has a width of 10 cm and a depth of 0.5 cm. Figure 2.11 presents a picture of the TFW detector.

Protron arm

The proton arm detectors cover an angular region centered at 30° with respect to the incoming beam direction. This arm is dedicated to measure the momenta of the protons that resulted from the decay or breakup of excited nuclei. Two detectors can be found in this line, the Proton Drift Chambers (PDCs) and a Time of Flight Wall, the so-called DTF. These are used for tracking and to determine the velocity of the protons, respectively.

There are two drift chambers placed before the DTF detector. The PDCs are gas detectors filled with a 20% of CO_2 and 80% Ar mixture. Each PDC has two layers which provide x (144 channels) and y (112 channels) position. The layers contain eight planes, six of conducting wires and two of sense wires. When “slicing” the detector, it is possible to verify that the conducting wires are arranged in a hexagonal structure and the sense wires is in its centre, as shown in Figure 2.12.

FIGURE 2.11: The heavy fragment branch Time of Flight Wall. Two perpendicular planes of plastic scintillator paddles are used to determine the charge and β velocity of the impinging heavy ions.

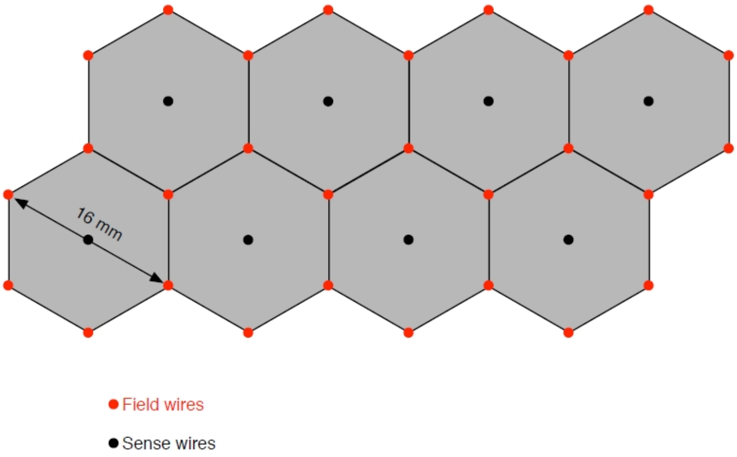

FIGURE 2.12: Scheme of the PDC hexagonal drift cells. At the center of the hexagons are the sense wires (black) and at the edges the field wires (red).

When a proton passes through, it ionizes the gas atoms that are after directed towards the sense wires due to the field created by the field wires.

The DTF is a Time of Flight Wall comprised by nine scintillator paddles. Its main goal is to measure the energy and the time of flight of protons. The paddles are distributes in two planes. The vertical plane has 6 paddles of 120 cm length, 20 cm width and 1.5 cm thickness. While the horizontal paddles are 140 cm in length, 20 cm wide and 0.5 cm thick and are separated by ∼44 cm. Similar to TFW, all paddles are readout by photomultipliers at both ends, as shown in Figure 2.13.

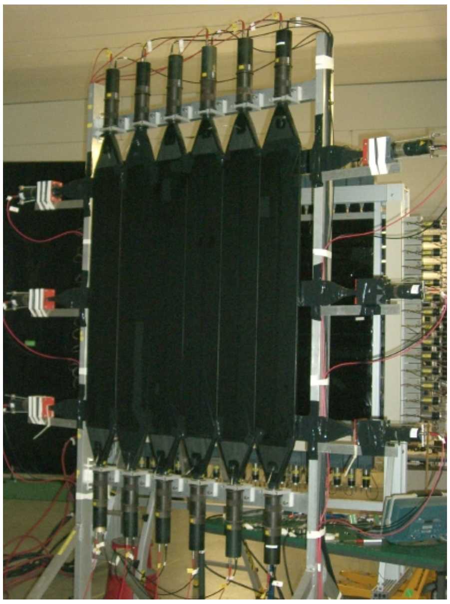

FIGURE 2.13: Time of flight wall composed of plastic scintillators placed in the proton fragment branch, the so-called DTF.

2.3 Triggers

Not all events are recorded. The Data AcQuisition (DAQ) system will only process an event when certain trigger patterns, combinations of logic signals from the detectors are achieved. This avoids unnecessary dead time. In addition, the priority of the trigger patterns reveals the significance of the underlying physics of the event.

The trigger patterns are not only useful during the experiment but also in the analysis stage. Table 2.2 contains the list of trigger patterns used during the S393 experiment along with a short description. The triggers are divided in two groups: “onspill” or physics triggers and “offspill” or calibration triggers.

Regarding the priority of the triggers, a Down Scale Factor (DSF) is atributed to each trigger. This factor is larger if the trigger/reaction is expected more often, allowing the DAQ to select events more meaningful. The DSF range from 1 to 1024. In case of the later only one out of 1024 events associated to the trigger pattern in question will be recorded.

Trigger bit (n)	Trigger pattern	Name	Description
1	1	Minimum Bias	Good beam
2	2	Fragment	Fragment detected in TFW
3	4	FRS S8	Signal in S8 (FRS)
4	8	Crystal Ball Sum	Crystal Ball high energy and fragment in TFW
5	16	Proton	Proton detected in DTF
6	32	Good Beam - pileup	Removes pile-up
7	64	Pix	Hit in pixel detector (PSP calibration)
8	128	Neutron	Hit in LAND and Fragment in TFW
9	256	Crystal Ball Muon	Crystal Ball calibration
10	512	LAND Cosmic	LAND calibration
11	1024	TFW Cosmic	TFW calibration
12	2048	Crystal Ball Gamma	Crystal Ball calibration
13	4096	DTF Cosmic	DTF calibration
14	8192	NTF Cosmic	NTF calibration
15	16384	Crystal Ball Left+Right muon	Muon detected in both halfs of Crystal Ball
16	32768	-	Not used

TABLE 2.2: Trigger information used in the S393 experiment.

Chapter 3

Calibration

The present chapter contains a description of the procedures employed to calibrate several detectors used in the S393 experiment. In particular, it describes an overview of some of the process required to obtain meaningful observables from raw data using the collaboration analysis framework *land02* [82]. Following this, are the calibration procedures in which the author of this work was focused: calibration of the beam diagnostic detectors and the Silicon Strip Detectors.

Last but not least, a brief description of the method used to track the particles through the magnetic field of ALADIN, that allowed the determination of its mass and thus used to characterize the nuclei after the reaction, is provided together with its calibration procedure.

3.1 Overview of the land02 Calibration Tool

The information collected at the several detectors of the setup by the DAQ system is clustered in events by the Event Builder. The information is then stored in *lmd*-format files (list mode files). Developed by H. Johanson [82], there is a software package available in the collaboration that makes easier the calibration procedure. This procedure aims to retrieve the physical quantities (time (ns), energy (MeV) and position (cm)) from the histogram channel values.

Using the *land02* software package it is possible to convert (unpack) the *lmd* files into ROOT [83] files and also to perform some calibrations. There are several calibration steps associated to different unpacking levels:

- RAW - This level converts the binary format into ROOT files where the information is organized by detector and given in TDC, QDC and ADC channels.
- TCAL - From the RAW level, using the *tcal* and *clock* routines it is possible to extract the parameters necessary to convert the TDC channels into time units (ns) and to subtract the pedestal of the QDC.
- SYNC - After determining the necessary parameters (usually retrieved with the *phase1* routine) and including them in *land02*, this level allows to reconstruct the data for the whole detector as a unit, i.e. synchronize the individual detectors that compose the overall detection system.
- DHIT - This level characterizes the hit in the detector specific coordinates providing position, energy loss and time information.
- HIT - The position, energy loss and time information is here provided in cm, MeV and ns.
- TRACK - In this level the reconstruction of the mass, atomic number and velocity of the ions is achieved, allowing to identify the different isotopes present.

The following two sections introduce and provide the performance details of the time calibration and pedestal removal performed in the TCAL leval if *land02*.

3.2 Time Calibration

The time calibration is essential to convert channels in time units, in this case nanoseconds (ns). This procedure is required for every detector that collects time information. In fact, the time information from the several detectors is relative to the time of a certain reference detector, in this case the master start was a signal collected at the POS detector. Therefore, time is mentioned as a time difference and is mostly referenced as a time of flight of particles (tof).

During the S393 experiment, to obtain time information in ns two logic signals were sent to the Time to Digital Converters (TDCs) from the trigger logic module. One signal was responsible for the start of the time counting, the other for the stop. The time interval (ns) between the two signals was known (Tcalt). This reference value, allowed to make a correspondence between the channels of time information and the nanosecond time scale, i.e to calibrate the time intervals measured by the TDCs.

For example, the linear relation between the output of POS and S8 detectors in channels and the time interval (ns) allowed to extract the parameters presented in Table 3.1.

The validation of the parameters for all the files recorded during the experiment was also performed. For the POS detector the parameters offset and slope were stable throughout the experiment, while the S8 parameters changed at one point due to a TDC replacement.

		Output	Offset (ns)	Slope (ns/ch)
SCI	Before TDC change r326-r376	S2 11	273.455	0.025022
		S2 12	277.978	0.029061
		S8 21	328.188	0.025033
		S8 22	330.152	0.024863
	After TDC change r377-r518	S2 11	219.827	0.0484576
		S2 12	224.218	0.0478246
		S8 21	273.251	0.0478528
		S8 22	275.846	0.0465496
POS	r326-r497	POS 1	332.941	0.0252579
		POS 2	323.799	0.0251726
		POS 3	316.379	0.0249855
		POS 4	307.726	0.0249629

Table 3.1: Scintillators (SCI) and POS offset and slope parameters determined for the time calibration. In the case of S8, the parameters before and after the TDC replacement are presented.

3.3 Pedestal Subtraction

The pedestal arises from the internal capacitance present in the QDCs (Charge to Digital Converters). It has to be subtracted from the data in order to obtain the correct energy information that corresponds to physical data. The effect of the pedestal can be seen in Figure 3.1, showing the raw energy spectrum of one strip. The pedestal is the first bump in the spectrum in Figure 3.1, around channel 430.

In more detail, QDCs convert charge into digital values, by measuring the voltage on an internal capacitor. If the gate is open, the capacitor is charged by the signal of the detector and by a very little current (I_{ped}) provided by the QDC itself. Therefore, the capacitor always contains at least the charge due to that current: $I_{ped}\times$length-of-gate. This results in a non-zero conversion value, the so-called pedestal.

During the experiment a clock signal was sent to the QDCs in order to continually obtain the pedestal value. Whenever a QDC is used, the pedestal must be subtracted. In the case of the SSTs, the subtraction of the pedestal is done by fitting a Gaussian and obtaining its mean and sigma values, in order to subtract it from the energy spectrum.

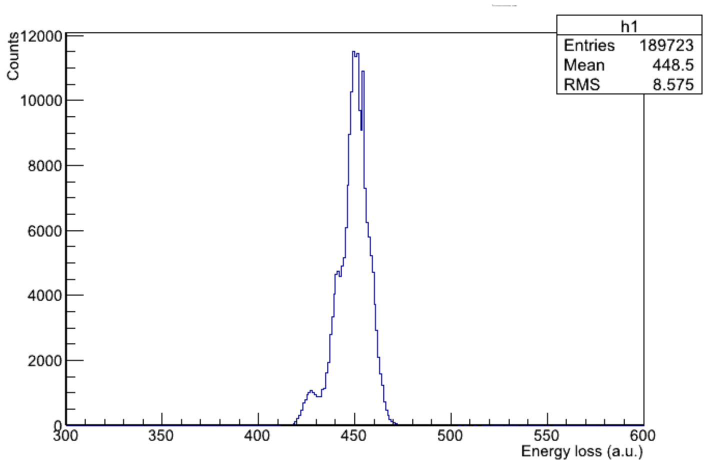

FIGURE 3.1: Example of an energy spectrum from the silicon tracker before pedestal subtraction. The pedestal is seen around channel 430.

The parameters were obtained for all the strips of the 8 detectors and a stability study was performed. The idea was to determine the clock parameters from the average of all the values, for all the runs. The initial values were determined with the *clock* program of *land02*.

The final parameters obtained were in fact the average of the parameters for every run. As an example, Figure 3.2 shows the final pedestal mean values for each strip of SST 3.

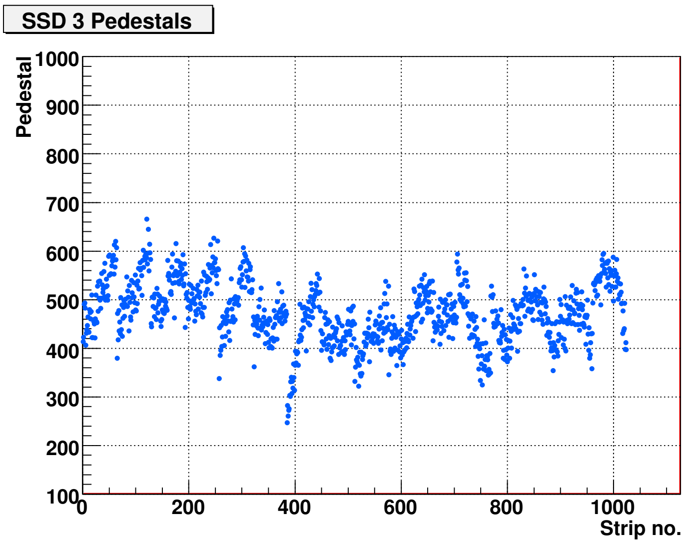

FIGURE 3.2: Pedestal mean values for each strip of SST 3.

After these two general calibration steps, common to most of the detectors used in the experimental setup considered in this work, we will present some specific aspects of the detector systems calibrated by the author of this work, starting with the calibration of those units used to characterize the cocktail beam of isotopes arriving to the target area.

3.4 Beam Diagnostics Detectors Calibration

The incoming beam detectors are placed before the target and their main goal is to identify the different nuclei that reach the experimental setup. These include time of flight detectors, the S8 and POS scintillators, and an energy loss detector, a Position Sensitive silicon Pin diode (PSP). While the S8 scintillator is located at the FRS the POS and PSP are located at the experimental area as shown in Figure 3.3.

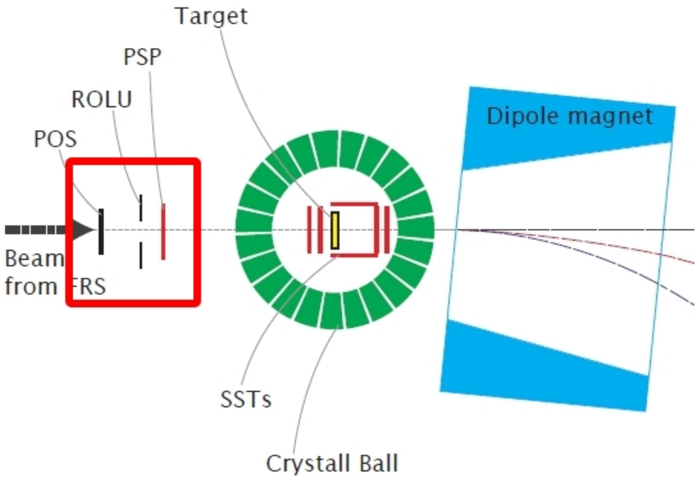

FIGURE 3.3: Location of the beam diagnostic detectors PSP and POS.

These detectors are crucial in the identification of the different isotopes arriving at the target area, being the ion identification only possible after the charge and the mass-to-charge ratio calibration.

3.4.1 Charge Calibration

Taking advantage of the energy loss obtained, we aim at extracting the correct atomic number (Z) of the incoming nuclei from the energy loss detected.

The charge or Z calibration is achieved using the Bethe-Block formula,

$$\frac{dE}{dx} = -\frac{4\pi}{m_e c^2}\left(\frac{N_a Z \rho}{A M_u}\right)\frac{Z^2}{\beta^2}\left(\frac{e^2}{4\pi\epsilon_0}\right)^2\left[ln\left(\frac{2m_e c^2\beta^2}{I(1-\beta^2)}\right) - \beta^2\right], \tag{3.1}$$

where

m_e - electron rest mass
c - speed of light
v - velocity of the particle
N_a - Avogadro's number
Z, A - atomic number and mass number of the material
ρ - surface material density
M_u - Molar mass constant.
e - electron charge
ε_0 - vacuum permitivity
I - mean excitation potential of the material
$\beta = \frac{v}{c}$

This formula relates the energy loss with the atomic number, Z. The energy loss (dE) can be measured before the target in the PSP cathode. Therefore, in this calibration we aim for a correspondence between channel and energy loss, using it to extract Z.

In the case of the PSP detector its characteristics (dx, Z, A, ρ and I) are known: dx=320 um, Z=14, A=28.088, ρ=2.33 cm^{-2}, I=0.173 (keV). The total charge (Q) is collected from the back side cathode and this signal is directly related to the total energy loss of the incident particle, which is in turn related to the atomic number (Z).

Following Equation (3.1), in order to determine the energy loss (MeV/u) in the PSP detector it is necessary to determine the nominal velocity (β). This parameter can be calculated from the beam energy (in units of MeV/u), which is known from the FRS beam deflection settings. Finally, one can obtain the energy loss in the PSP for each Z.

The energy loss spectrum obtained from the PSP cathode is shown in Figure 3.4. The events considered are such that the number of neutrons is equal to the number of protons (N=Z), i.e. the FRS settings were such that the ions that reached the setup where characterized by N=Z (^{6}Li, ^{8}Be, ^{10}B, ^{12}C, etc).

In the PSP spectrum there are several peaks, corresponding to the energy loss of the ions that passed through the detector material as shown in Figure 3.4. Each ion is identified by its atomic number, Z.

It is known that in nature the ^{8}Be nucleus is not bound, therefore we expect a gap instead of a peak at the corresponding position. This fact allows us to make the correct correspondence between peaks and isotopes, necessary to make the correlation between channels and energy loss.

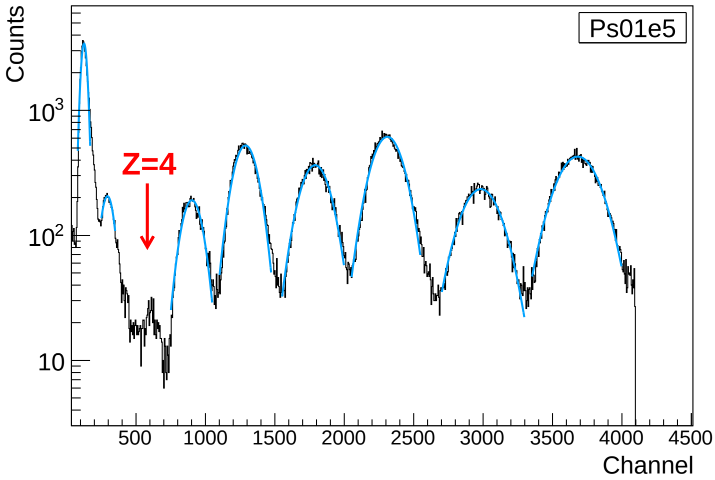

FIGURE 3.4: PSP cathode energy loss spectrum of events characterized by the N=Z relation. The gap around channel 600 is expected and corresponds to the ^{8}Be nucleus. It provides a good starting point to identify the nuclei that are present. Each peak is fitted with a gaussian, used to determine the centroid channel corresponding to each isotope.

Applying a gaussian fit to the peaks, as shown in Figure 3.4, we can get the centroid value for each Z value. In Figure 3.5 is represented the correlation between the calculated energy loss (MeV) in the PSP detector and the centroid value (channels). A linear fit was applied and the calibration parameters extracted.

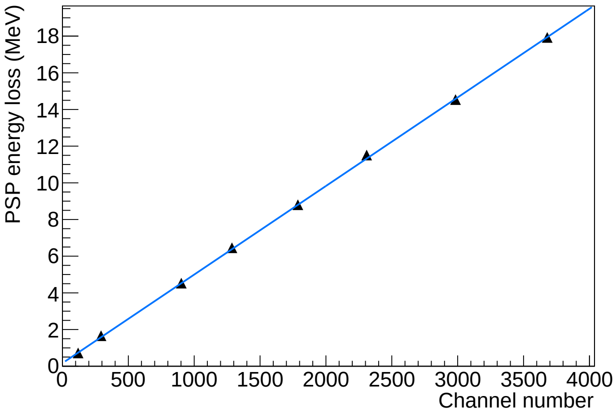

FIGURE 3.5: Energy calibration of the PSP: correlation between energy loss (MeV) in the PSP and the centroid channel obtained from the gaussian fit shown in Figure 3.4. A linear fit was used to extract the calibration parameters.

3.4.2 Velocity calibration

In order to perform the velocity calibration, also called mass-to-charge ratio (A/Z) calibration, the previous charge calibration must be completed. The velocity calibration aims at obtaining the correct correspondence between the times measured and the mass-to-charge ratio (A/Z) of the observed nuclei. This is achieved by determining the distance between ToF detectors and the time offset. In fact, the times measured are related to the ToF of the particles by an offset caused by electronics and cable delays.

A particle with mass m, charge q and velocity $\overrightarrow{v}$ moving in a magnetic field, $\overrightarrow{B}$, experiences a magnetic force described by $\overrightarrow{F} = q\overrightarrow{v} \times \overrightarrow{B}$. In the case of a magnetic field perpendicular to the velocity of the particle, this expression is reduced to $F = qvB$ and the particle is subject to a centripetal acceleration, $a = \frac{v^2}{\rho}$ where ρ is the curvature radius.

Considering the previous statements, one finds $\gamma ma \approx qvB \Longrightarrow \gamma m\frac{v^2}{\rho} \approx qvB$. Also considering $v = \beta c$, $q = Z.e$ and $m = A.u$, we have

$$\frac{A}{Z} \approx \frac{B\rho}{\beta\gamma}\frac{e}{cu}. \tag{3.2}$$

Equation (3.2) contains the relation between $\frac{A}{Z}$ and β. Considering the traveled distance d, β relates to the ToF of particles, according to

$$\beta = \frac{d}{c\,ToF}. \tag{3.3}$$

However, the time measured by the DAQ also includes a time offset, t_{off}, due to electronics and cable delays. Thus, the times measured, δt, relate to the ToF as

$$\delta t = ToF + t_{off}. \tag{3.4}$$

Replacing ToF in Equation (3.4) in (3.3), we obtain

$$\beta \cdot \delta t = \frac{distance}{c} + \beta t_{off}. \tag{3.5}$$

It is in this last expression that we find the parameters (distance and t_{off}) required to obtain the correct mass-to-charge ratio. For this purpose, the two plastic scintillators part of the beam diagnostic detectors are used to measure the ToF, the POS and the S8. Their description can be found in Section 2.2.1.

In order to perform the velocity calibration, we must use several runs for which we know the ratio A/Z (given by the FRS settings). Regarding the S393 experiment, we used a run characterized by an A/Z=2 and another by A/Z=3. Considering that the charge calibration was already performed, it is possible to identify the isotopes present in the beam.

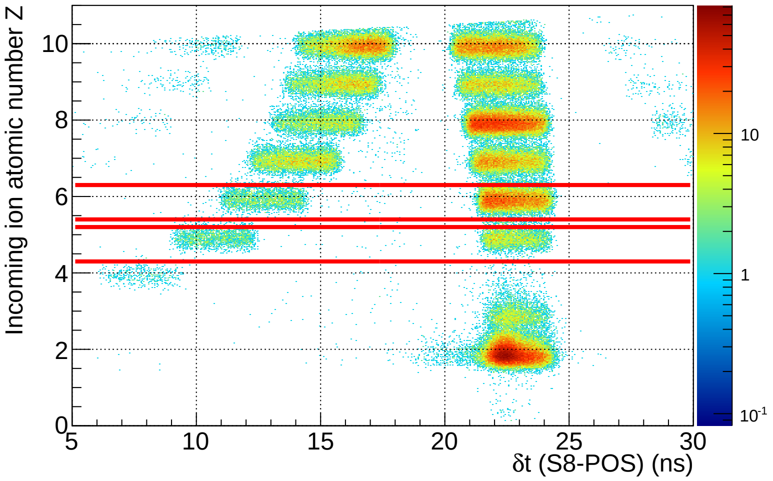

FIGURE 3.6: Particle identification plot, for A/Z=2 setting focusing on Z=6 and Z=5.

In Figure 3.6 is shown a study of the atomic number of the nuclei (Z) and the measured tof between the S8 and the POS detector, in which a higher mass corresponds to a lower tof. We can select a charge range of incoming ions being sure of their atomic number. In Figure 3.6, for the case of A/Z=2 events, if we consider Z=5 from left to right, we find A=11 and A=10 and with Z=6 we have A=13 and A=12.

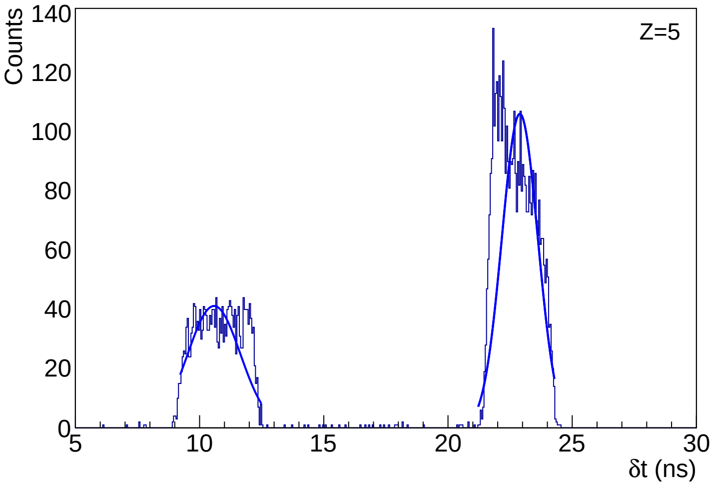

FIGURE 3.7: Incoming ion projection for Z=5 for a A/Z=2 setting.

As shown in Figure 3.7 for Z=5, a gaussian fit can be used to obtain the mean measured time interval (δt) for the different isotopes in the different runs. The energy loss and the β values were also determined for the same nuclei.

In order to obtain the calibration parameters required by Equation (3.5), we study the correlation between the mean value of $\beta \cdot \delta$t and β, as shown in Figure 3.8.

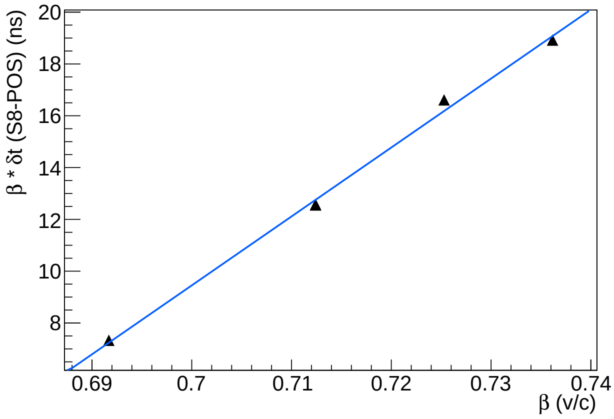

FIGURE 3.8: Study of the correlation between $\beta \cdot \delta$t mean value and β. The parameters obtained correspond to a time offset (slope, p_1 in ns) and the other to a distance between detectors (offset, p_0 in) introduced in Equation 3.5.

3.5 Calibration of the Silicon Strip Detectors

The Silicon Strip Detectors (SSTs) in the LAND/R^{3}B setup surround the target. In particular for S393, 2 detectors were in front of the target, 2 behind the target and 4 around it (box detectors). This detector system provides position, angle and energy loss information. The next paragraphs provide information on some aspects that allow to correctly obtain these measurements.

When impinging on a SST, a charged particle (proton or fragment) generates a signal in several (N) strips, the group of strips with a signal is called **cluster**.

The total charge deposited in the detector, Q, is the cluster sum, or also called the cluster area (the area bellow the energy deposited curve in the strips),

$$Q = \sum_{i}^{N} q_i \, . \tag{3.6}$$

The hit position, $X_{S,K}$, can be retrieved taking into account the charged-weighted center of gravity, CoG,

$$CoG = \frac{\sum_{i}^{N} n_i \times q_i}{\sum_{i}^{N} q_i}, \tag{3.7}$$

$$X_{S,K} = CoG \times d_{S,K}. \tag{3.8}$$

Where n_i is the strip number and $d_{S,K}$ is the strip implantation pitch distance, (S-side=110 μm; K-side=104 μm).

The SSTs are used to measure energy loss and position. To obtain those measures a pedestal subtraction must be performed before any further corrections are applied. Also the strips that did not work during the experiment had to be identified.

3.5.1 Dead Strips Identification

The detectors have in total 1024 strips each. Some of the strips may be marked as "dead" if there is no output signal. A threshold was set. If there was no energy deposit above 50 (counts), the strip is marked as dead. This is important to correctly account for the center of gravity and in its turn the hit position, $X_{S,K}$.

Figure 3.9 shows the energy loss in SST 2 on the K-side.

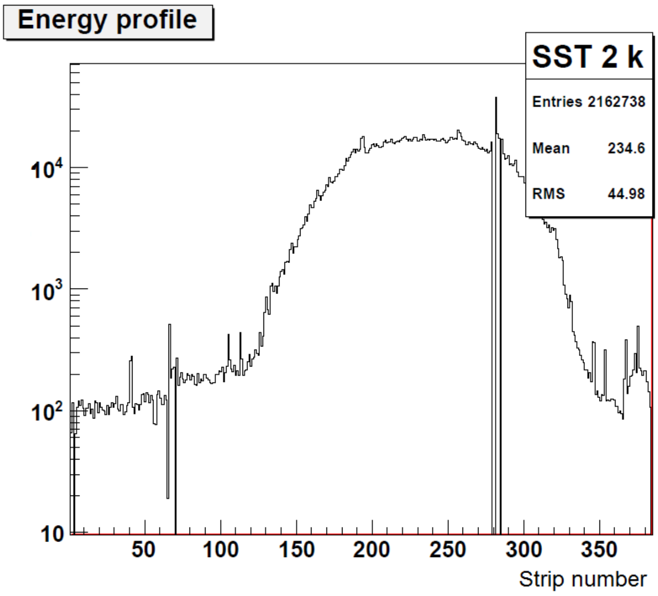

FIGURE 3.9: Projection of the energy loss in the strips of SST 2 K-side. The dead strip identification was performed by imposing a threshold in energy loss.

3.5.2 Position Correction

Due to the presence of floating strips i.e, strips that are not read out, the relation between the particle position and the charge collected in the readout strip is affected. In this correction we aim to determine the real position of the hit relative to the first cluster strip on the left. The following calibration was only performed on the inbeam detectors because for these detectors we are able to select a particular nucleus and study its energy loss, using data when no target was present (empty run).

If we consider E_{S_1} and E_{S_2} as the two highest energy signals, we can define $\eta = \frac{E_{S_2}}{E_{S_1}+E_{S_2}}$, where the indexes represent the readout order. In fact it is expected to see a flat correlation between the relative charge collected on the two strips and the track position in the readout gap, $X_{CoG} = X_1 + pitch \times \eta$. However if one represents the normalized η distribution, $f(\eta)$[1], one can see enhancements at the floating strips positions, as shown in Figure 3.10. Finally the correct position can be obtained from $X_\eta = X_1 + pitch \times \int_0^\eta f(\eta')\,\mathrm{d}\eta'$. Detailed information on the position reconstruction can be found in [84].

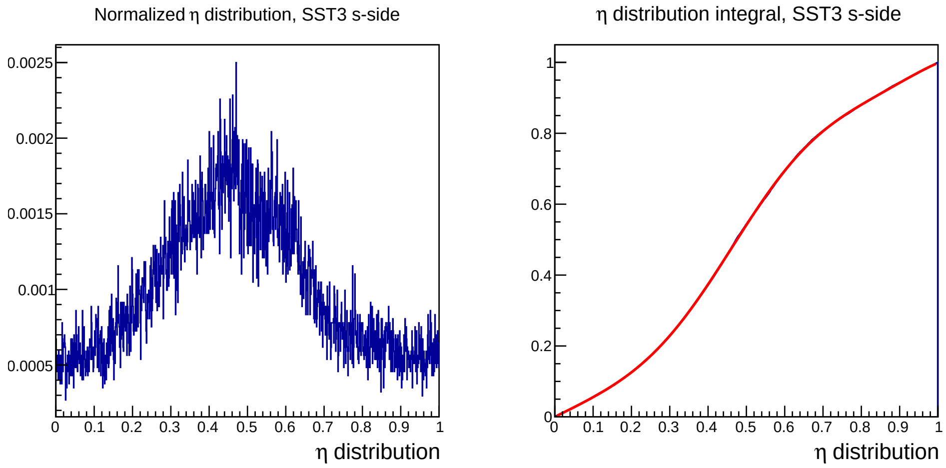

FIGURE 3.10: Position calibration for SST 3, S-side. At the right is the normalized η distribution, $f(\eta')$ and in the left the integral of this distribution. The presence of peaks reveals the position of floating strips.

In order to extract the correct position of the hits, the integral of the normalized η distribution was determined for each of the 4 detectors and fitted, as shown in Figure 3.11. This concluded the position calibration and the results can be seen in Figure 3.12. The obtained parameters attribute to a certain η a distance between two consecutive strips.

---

[1] Obtained by summing the individual inter-strip distributions.

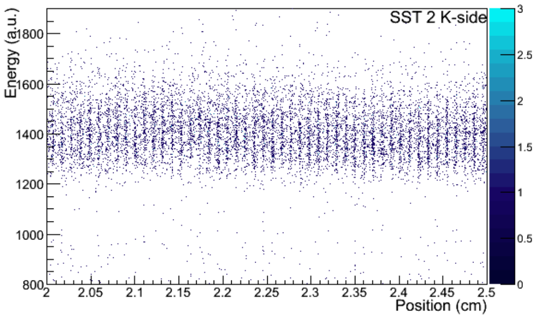

FIGURE 3.11: Correlation between energy loss (a.u.) and position (cm) on SST 2, K-side, before the position correction.

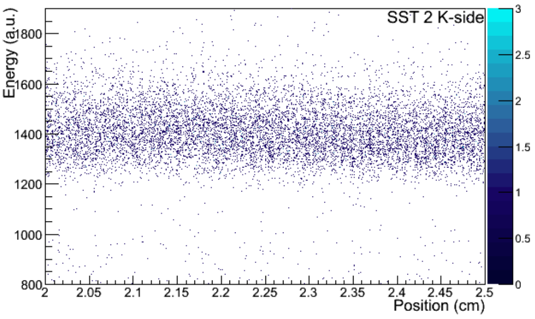

FIGURE 3.12: Result of the position calibration for SST 3, K-side, study of the correlation between the energy loss (a.u.) and position (cm) after the position correction.

3.5.3 Energy Gainmatch

The energy gainmatch correction is performed to improve the energy resolution, and thus, the identification of the different isotopes. The energy deposited (ΔE) for the same isotope with the same energy should be the same for every strip. However this is not the case, as shown in Figure 3.13 for SST 3, K-side and must be corrected.

The general idea of the gainmatch is to select a nucleus and choose a reference ΔE for that nucleus. Then the measured ΔE measured for each strip can be corrected with a multiplication factor to match the reference value. The procedure is repeated for each strip. Because of low statistics, a gaussian fit of the peak didn't offer any advantage over simply selecting the mean value of the measured energy. The application of this correction allowed to improve the energy resolution, as shown in Figure 3.14 for one nucleus.

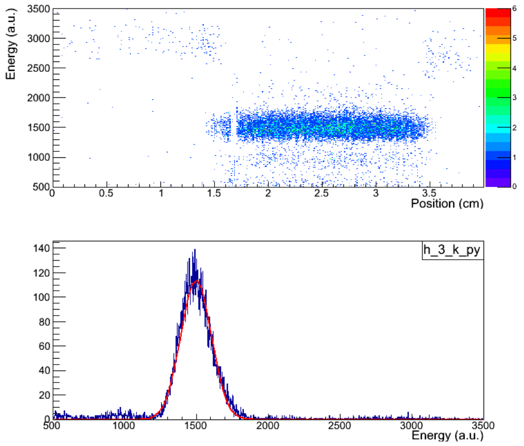

FIGURE 3.13: Correlation between the energy loss and the position in SST 3 K-side, without gainmatch.

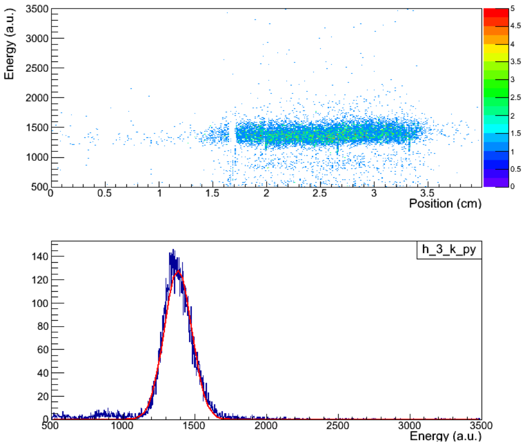

FIGURE 3.14: Result of the application of the gainmatch for SST 3, K-side.

3.5.4 Energy Correction

As mentioned previously the energy deposited is affected by the floating strips. Studying the energy deposited as function of the η distribution, it is possible to observe an increase in energy loss in the position of the floating strips, as shown on the left of Figure 3.15. This should be a flat distribution because the energy deposit of the nucleus selected should be the same.

In order to perform this correction, the correlation between energy loss and the η distribution was studied and a fit was made to the profile of this distribution. The evaluation of the fit allows to correct for the artificial energy deposit. The results of this calibration can be seen in Figure 3.15.

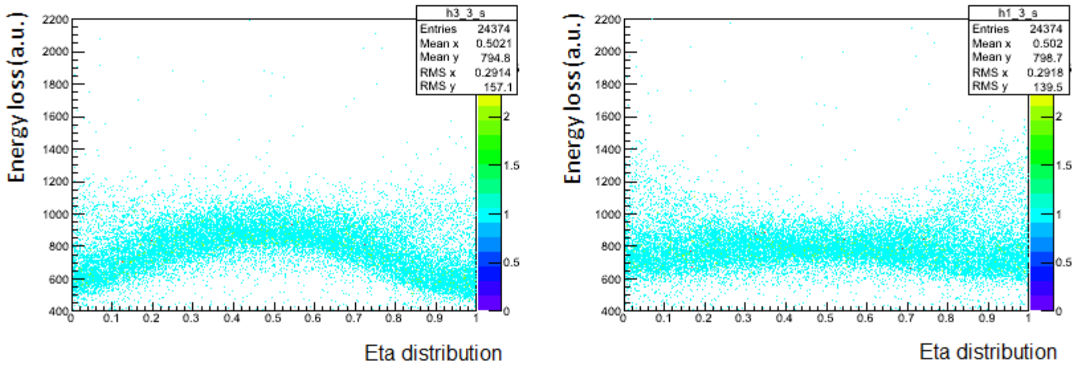

FIGURE 3.15: Correlation between energy loss and the η distribution, before the energy correction (left) and after performing the energy correction (right).

3.5.5 Detector alignment

For each event, the fragment angle must be corrected by the incoming projectile angle in order to obtain the angular response due to the reaction. These angles are obtained through the hit positions in the Silicon Strip Tracker (SSTs) placed before and after the target, the so-called in-beam SST detectors.

The correct incoming and outgoing angles are deduced by aligning the SSTs. The basis of the alignment is to consider that the trajectories of the nuclei consist of straight paths when no target is present, and the position origin is in the center of the target. Following this, the path of a projectile can be described by two linear equations: $x, y = m_{x,y}z + b_{x,y}$ where the z is the position of the detectors along the beam line.

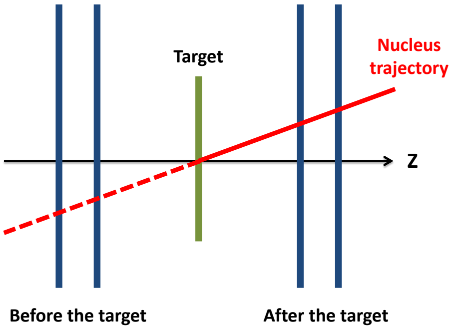

FIGURE 3.16: The hit positions on the SSTs were used to determine the path of the ions (solid line), and to calculate the expected path on the other detectors (dashed line).

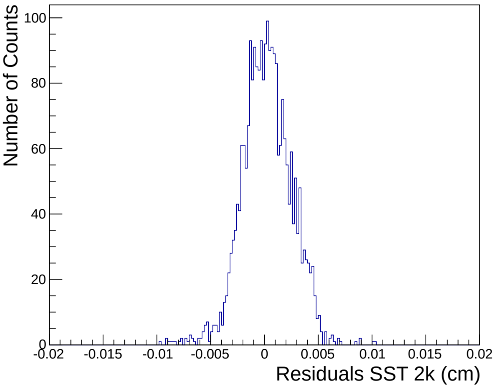

FIGURE 3.17: Residuals for SST 2 K-side (y direction) after the alignment of the SSTs. The residuals are defined as the difference between the determined and the expected hit position assuming a straight path.

In addition, the calibration of the tracking routine provides the correct positions of the SSTs after the target. The hit positions on these SSTs can be used to calculate the trajectory and to determine the expected hit positions in the SSTs before the target, as shown in Figure 3.16. The residuals (difference between the measured and calculated hit position) can be used afterwards to carry out a fine adjustment of the x and y position of the SSTs before the target.

Thus the alignment consisted on two corrections. Firstly, the trajectory was calculated just using the hit positions of the two detectors after the target and correcting the two others before. At a second stage, three hit positions were considered leaving one detector to be adjusted at a time. The alignment was concluded when the residuals were centered at zero. To overcome the low statistics of ^{11}Be in the runs with no target, ^{12}Be projectiles were considered for this procedure.

It should be highlighted that the expression *unreacted beam* indicates that ^{11}Be is the impinging nucleus and is also the outgoing fragment (^{11}Be→^{11}Be), while *reacted* refers to the ^{11}Be(p,X)^{10}Be reaction. The detector alignment method was applied to the projectile of interest ^{11}Be impinging on a CH$_2$ target and the angular distributions can be seen for the *unreacted* and *reacted* beam in Figure 3.18.

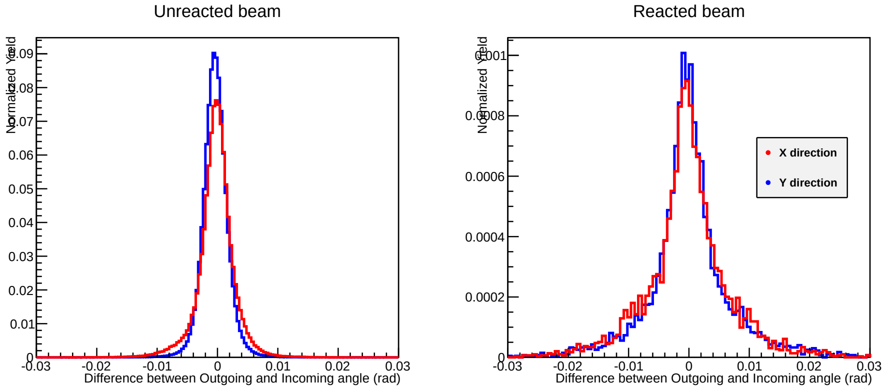

FIGURE 3.18: Unreacted and reacted beam fragment angles after correcting with the incoming projectile angle.

3.6 Tracking routine

The so-called *tracker* is a tool developed within the R^{3}B collaboration, it is a software tool allows to track and identify the fragments after the reaction target.

After the target, the heavy fragments resulting from the collision of the projectile beam with the target go through the SSTs and are deflected by the ALADIN dipole to the heavy fragment branch. The detectors on their trajectory (SSTs and TFW) allow to measure their energy loss, position and tof. Following Equation (3.2), the fragment mass is determined when the magnetic field is known. In the case of Berylium isotopes the GFIs (fiber detectors present in the heavy fragment branch) are not included in the *tracker* due to their low efficiency for low charges.

The *tracker* reads in an event-by-event basis, the hit position on the SSTs, using the field maps of ALADIN it checks if the position measured after the dipole is in agreement with the calculated/expected position. When this occurs, the event is kept and the fragment mass is calculated. In addition, the *tracker* can run in forward or backward mode (with respect to the incoming beam). In the forward mode the positions on the SSTs are fixed and the check is done on the detectors further away from the target. While in backward mode, the particle travels in the opposite direction of the beam, and the fixed positions are further away from the target.

In the GUI feature of the *tracker* it is possible to check the path of the fragments, event by event. In Figure 3.19 is shown the path of fragment resulting from an incoming ^{11}Be nucleus. The green color identifies the events that were kept.

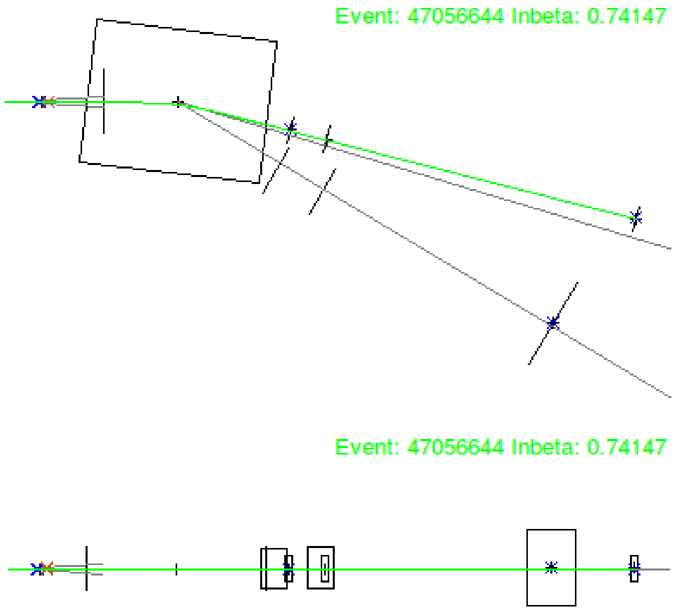

FIGURE 3.19: Example of the tracker GUI. In this case an ^{11}Be nucleus is detected at the entrance of the setup and its path is such that the event is kept (in green).

The difference between the measured and calculated positions is called *residual*. These are used to fine tune the detector positions.

3.6.1 Tracker calibration

The correct use of the *tracker* must be preceded by following several steps:

- Define a setup file that contains the detector positions and target definitions.
- Insert some of the reaction gates in the experiment specific file. In particular, select the incoming beam, trigger pattern and the outgoing charge-defining energy gate.
- Correct the tof offset: Run the *tracker* using a CH_2 target run and correct the tof offset with the residual obtained.
- Iteratively, run the *tracker* and check the position residuals on the TFW. If required, modify the positions of the detectors accordingly. One must also keep in mind the fragment mass distribution, i.e be sure that the peaks are in their right positions.

- Use the *have/want* feature of the *tracker* to fine tune the fragment mass spectrum.

As a result of the calibration, using the *tracker* on a CH_2 run, the following fragment mass distribution was obtained, with a mass resolution of 1.9% for the ^{11}Be nucleus.

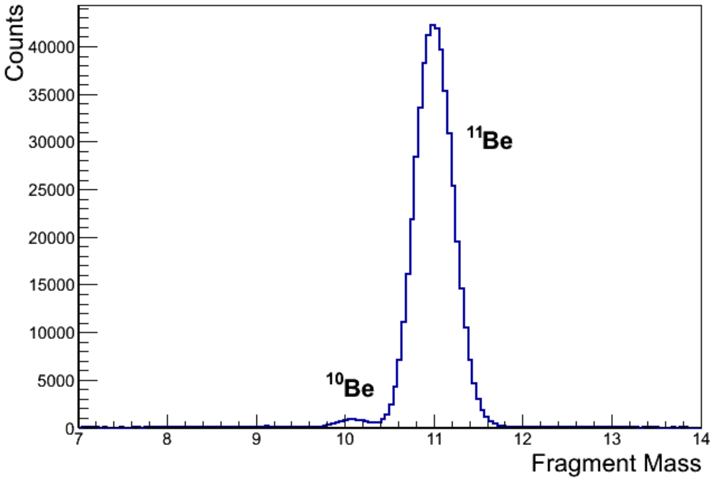

Figure 3.20: Reconstructed fragment mass spectrum obtained with the tracking routine. A resolution of 1.9 % was achieved for ^{11}Be.

Chapter 4

Analysis Methods

This chapter describes the method used to select the reaction channel and to obtain the physical quantities of interest.

First, the tagging of the reaction channel is achieved by means of the identification of the nuclei of interest before and after the target. Once the identification is concluded it is possible to calculate the corresponding momentum distributions and cross sections. At this point, it is necessary to take into account the presence of carbon in the polypropylene (CH_2) target which demands a background subtraction aiming at the removal of the events that resulted from the interaction with the carbon.

The last part of this chapter will focus on the γ-ray reconstruction using an *addback* algorithm. This algorithm allows to cluster and sum the energy deposited in several neighboring crystals and reconstruct the energy deposited in one event.

4.1 Nuclei Identification and Selection

The reaction channel gate was applied by means of the identification of the nuclei of interest before and after the target. In particular, the selection gates focused on isotope mass and energy loss correlations.

Positioned before the collision target, the S8, POS and PSP inbeam detectors allow to characterize the beam entering the setup. The energy deposited in the PSP detector combined with the time-of-flight (tof) information provided by the POS and the S8 scintillator allows the identification of the different nuclei present in the beam as shown in Figure 4.1. An elliptical gate was applied in order to select the incoming ^{11}Be projectile characterized by an atomic charge of 4 and a mass-to-charge ratio of 2.75. At the same

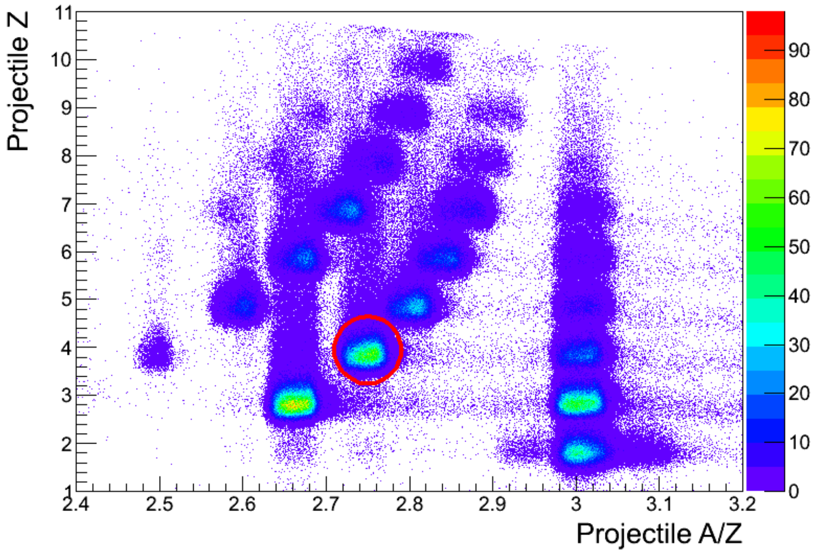

FIGURE 4.1: Particle identification plot of the cocktail beam entering Cave C, during the ^{22}O FRS setting. Identified is the ^{11}Be projectile (Z=4 and A/Z=2.75).

stage of the previous gate, a charge selection was performed using the energy deposit on the SSTs placed before the target, see Figure 4.2. This particular selection is carried out in order to reject possible reactions that occurred between the PSP and the target.

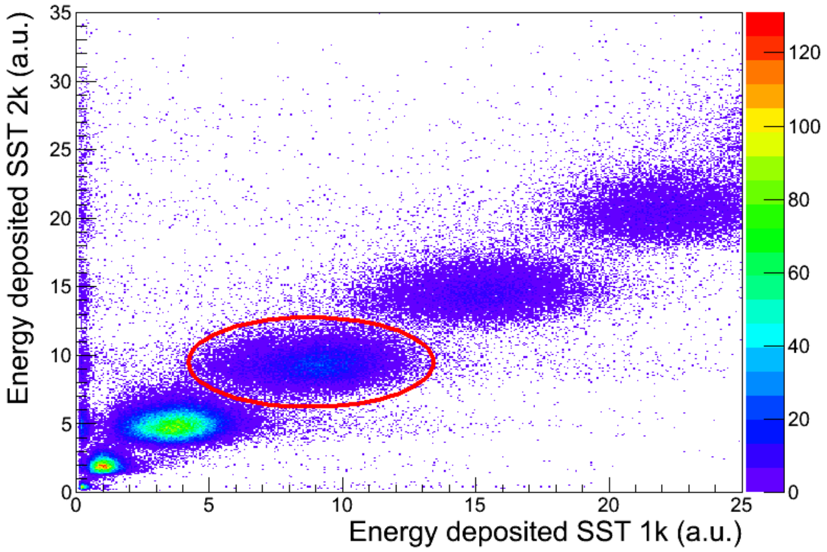

FIGURE 4.2: Energy deposited in the SSTs placed before the target, SST 1 and 2. The different regions identify different atomic charges. The ellipse drawn surrounds the nuclei of atomic charge 4 (Beryllium).

After the target, the different charges are identified via energy loss in the outgoing SSTs and the TFW detectors. While the fragment mass is obtained by means of the fragment velocity and trajectory according to

$$B\rho \propto \frac{A}{Z}\beta\gamma. \tag{4.1}$$

Where B is the magnetic field, ρ the particle trajectory, $\frac{A}{Z}$ the mass-to-charge ratio of the particle, β the nominal velocity of the particle and γ, the Lorentz factor. The field map of the ALADIN dipole magnet has been measured, therefore is it possible to determine the $B\rho$ for a certain current and trajectory. The β velocity was determined via the flight path and tof between the target and the TFW detector.

Finally, the nucleus charge was determined through the energy loss in TFW, leaving the fragment mass an accessible quantity. The identification of the fragment mass was done using a software tool of the collaboration, the *tracker* (described in the previous chapter).

The outgoing fragment charge tagging was carried out through the correlation between the energy deposited in one of the SSTs after the target and the TFW detector, shown in Figure 4.3.

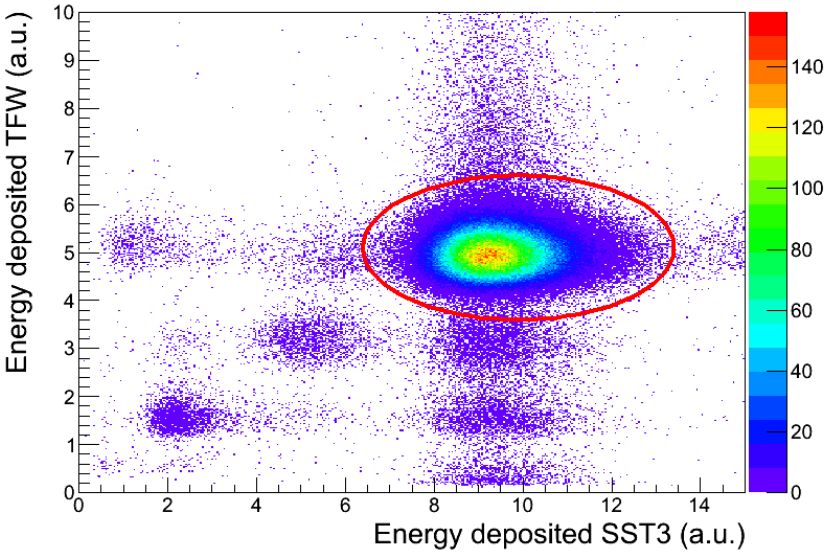

FIGURE 4.3: Correlation of the energy deposited in the TFW and one of the Silicon detectors after the target. The ellipse drawn represents the cut applied to select Beryllium fragments after the reaction.

Regarding the selection of the ^{10}Be fragment, it is achieved applying an elliptical cut in the correlation of the fragment X-axis position on TFW and the fragment mass. This correlation as well as the gates applied are shown in Figure 4.4. The GFI detectors, also placed in the heavy fragment branch, were not taken into account due to their low efficiency for low charges [79].

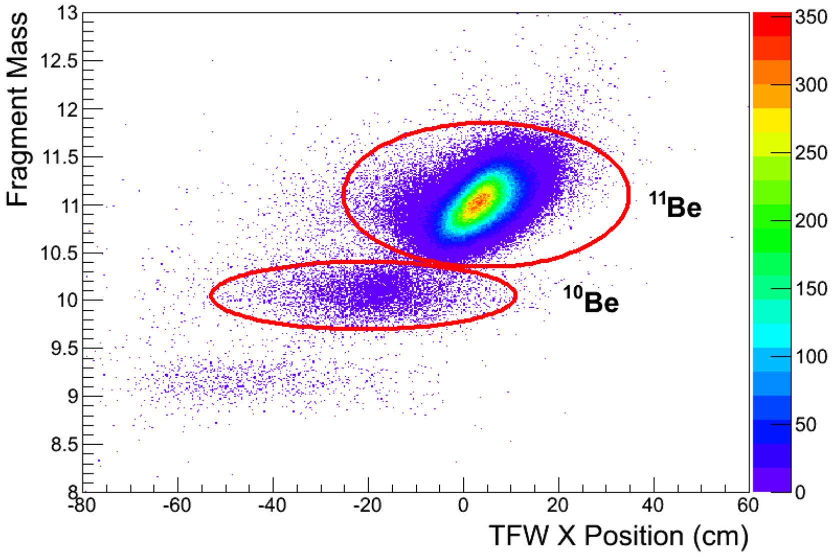

Figure 4.4: Fragment detected position in TFW and reconstructed mass correlation for an incoming ^{11}Be projectile. Identified are the elastic scattered or just unreacted ^{11}Be nuclei and the 1-neutron breakup resulting ^{10}Be fragment.

4.2 Momentum Distributions

The momentum ($\vec{P}$) of the fragment can be decomposed in two components, longitudinal ($\vec{P}_{||}$) and transverse ($\vec{P}_{\perp}$) and $\vec{P}$=$\vec{P}_{||}$+$\vec{P}_{\perp}$. The longitudinal component is parallel with respect to the direction of the incoming projectile, while the transverse component is perpendicular.

In order to extract the different components one must considered the projections on the X, Y and Z axis. In the LAND/R^3B setup, the Z axis is defined along the beam, X perpendicular to Z and parallel to the floor while Y is perpendicular to the beam direction and to the floor. Within this coordinate system the longitudinal momentum corresponds to P_Z and the transverse momentum is the sum of the P_X and P_Y components,

$$P_{\perp} = \sqrt{P_X^2 + P_Y^2}. \tag{4.2}$$

Regarding the absolute value of the total momentum, this quantity is obtained via the tracking routine following the relation

$$P = \gamma \cdot m_{frag} \frac{Flight\,Path}{ToF}. \tag{4.3}$$

where the flight path and tof considered are measured between the target and the TFW detector and $m_{fragment}$ is the rest mass of the fragment in our case ^{10}Be.

The P_Z component can be determined in the laboratory frame or in the centre of mass frame of the particle. The later is obtained following

$$P_Z^{cm} = \gamma_{proj} \cdot (P_{Z_{fra}} - \beta_{proj} \cdot \gamma_{fra} \cdot m). \tag{4.4}$$

In the previous equation γ_{proj} and β_{proj} are the Lorentz factor and nominal velocity of the incoming projectile, $P_{Z_{fra}}$ is the Z component of the momentum of the fragment, γ_{fra} and m are the Lorentz factor and mass of the fragment.

The X and Y components of the momentum are obtained through the projection of the total core momentum in the corresponding axis:

$$\begin{aligned} P_X &= P \,.\, sin(\delta_{X,out} - \delta_{X,in}), \\ P_Y &= P \,.\, sin(\delta_{Y,out} - \delta_{Y,in}), \end{aligned} \tag{4.5}$$

where $\delta_{X,out}$ ($\delta_{Y,out}$) and $\delta_{X,in}$ ($\delta_{Y,in}$) are the angles of the outgoing and incoming particles, respectively, determined in the XZ (YZ) plane with respect to the Z axis. The angles are determined using the hit positions in the SSTs, after not only calibrating the detectors but also doing a relative alignment, already presented in section 3.5.

4.3 Background Subtraction

In this work we aim to study neutron knockout of ^{11}Be from the collision of a projectile with a proton target. Due to its high density of protons a polypropylene (CH_2) target was used. Therefore the collisions with the carbon present in the CH_2 and the contributions of the setup must be taken into account in order to correctly determine the physical quantities of interest. To achieve this, during the experimental campaign a pure graphite as well as an empty target setting runs were recorded. However, in this work the empty target contamination could not be considered as no data was acquired considering an empty target for the ^{22}O FRS setting (FRS setting in which ^{11}Be was abundant).

The background subtraction procedure consisted on two normalizations: the first regards the number of incoming particles impinging on the target during the considered setting; the second takes into account the number of active centers present in each target, (τ). The number of active targets is defined as

$$\tau_{target} = \frac{d_{target} \cdot N_A}{M_{target}}, \tag{4.6}$$

where d_{target} is the density of the target in g/cm^2, M_{target} the molar mass of the target compound in g/mol and N_A the Avogadros constant.

After normalizing to the number of events of interest for each target setting, the contribution of the events that reacted with the carbon present in CH_2 has to be deducted. The background subtraction is carried out, providing the number of reactions, X, according to

$$X = N_o^{CH_2} - N_i^{CH_2} \frac{N_o^{carbon}}{N_i^{carbon}} \cdot \frac{\tau_{CH_2}}{\tau_{carbon}}. \tag{4.7}$$

Where N_i is the number of ions impinging on the target, N_o the outgoing number of detected particles and τ the number of active targets.

Regarding the number of active centers present in each target, in the S393 experiment and for the ^{22}O setting, the properties of two targets considered are in Table 4.1.

Target	Thickness (mg/cm^2)	Molar Mass (at/mol)
CH_2	922	14.02
Carbon	935	12.01

TABLE 4.1: Target characteristics of the ^{22}O setting of the S393 experiment.

The fragment mass spectra for a CH_2 and carbon target settings as well as the effect of the backgroung subtraction are shown in Figure 4.5. After the background subtraction, the number of ^{11}Be projectiles is negligible proving the correct normalization to the number of impinging particles for each target.

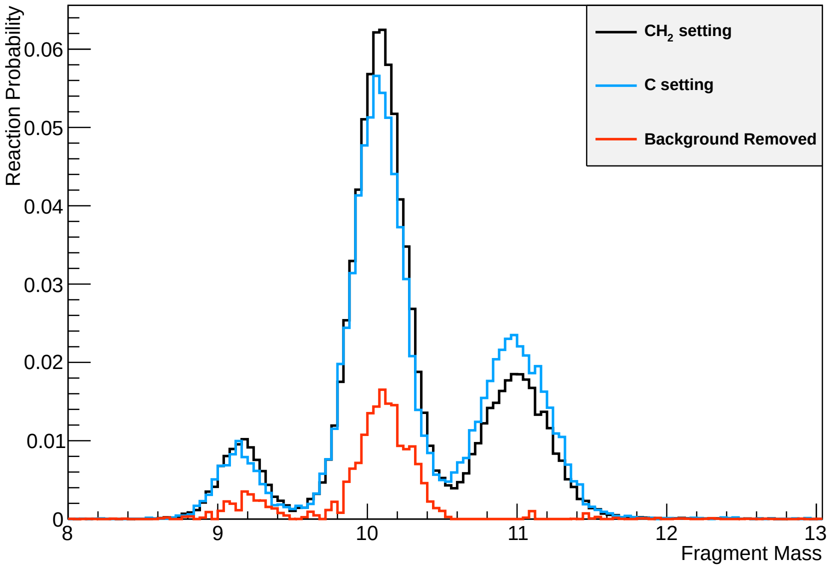

FIGURE 4.5: Fragment mass spectrum before and after background subtraction. This procedure removes the contribution of possible events that occur in the carbon present in the CH$_2$ target.

4.4 Total Cross Sections

The total integrated cross-section represents the likelihood of a certain event to occur. In this study it is determined the reaction cross section on a proton target. In order to obtain the later observable, the probability of reacting with the carbon target must be accounted for and subtracted,

$$\sigma_{H_2} = \sigma_{CH_2} - \sigma_{carbon}. \tag{4.8}$$

The reaction cross section is determined from the ratio between the number of reacted events (N$_o$) and the number of incoming ions (N$_i$) impinging on a target with a given number of active centers per cm^2, τ_{tg}. The cross section for a given target, σ_{tg}, can then be determined using

$$\sigma_{tg} = \frac{N_o}{N_i \cdot \tau_{tg}}. \tag{4.9}$$

The correct determination of the number of ions (N$_i$ and N$_o$), from the number of detected ions (N$_d$), must consider the geometric and detection efficiency, ϵ, as well as the downscale factor (DSF) defined in the considered trigger pattern, e.g. $N_i = \epsilon \cdot DSF \cdot N_d$. Due to similar event selection criteria, such corrections may apply when counting N_i and N_o events. In that case, the correction is canceled out. In fact, event selection is carried out similarly for most of the detectors, except for the Crystal Ball.

Replacing Equation (4.9) in Equation (4.8) one obtains

$$\sigma_{H_2} = \frac{N_{oCH_2}}{N_{iCH_2} \cdot \tau_{CH_2}} - \frac{N_{oCarbon}}{N_{iCarbon} \cdot \tau_{carbon}}. \tag{4.10}$$

Finally, to obtain the reaction cross section on a proton target, one must consider the number of protons in CH$_2$, $\sigma_H = \frac{1}{2} \cdot \sigma_{H_2}$.

4.5 Cluster Identification in Crystal Ball

The Crystal Ball detector can be used to measure protons and neutrons in coincidence allowing to tag quasi-free knockouts. However, one is not able to identify if the detected nucleon is either a proton or a neutron. It also allows to measure the energy deposited by a γ-ray emitted by a reacting nucleus. In both cases, the energy can be deposited in several neighbouring crystals of the detector. Therefore, an addback algorithm is used to reconstruct the total energy deposited.

4.5.1 Addback Algorithm

In an event-by-event basis, the addback algorithm orders systematically the crystals by the maximum energy deposited into a list.

Starting from the first position of the sorted list, i.e, from the crystal with the highest energy deposited, the routine checks the type of particle whether it is a proton or a γ-ray.

In the case of a proton, the energy deposited in the proton branch is finite and above a minimum energy threshold that can range from 6 to 23 MeV. In addition, the energy collected in the γ branch is above a certain maximum threshold or is characterized by an overflow. In the case of a γ-ray, the energy deposited in the γ branch must be finite, above a minimum threshold ranging from 80 to 400 keV and bellow a maximum energy threshold. In this work the maximum energy threshold for a γ-ray was 17 MeV which also defined the minimum energy threshold required to detect protons.

The algorithm will search through the list for neighboring crystals of the identified first crystal. If these exist, their energy will be added and the crystals are eliminated from the list.

The set of crystals found form a cluster and its energy is the sum of the energies deposited in the crystals that are part of it. The cluster angle is the center angle of the crystal with maximum energy.

In the case of gammas, the angular information (θ) is crucial because the gammas emitted by relativistic energy nuclei suffer the Doppler effect. The center of mass energy (E_{cm}) is determined from the measured deposited energy in the laboratory (E_{lab}) must be correct according to

$$E_{cm} = E_{lab} \cdot \gamma \cdot (1 - \beta cos\theta), \tag{4.11}$$

where γ is the Lorentz factor, β the nominal velocity of the emitting nuclei and θ is the emission angle of the γ in respect to the direction of the nuclei.

Regarding the proton angles, a randomization of the angles is carried out following the work of [85], which allows to account for the non-uniform shape of the crystals.

4.5.2 (p,pn) channel in inverse kinematics

Up to this point, the previous algorithm is capable of identifying protons and neutrons emerging from the reaction providing its energy and angular information. This fact allows to pursue the (p,pn) channel using the Crystal Ball detector.

In previous experiments at the R^3B setup, the identification of proton and neutrons was performed with the aid of the SSTs surrounding the target. However, during S393 these detectors were not operating. As a result, it was not possible to clearly distinguish a proton from a neutron. In addition, the angular resolution of the emitted nucleons was limited to the Crystal Ball resolution.

The (p,pn) event requires the identification of two nucleon clusters. Figure 5.2 presents the results of the simulation of the (p,pn) reaction in Crystal Ball, using kinematic simulations developed by [86]. It shows a dominant contribution for the opening angle of the emerging nucleons to be around 90° and in the azimuthal angle, and that the nucleons travel back to back, revealing an azimuthal angle difference of approximately 180°. These features were also obtained theoretically for the case of nucleon knockout from ^{12}C at 400 MeV/u [87].

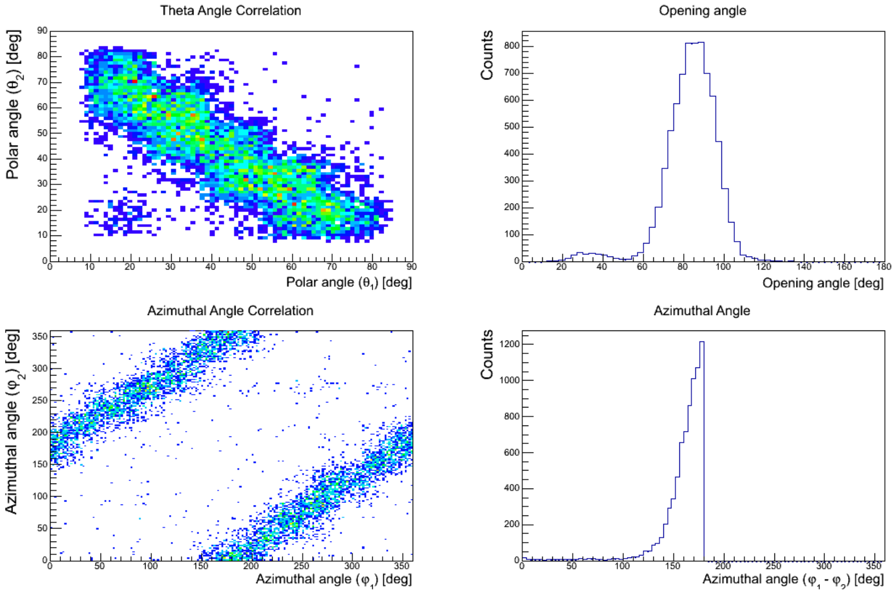

FIGURE 4.6: Simulated ^{11}Be(p,pn)^{10}Be azimuthal and polar correlations on Crystal Ball.

The previous figure can be compared with the data collected in experiment S393 for the ^{11}Be projectile for both CH$_2$ and carbon targets. The correlations in theta and azimuthal angles for the CH$_2$ and carbon targets are shown in Figures 4.7 and 4.8. It can be seen that for the Carbon target the correlations are not so strong, in particular for the polar angle where a broader peak appears.

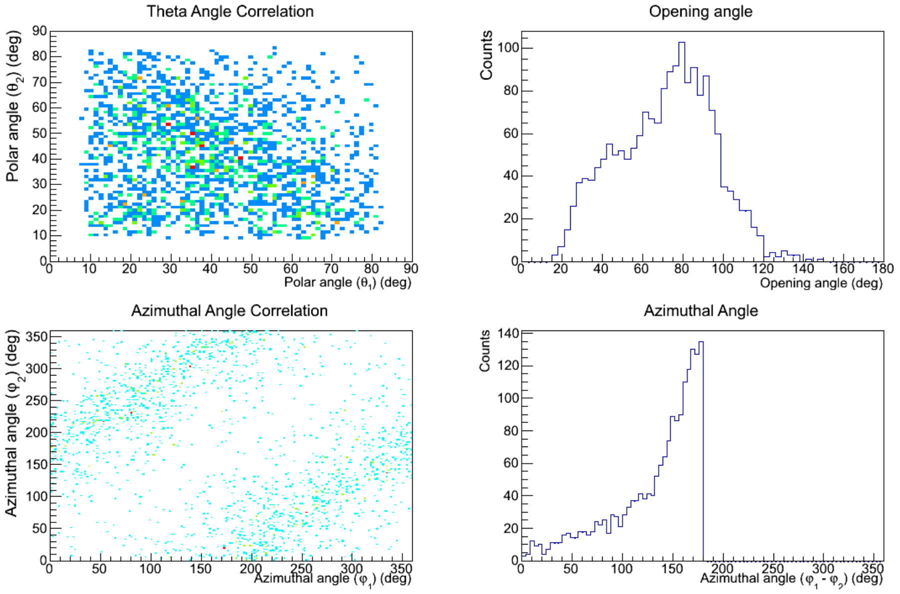

FIGURE 4.7: Azimuthal and polar correlations of the nucleons emitted form the ^{11}Be(p,pn)^{10}Be reaction measured in Crystal Ball using the CH$_2$ target.

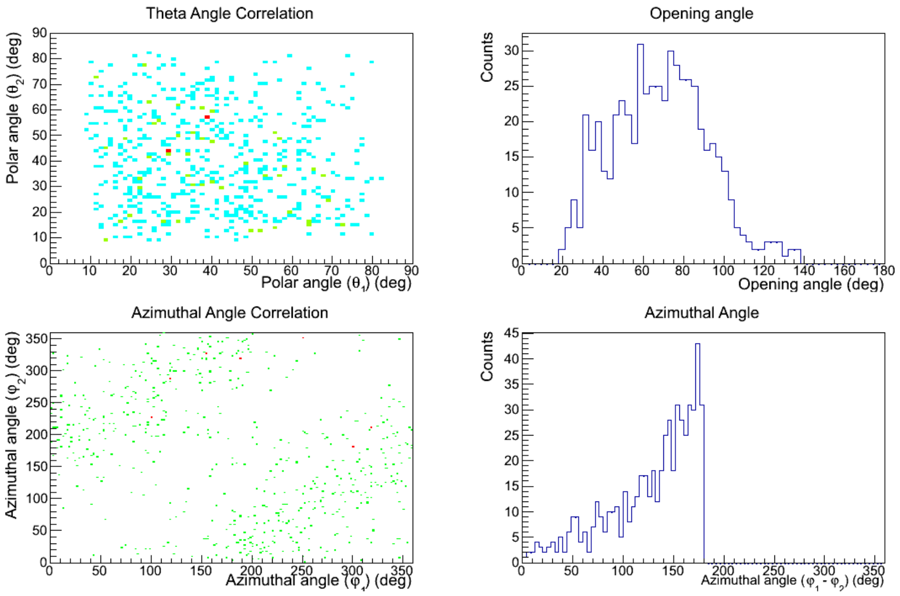

FIGURE 4.8: Azimuthal and polar correlations of the nucleons emitted form the ^{11}Be(p,pn)^{10}Be reaction measured in Crystal Ball using the carbon target.

Chapter 5

R3BROOT Simulations

The extraction of the physical quantities of interest requires the evaluation of the response of the experimental setup to different particle interactions. This characterization aims at the determination of detection efficiencies.

In this chapter, it will be covered the Crystal Ball detector response to a proton, a neutron and γ-rays. We will only cover this detector system because its efficiency must be considered in the determination of the number of events where two nucleons stemmed from the (p,pn) reaction. This information is crucial in the determination of the cross section. All the other detector systems are also relevant, however the quantities extracted do not depend on the efficiency, as it is the same.

The efficiency was determined by means of simulations. This needs to be considered when there is no real way to perform measurements that allow for a parametrized efficiency determination.

The simulations performed used GEANT4 for the transportation and the geometry of the detectors. They also allow to introduce events with the physical characteristics of the physics one wants to study, in this case correlated hadrons at relativistic energies and photons isotropically emitted. The photons are affected by the Lorentz boost due to the relativistic velocity of the particle that emits them.

During the development of this work several discussions took place regarding the physics lists being used in the simulations. We shall return to this point later.

5.1 The R3BRoot Framework

The different experiments at the FAIR facility can be simulated using the FairRooT [88] simulation software package or framework. It is fully based on ROOT [83] and supports Geant3 and Geant4 [89, 90] particle transport engines.

The FairRooT framework allows the user to implement new detectors or to use existing ones and perform simulations or/and analysis tasks. In particular, the R3BRoot framework within FairRooT has been developed for the future R^3B setup at Fair [88]. These frameworks also intent to be an analysis framework.

The R^3B/LAND detectors are implemented in R3BRoot and this allows to study their response to particle interactions. For the present study we are interested in the response of the Crystal Ball detector to protons, neutrons and photons. Nevertheless, the present chapter will only focus on the simulations of protons and neutrons.

5.2 (p,pn) Simulations in Inverse Kinematics

The simulations considered in this work involve the 159 NaI crystals that compose the Crystal Ball detector. Each crystal has a length of 20 cm and covers a solid angle of $\approx$77 msr. This detector allowed the detection of recoil protons and neutrons and the in-flight emitted photons from excited fragments at angles larger than $\pm 7^\circ$ in the laboratory frame. Each crystal is connected to a photomultiplier for the detection of photons. In addition, the 64 most forward crystals have an additional lower-gain readout which allows to detect the protons and neutrons emerging from the knockout reaction.

The simulations aim to predict the detection efficiency by comparing the number of reconstructed events after the simulation with the total number of events simulated. At this point we are interested in the simulation of the proton that scattered from the target and the neutron from the projectile as if both particles are free.

The information of the proton and neutron is provided by a so-called event generator. The event generator must characterize the particles of interest by particle ID, 3-momentum and direction for each event one intends to simulate.

The standard R^3B/LAND Event Generator is a kinematical code, here denoted as KinEG[1], describing (p,pn) and (p,2p) reactions assuming the QFS reaction mechanism. It was developed by L. Chulkov at GSI and later adapted to C++ by V. Panin [86].

---

[1] Kinematical Event Generator

The KinEG, based on the Goldhaber model, requires as input the energy of the projectile and the masses of the projectile, spectator and the 2 emitted nucleons such is the case of (p,2p) or (p,pn) reactions. It calculates the width of the momentum distribution, σ, according to

$$\sigma^2 = \sigma_0^2 \, \frac{A_f \cdot A_n}{(A_f + A_n)},$$

where A_f and A_n are the masses of the fragment and removed neutron, respectively. The σ_0 constant is related to the nucleon separation energy by $\sigma_0 = \sqrt{2 \cdot S_n}$.

The KinEG also considers the possibility of an isotropic or non-isotropic emission of the knockout nucleon. The isotropic emission is suited for the (p,2p) reaction while the non-isotropic is suited for the (p,pn), according to [91, 92]. Using the KinEG, the isotropic and non-isotropic distributions for the emitted nucleon were obtained, and are plotted for center of mass in Figure 5.1.

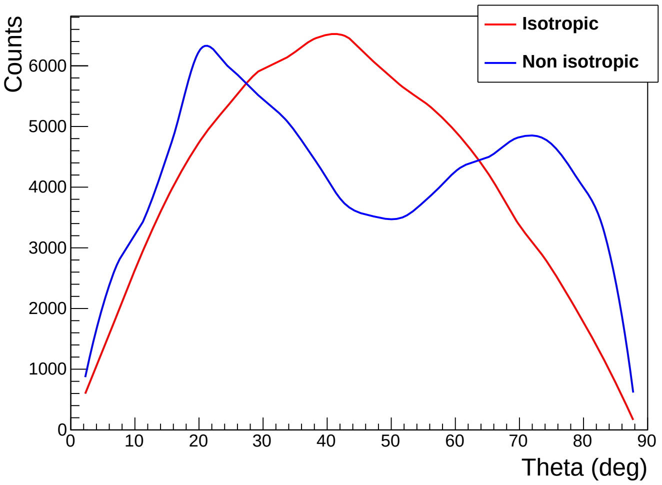

Figure 5.1: Isotropic and non-isotropic center of mass polar angle distribution of the emitted neutron.

This standard event generator was used to simulate the ^{11}Be(p,pn)^{10}Be reaction and the results are presented in Figure 5.2. As expected from the QFS mechanism features, the opening angle between the two nucleons peaks at around 84° and the difference in azimuthal angle of approximately 180° indicates that the neutron and the proton are emitted back-to-back.

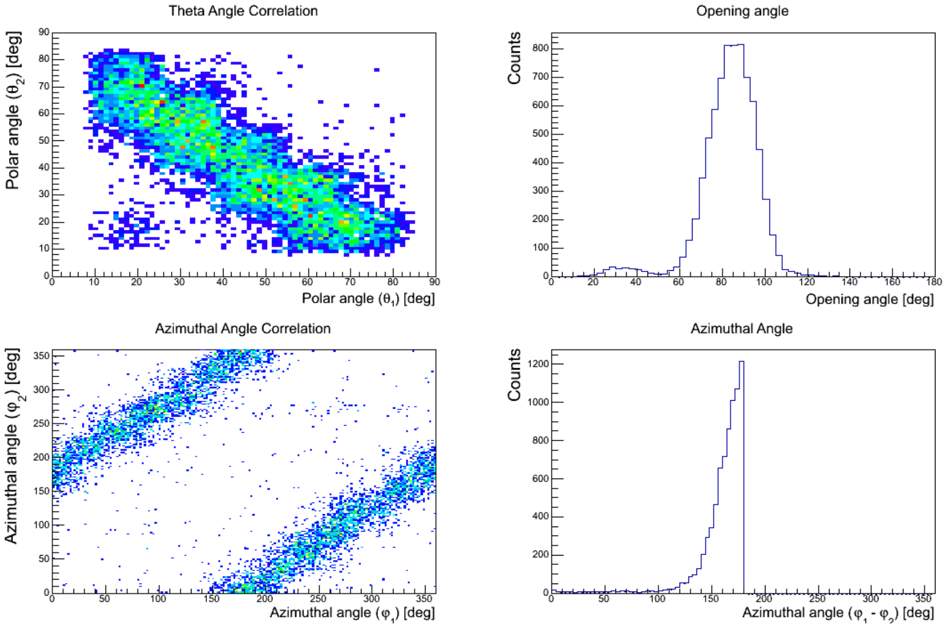

FIGURE 5.2: Simulated angular correlations of the neutron and proton resulting from the ^{11}Be(p,pn)^{10}Be reaction. On the left is shown the correlation in theta (top) and azimuthal (bottom) angles between the two nucleons. On the right is presented the opening angle (top) and the difference between the two nucleons in azimuthal angle(bottom)

5.3 Proton and Neutron Response of Crystal Ball

During the S393 experiment the Silicon Strip detectors placed as a box around the target, as shown in Figure 2.7, were not properly operating, thus, making it impossible to discriminate between protons and neutrons. This lead to an attempt to characterize Crystal Ball response to the different nucleons separately.

For the following study, it was used as the input file of the simulation the same file considered for the ^{11}Be(p,pn)^{10}Be reaction. The particle ID allowed to exclude one nucleon at a time in order to simulate separately the different nucleons.

Figure 5.3 presents the response to protons and neutrons. Three major differences are revealed: neutrons present larger theta/polar angles, θ, smaller reconstructed cluster energy and a larger number of crystals fired than protons. The protons punch through is in high evidence in Figure 5.3a around 150 MeV.

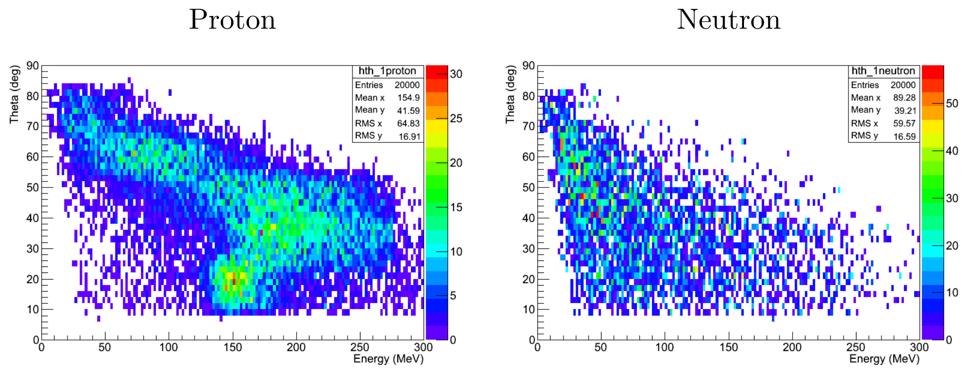

(a) Theta-energy correlation (b) Theta-energy correlation

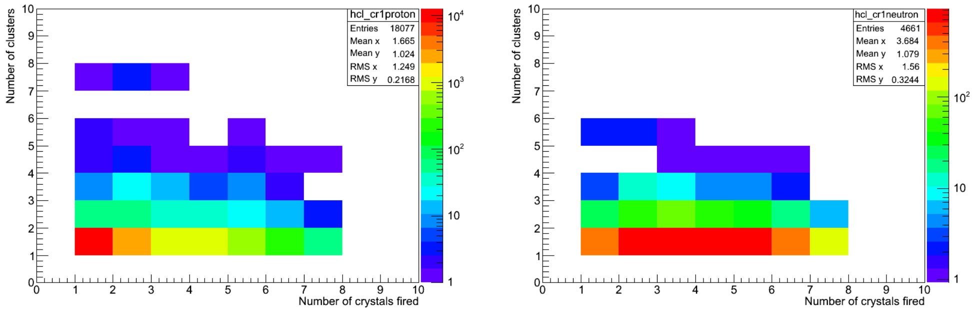

(c) Cluster-crystal number (d) Cluster-crystal number

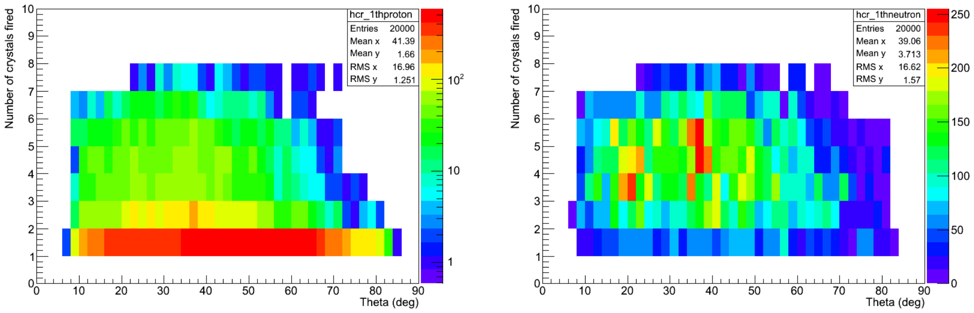

(e) Crystal-theta correlation (f) Crystal-theta correlation

FIGURE 5.3: Individual simulation of protons (left) and neutrons (right) emerging from the quasi-free scattering $^{11}Be(p,pn)^{10}Be$ reaction.

The next study considers a (p,pn) simulation, where only two clusters are expected and reconstructed and also keeping in mind that the addback algorithm performs a descending energy sorting. It is reasonable to expect that the highest cluster energy is located in the cluster that is defined first. From here on, cluster 1 is the first cluster formed and cluster 2 the second expected cluster on a (p,pn) event reconstruction.

Figure 5.4 presents several correlations for cluster 1 and cluster 2, similar to those presented in Figure 5.3. Here it is shown that cluster 1 presents larger energy deposited, smaller theta angle and fewer number of crystal fired as shown for in protons in Figure 5.3. The cluster multiplicity histogram (5.3c and 5.3d) was replaced, as the cluster multiplicity is selected as 2 for the (p,pn) reaction channel.

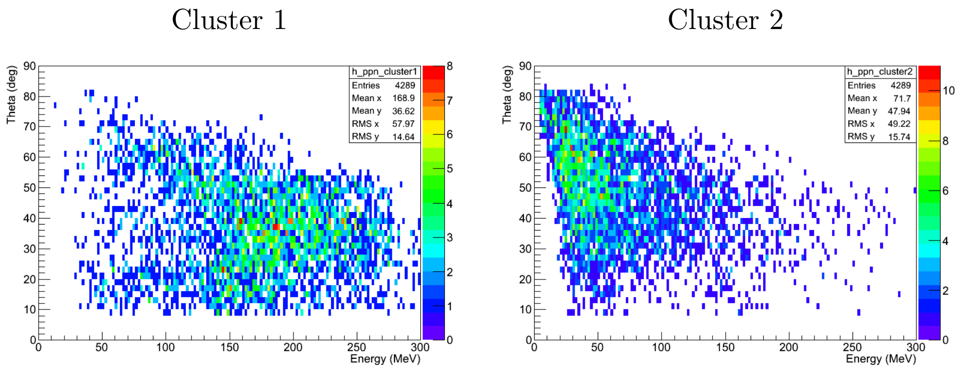

(a) Theta-energy correlation (b) Theta-energy correlation

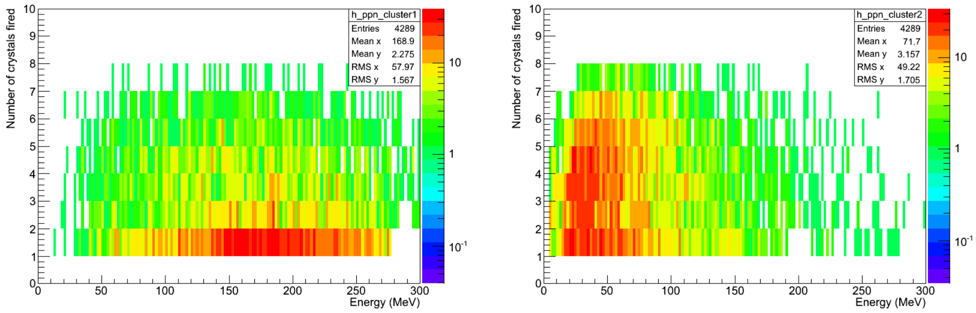

(c) Crystal-energy correlation (d) Crystal-energy correlation

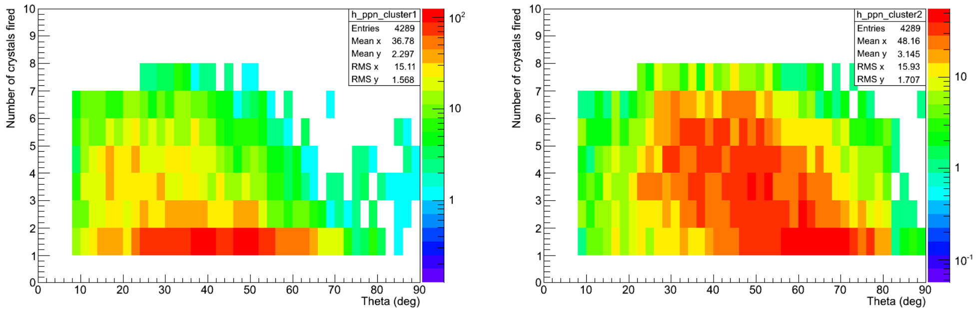

(e) Crystal-theta correlation (f) Crystal-theta correlation

FIGURE 5.4: Simulated nucleon cluster angular, energy and crystal number correlations in which cluster 1 corresponds to the highest energy deposition.

Regarding experimental data, the same conditions were applied and cluster 1 and 2 investigated. The correlations are presented in Figure 5.5. Here, once again, the cluster 1 can be associated to the response of a proton and cluster 2 of a neutron. In any case, this study is not sufficient and only a comparison with data acquired in the SSTs can shed light on this subject.

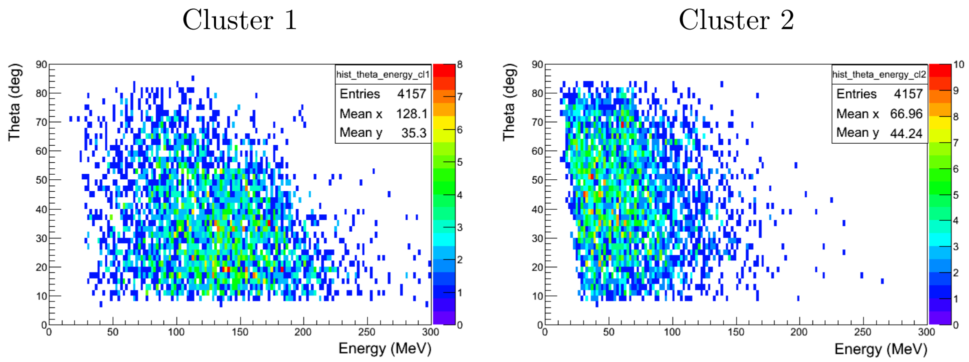

(a) Theta-energy correlation (b) Theta-energy correlation

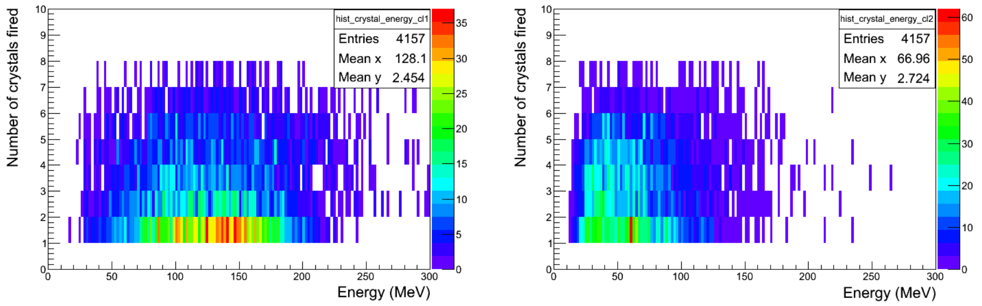

(c) Crystal-energy correlation (d) Crystal-energy correlation

FIGURE 5.5: Nucleon cluster angular, energy and crystal number correlations of experimental data, where cluster 1 corresponds to the highest energy deposition followed by the second in cluster 2.

5.3.1 Efficiency Response

The efficiency of the (p,pn) reaction, mentioned in this work as neutron knockout is characterized by detecting one proton and one neutron simultaneously. In this case the efficiency is determined by the number of events after the addback reconstruction with a nucleon multiplicity of 2, divided by the total number of simulated events.

During the conclusion of this work the debate of the physics lists (pl) been used in the simulations was open. In fact, it was seen a dependence of efficiency with the pl used.

The physics lists are classes containing the physics models, the particle types and the cross sections required in a particular simulation [89, 93].

In this work several physics lists were used to determine the efficiency. In all cases, the core packages used are *decay*, *elastic*, *gamma_nuc*.

There are two main categories of physics lists: electromagnetic and hadronic physics. The simulation of electromagnetic interactions concerns the physics processes for photons, electrons and positrons. While the Penelope model has been developed for low energy phenomena (atomic effects), the standard class is also an option for a wider range of energies.

Hadronic physics treats reactions triggered by long lived hadrons, such as protons, neutrons and γ-rays in the 0 to 1 GeV energy range. Three main models are available in this category: Binary, Bertini and INCL++ (the Liège Intranuclear Cascade).

In the case of the Binary model (binary_ion) the interactions occur between a primary and a secondary particle and an individual nucleon of the nucleus. Experimental data are used to in the calculation of the total, inelastic and elastic cross section. Numerical solutions of the equations of motion are used to the determine the propagation of particle in the nuclear field. The cascade stops as soon as an energy threshold is reached.

The Bertini model (qgsp_bertini) as been widely tested against experimental data which the incident kinetic energy is between 100 MeV and 10 GeV. The cascade is triggered when an incident particle strikes a nucleon and produces secondary particles. In their turn, these also interact. The cascade stops when all particles escape the nucleus, if kinematicaly capable.

The INCL++ model (qgsp_inclxx) is best suited in simulations where light-ion-induced reactions and spallation reactions play a dominant role. The transport of the nucleons inside the nucleus are fixed at the beginning of the simulation. The nucleus is simulated as a Fermi gas in a static potential well with a realistic density. This model minimizes the number of free parameters. The limitations of this model rely on the energy range of the incident particle (1 MeV - 20 GeV) and the target nucleus. Particular attention was given to heavy and stable nuclei.

Independently of the cascade model, it is possible to choose two distributions for the emitted nucleon: isotropic and non-isotropic, shown in Figure 5.1. For (p,pn) reactions (proton-neutron scattering) the non-isotropic distribution should be considered [91, 92].

In this work several physics lists were used to determine the efficiency. It was also considered the isotropy of the neutron distribution. The values obtained are presented in Table 5.1.

The debate on this subject is still ongoing. Due to the uncertainties associated to the choice of the physics list. In this work, the efficiency adopted is (15.2±6.1)%, corresponding to the standard and Bertini physics lists and the error is determined as the relative difference to the efficiency obtained from using the INCL++ physics list.

PL	Packages used	Isotropic (%)	Non-isotropic (%)
1	standard + qgsp_bertini	17.6	**15.2**
2	standard + binary_ion	17.5	15.4
3	penelope + qgsp_bertini	17.4	14.5
4	penelope + binary_ion	17.3	14.3
5	standard + qgsp_inclxx	24.1	21.3
6	penelope + qgsp_inclxx	23.5	20.8

Table 5.1: Efficiency obtained for the different physics lists used in the simulations.

Chapter 6

Results and Discussion

In this chapter we present and discuss the observables measured during the S393 campaign of the neutron knockout of ^{11}Be from the interaction with a proton target. These include total knockout cross-sections, differential core momentum distributions and the ^{10}Be energy spectrum.

We consider two types of analysis procedures that are related with the detected particles emerging from the collision process: (i) particle inclusive neutron knockout where only the heavy fragment is detected, (^{11}Be(p,X)^{10}Be), often referred neutron removal ^{11}Be(-1n); (ii) particle exclusive neutron knockout where the light particles and heavy fragments are detected, (^{11}Be(p,pn)^{10}Be). For this case, the light particles emitted from the reaction are detected using the Crystal Ball detector.

We compare the measured and calculated observables using the Faddeev/AGS reaction formalism assuming that other channels are negligible.

6.1 Particle Inclusive ^{11}Be Neutron Knockout, ^{11}Be(p,X)^{10}Be

The particle inclusive ^{11}Be neutron knockout reaction only demands the identification of the ^{11}Be projectile and the ^{10}Be fragment, disregarding the proton and neutron detection in Crystal Ball as well as the final state of the fragment.

The beam diagnostic detectors (POS, S8, PSP and the SSTs) allow to identify and select the ^{11}Be isotope from the cocktail beam. After the interaction with the target the energy loss information as well as the reconstructed heavy fragment mass are used to select both ^{11}Be and ^{10}Be isotopes among the fragments produced as described in Section 4.1. This is achieved using the detectors present in the heavy fragment branch after the target (SSTs and TFW).

6.1.1 Heavy Fragment Momentum Distributions

Heavy fragment momentum distributions are a powerful tool to obtain information of the removed particle. In the case of the reaction of interest, the momentum distribution provides information on the halo ground state, among other neutron configurations that can be excited.

The different transverse momentum distributions were obtained for both unreacted and reacted heavy fragments using Equation (4.5). The inclusive momentum distributions of ^{11}Be reaction are shown for the different targets in Appendix C.2.

Using the the inclusive momentum distributions of ^{11}Be, the straggling of the beam through the various targets was investigated, and is presented in Table 6.1. This is an important verification as it may limit the the measurement of narrow momentum widths, characteristic of halo states.

	Momentum Straggling (MeV/c)	
Target	x direction	y direction
CH_2	36.1±2	22.9±3
Carbon	41.7±2	21.4±3

Table 6.1: Momentum straggling for ^{11}Be projectiles at 457 MeV/u considering CH_2 and carbon targets. The values were obtained when fitting the distributions with a gaussian function.

According to [56] and [57], the expected full width at half maximum (FWHM) for one-neutron knockout is 43.6±1.1 MeV/c and 45.7±0.6 MeV/c, respectively, which is within the limits imposed by the straggling. The discrepancy between the y and x direction is known and expected, in addition part of SST1 had operation issues [70, 85]. Due to this observation, the results presented hereafter only consider the projection in y direction. The direction representation in the LAND/R^{3}B setup is described in Section 4.2.

From the previous results, it is possible to determine the momentum widths, given as FWHM. The momentum distributions of the neutron removal of ^{11}Be considering CH_2 and carbon targets in y direction are presented in Figure 6.1.

In order to extract the momentum distribution width that actually resulted from the neutron removal reaction, the contribution from the straggling of the beam must be subtracted. In Equation (6.1), Γ represents the momentum width, and it shows how the subtraction of the momentum resolution is considered for the ^{11}Be(p,X)^{10}Be inclusive reaction,

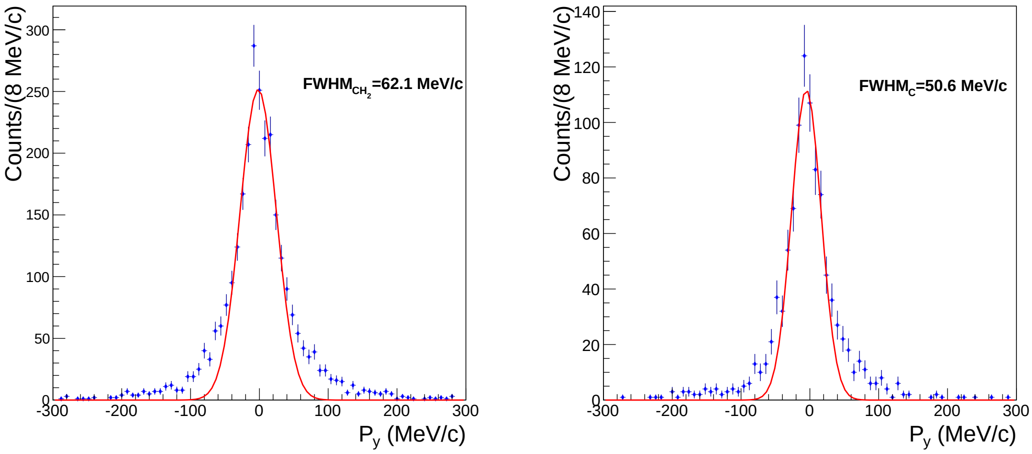

(a) CH_2, y projection

(b) Carbon, y projection

FIGURE 6.1: Heavy fragment transverse momentum distributions for the CH_2 and carbon targets runs of the ^{22}O setting, considering for the particle inclusive knockout reaction. The red line corresponds to a gaussian fit of the distribution.

$$\Gamma^2_{(^{11}Be(p,X)^{10}Be)} = \Gamma^2(^{10}Be) - \left(\frac{m(^{10}Be)}{m(^{11}Be)}\Gamma(^{11}Be)\right)^2. \tag{6.1}$$

The subtraction has to take into account the proportionality between momentum and mass (p $\propto$ m), therefore a normalization to the nuclear mass arises in the second term. Finally, the momentum widths for the ^{11}Be neutron removal reaction were determined for the CH_2 and carbon targets. The values are (44 ± 2) MeV/c for the former and (26 ± 3) MeV/c for the carbon target.

6.1.2 Cross Section

In this section, the results for the inclusive one neutron removal cross section of ^{11}Be impinging on a proton and carbon targets and requiring are presented.

The calculation of the cross section requires the evaluation of the number of fragments and projectiles detected, as shown in Equation (4.9). The detection of an ion needs to be corrected by the detection system efficiency (ϵ) i.e., the number of detected ions is a fraction of the actual number of ions that reached the detection system, $N_{detected} = \epsilon\, N_{total}$.

When considering the particle inclusive neutron knockout reaction as the isotopic number of the nucleus does not change, the detection efficiency of both projectiles and fragments is the same. In addition, it is a good approximation to consider that the number of incoming ions that reach the setup is the same as number of ions that did not react [85]. Therefore, for the cross section calculation, the number of incoming ions is taken as the number of ^{11}Be projectiles that reach the TFW and the number of ^{10}Be nuclei detected in the TFW constitute the number of the outgoing fragments.

When obtaining the integrated and differential cross sections, the procedure used to determine the number of impinging ions as well as the number of active centers was identical. The difference resides on the object used to determine the number of reacted ions, total number of counts or distribution. Taking into account the previous considerations, the integrated inclusive reaction cross section, $\sigma_{(^{11}Be(p,X)^{10}Be)}$, on a proton and carbon target, was determined and shown in Table 6.2:

	Cross Section (mb)
Target	Inclusive
Proton	52 ± 5
Carbon	189 ± 6

Table 6.2: Total reaction cross sections of inclusive one neutron removal of ^{11}Be on a proton and carbon targets.

In the cross section calculation, for both targets (tg), the error presented is a statistical error calculated as the quadratic sum of the individual errors of the number of projectiles and number of detected heavy fragments. It also includes the error on the determination of the target thickness which is of the order of 2%.

$$\delta_{tg}^2 = (\delta_{N(^{11}Be)_{tg}})^2 + (\delta_{N(^{10}Be)_{tg}})^2 + (\delta_{\tau_{tg}})^2$$

A study of the size of the gates applied to the reaction channel selection was performed. The size of the cuts of elliptical shape has an effect on the magnitude of the cross section. To evaluate this effect the value of the total cross section was obtained varying the size of the tagging cut applied by a constant factor, see Section 4.1. The effect of the gate size on the cross section is shown in Figure 6.2. A cut factor of 1.5 was chosen and the results presented in this work applied this gate size.

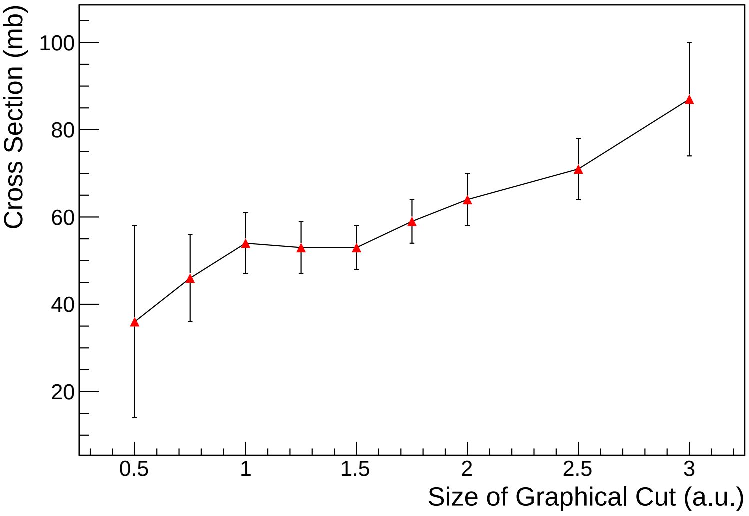

FIGURE 6.2: Variation of the total cross section with the reaction tagging sigma width cut applied.

The differential momentum reaction cross section was obtained and the result for the inclusive one neutron knockout on a proton target is shown in Figure 6.6. The integral of the distribution is 52 ± 5 mb.

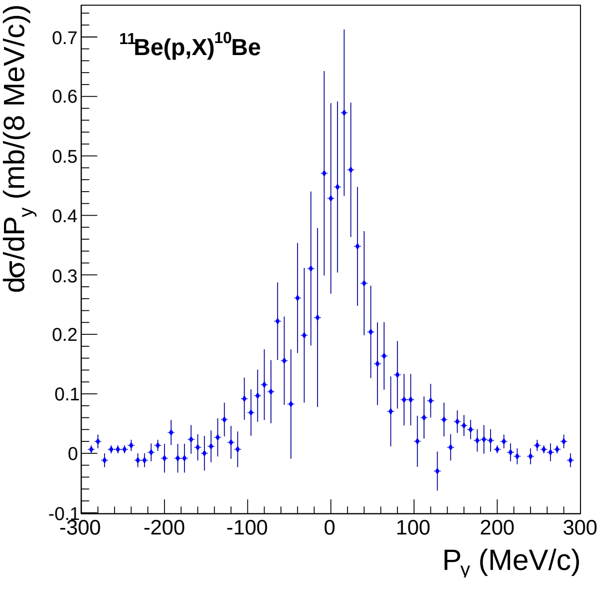

FIGURE 6.3: Differential momentum cross section for the inclusive neutron knockout reaction, (^{11}Be(p,X)^{10}Be). The integral value of the distribution is 52 ± 5 mb.

6.2 Particle Exclusive Neutron Knockout, ^{11}Be(p,pn)^{10}Be

The exclusive neutron knockout results presented in this section consider the reaction channel selection defined previously in Section 4.1 and also the detection of the proton and neutron emerging from the reaction in the Crystal Ball detector. Due to malfunctioning of the lateral (or box) SSTs, it was not possible to discriminate the proton from the neutron in this study.

The reaction tagging requirement was reduced to identifying a ^{11}Be projectile, a ^{10}Be fragment and a nucleon multiplicity of two in Crystal Ball. In terms of trigger patterns (Tpat) used in the data selection and described in Table 2.2, the impinging projectiles and reacted fragments were selected via the (Tpat&2) and the (Tpat&8) tag, respectively. The former indicating a measurement of a heavy fragment in the TFW detector placed along the heavy fragment arm of the setup. The (Tpat&8) tag associated with the detection of two nucleons in the Crystal Ball array surrounding the target.

The detection of two nucleons measured in Crystal Ball in coincidence with the ^{11}Be neutron knockout revealed the correlations shown in Figures 6.4 for the CH$_2$ target. In this figure, the expected nucleon correlations can be seen: an opening angle predominant at ≈90°, and a nucleon back-to-back emission ($\varphi_1 - \varphi_2$) revealed with the azimuthal angle peaking at ≈180°.

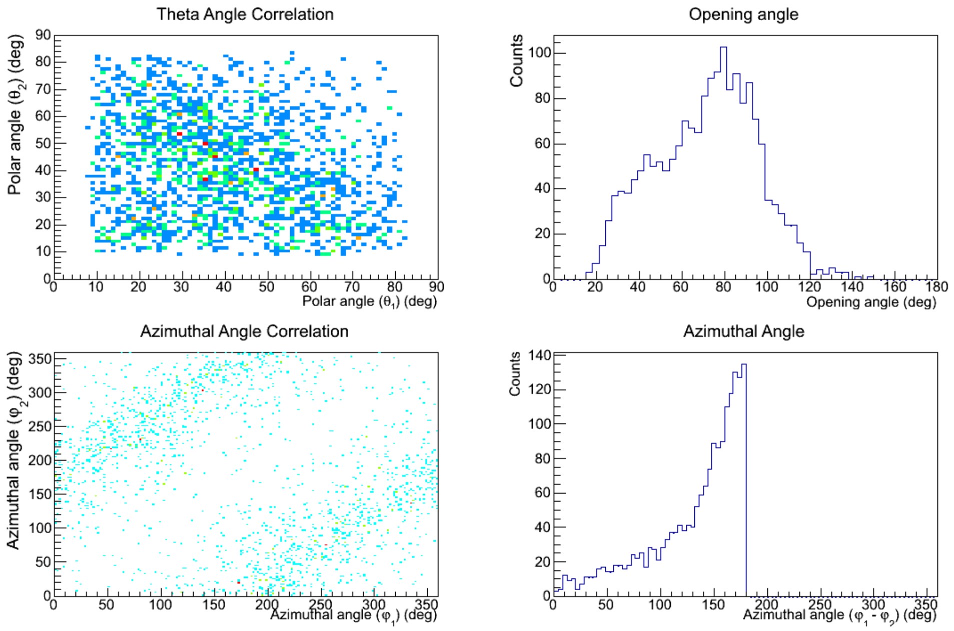

FIGURE 6.4: Nucleon angular correlations measured in Crystal Ball using the CH$_2$ target for the particle exclusive knockout.

6.2.1 Heavy Fragment Momentum Distributions

The transverse momentum distributions of the heavy fragment was obtained following Equation (4.5). In Figure 6.5 are presented the momentum distributions of the neutron knockout of ^{11}Be considering CH$_2$ and carbon targets in y direction.

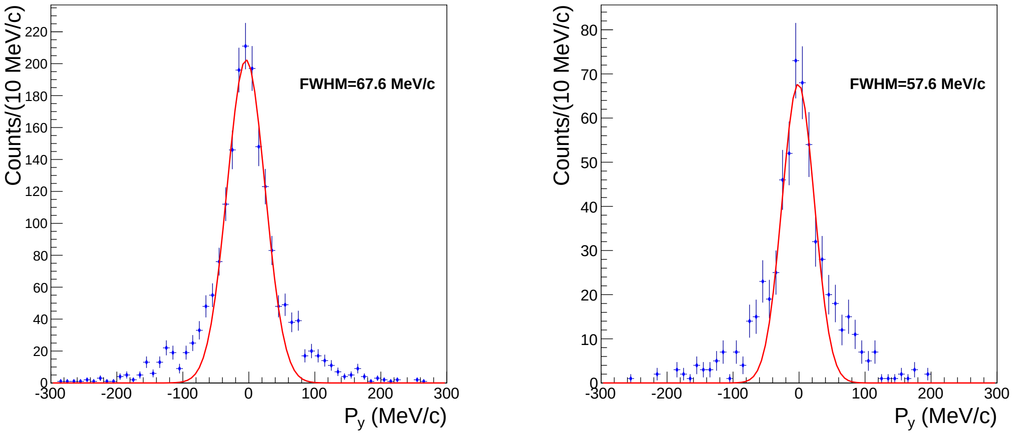

(a) CH$_2$, y projection (b) Carbon, y projection

FIGURE 6.5: Heavy fragment transverse momentum distributions for the CH$_2$ and carbon targets runs of the ^{22}O setting, considering the neutron exclusive knockout reaction (^{11}Be(p,pn)^{10}Be).

From this measurement, it is possible to determine the momentum distribution width. The contribution from the momentum resolution was subtracted using Equation (6.1) for the ^{11}Be(p,pn)^{10}Be reaction. The resulting widths of the momentum distributions are (51±2) MeV/c for the CH$_2$ target and (38±3) MeV/c for the carbon target.

6.2.2 Cross Section

The determination of the cross section of the exclusive neutron knockout reaction requires to take into account the efficiency of detecting a neutron and a proton in the same event. As this was not the procedure followed in the analysis, it was not possible to distinguish a proton from a neutron, the tagging applied consisted on the requirement of two nucleon signals, in the Crystal Ball detector.

Following the discussion presented in Chapter 5 about the detection efficiency of 2 nucleons in Crystal Ball, the efficiency obtained for the ^{11}Be(p,pn)^{10}Be reaction was $(15.2 \pm 6.1)\%$ using the KinGE event generator.

The integrated reaction cross sections on a proton and carbon targets were determined and are presented in Table 6.3:

	Cross Section (mb)
Target	Exclusive
Proton	37 ± 15
Carbon	92 ± 37

TABLE 6.3: Reaction cross sections of the ^{11}Be exclusive one neutron knockout, (^{11}Be(p,pn)^{10}Be), on a proton and carbon targets.

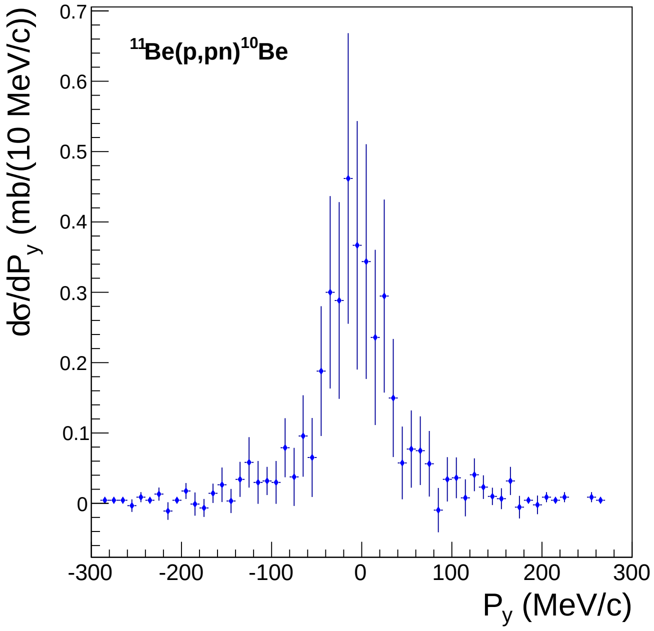

FIGURE 6.6: Differential momentum cross section of the ^{11}Be(p,pn)^{10}Be reaction. The integral value of the distribution is 37 ± 15.

6.3 Faddeev/AGS calculations

Considering knockout reactions in inverse kinematics, the intrinsic momentum distribution of the knocked out nucleon is reflected in the momentum distribution of the reaction heavy fragments. Moreover, the shape of the distribution is evidence of the nucleon orbital momentum. In the case of ^{11}Be(p,pn)^{10}Be reaction, the neutron is expected to be removed from the valence shell (s shell) or from an inner shell (p shell, associated to the ^{10}Be core) [94]. In Figure 6.7 it is shown a schematic representation of the contributions of the neutron knockout of ^{11}Be i.e., neutron removal from a valence shell or from the core (^{10}Be).

In this work we aim to compare the experimental results for the ^{10}Be momentum distributions and total cross sections with the theoretical results from the Faddeev/AGS reaction framework [95] that has been applied for the study of neutron knockout of light particles from the collision with a proton target [96–102]. Within this formalism it is

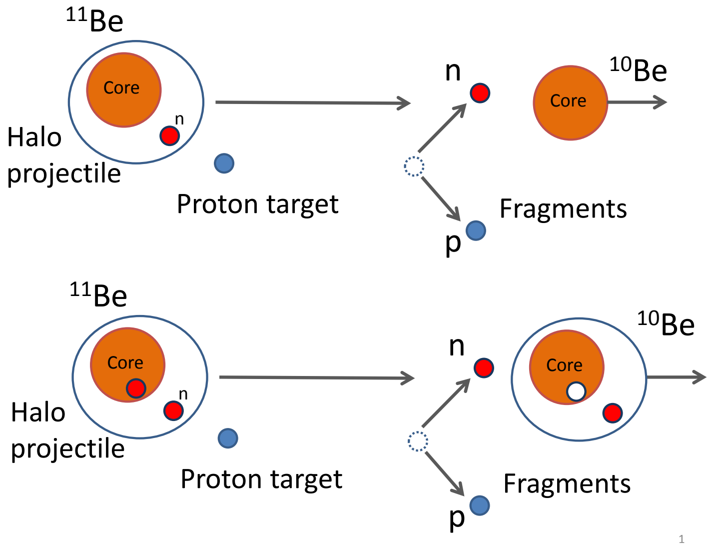

FIGURE 6.7: Schematic representation of the contributions to the knockout reaction.

assumed that ^{11}Be is described by an inert core (either in the ground state or in a excited state) and a particle. This formalism considers on equal footing all reaction channels and takes into account all interactions within all 3 particles (Core(^{10}Be), neutron and proton).

The ground state of ^{11}Be is assumed to be described as a weighted contribution of the core (^{10}Be) in the ground state coupled to a valence particle in the $2s_{1/2}$ configuration and the core in the 2^+ excited state couple to a valence particle in $1d_{5/2}$ configuration. In spectroscopic notation, the valence neutron can be given by
$|^{11}\mathrm{Be}_{g.s.}>= \alpha\cdot\, |^{10}\mathrm{Be}(0^+) \times \nu 2s_{1/2}> \, + \beta\cdot\, |^{10}\mathrm{Be}^*(2^+) \times \nu 1d_{5/2} >$.

The description of $|^{11}\mathrm{Be}_{g.s.}>$, used in this study, considered the weighted contributions of α=0.85 and β=0.15, in agreement with [57]. In addition, for the ground state of ^{11}Be, the calculations provided at this stage are double scattering, therefore not considering the full calculation.

We also consider the removal of an neutron for a $p_{3/2}$ shell, assuming the ^{11}Be is described as an inert core coupled with a $1p_{3/2}$ neutron,
$|^{10}\mathrm{Be}^*(^9Be(3/2^-)\times\nu 2s_{1/2};1^-)\times\nu 1p_{3/2}>$ or $|^{10}\mathrm{Be}^*(^9\mathrm{Be}(3/2^-)\times\nu 2s_{1/2};2^-)\times\nu 1p_{3/2}>$.

For this case, it was provided the knockout full calculation. The calculated Faddeev/AGS ^{10}Be momentum distributions normalized to the unit are shown in Figure 6.8 for a valence neutron and an inner core neutron.

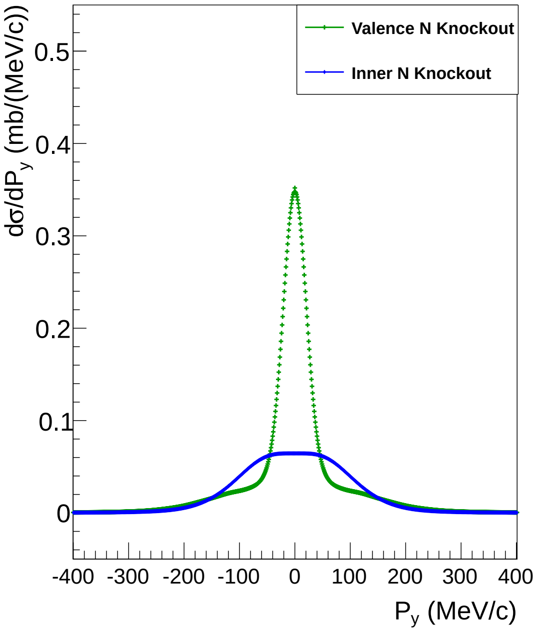

Figure 6.8: Theoretical momentum distributions for the different neutron shells of ^{11}Be. The narrow distribution is characteristic of an s-shell (green dotted line) and the broad of a p-shell (cyan colored line).

The calculated[1] single particle cross sections contributions renormalized to a spectroscopic factor of one are shown in Table 6.4. The calculations provided are double scattering for the $2s_{1/2}$ and $1d_{5/2}$ and full scattering for the knockout of the $1p_{3/2}$ neutron.

ν-shell	σ_{sp}^{theo} (mb)
$2s_{1/2}$	26.45
$1d_{5/2}$	4.28
$1p_{3/2}$	15.94

Table 6.4: Calculated Faddeev/AGS single particle cross sections for the different contributions for ^{11}Be as defined in the text.

In order to reproduce the total reaction distribution extracted from the experimental data, it is necessary to perform a weighted sum of the valence and inner core contributions,

$$\sigma_{total}^{theo} = a.\,\sigma_{valence} + b.\,\sigma_{inner}, \tag{6.2}$$

where a and b are the different weights of each contribution. Both a and b values are obtained from fitting the theoretical results to the experimental data by means of the

---

[1] performed by the theoretical group composed by E. Cravo, R. Crespo and A. Deltuva

minimization of the reduced χ^2 function. The reduced-χ^2 minimization was performed using the MIGRAD algorithm, a robust and stable minimization algorithm.

The parameters obtained were applied to the valence and inner core distributions and the total theoretical momentum differential cross section distribution was obtained. This procedure was applied to the inclusive and exclusive studies performed in this work and the results can be found in the following section.

6.4 Interpretation of Results

The study of the neutron knockout reaction of the ^{11}Be with a proton target at relativist energies was performed considering two approaches to which we named: a) inclusive neutron knockout (^{11}Be(p,X)^{10}Be) and b) exclusive neutron knockout (^{11}Be(p,pn)^{10}Be). In this section we aim to interpret the differences in the results obtained in the two approaches, mainly in the determined reaction cross section.

Experimental Momentum Distribution Widths

The first observable to be evaluated was the momentum distribution width. The work of Kelley *et al.* [56] evaluated parallel momentum distributions by means of nuclear breakup at 63 AMeV with different targets: ^{9}Be, ^{93}Nb, ^{181}Ta and ^{238}U. A mean value for the longitudinal momentum width of 43.6±1.1 MeV/c was determined as the breakup mechanism does not appear to distort the momentum distribution of the ^{10}Be core.

The momentum distribution was also evaluated by Aumann *et al.* [57] via the one neutron knockout ^{9}Be(^{11}Be,^{10}Be+γ)X reaction at 60 AMeV, a core momentum width of 45±0.6 MeV/c was obtained.

It is expected from the theoretical point of view that longitudinal or parallel momentum distributions are less perturbed by reaction mechanisms than transverse momentum distributions [103]. However, these should carry similar information except for large momentum transfer [34]. In fact, narrow momentum distributions were first observed in halo nuclei when studying perpendicular momentum distributions [43].

In this work, only the momentum distributions perpendicular to the beam direction were determined and the results for the CH$_2$ and carbon targets are shown in Table 6.5. The values obtained for the exclusive knockout reaction present a good agreement with the results found in the literature.

Momentum Width (MeV/c)				
Target	p.Inclusive	p.Exclusive	Ref. [56]	Ref. [57]
CH_2	44 ± 2	51 ± 3	43.6 ± 1.1	45.7 ± 0.6
Carbon	26 ± 3	38 ± 3		

TABLE 6.5: ^{10}Be experimental momentum widths considering ^{11}Be particle inclusive knockout (^{11}Be$(Z, X)^{10}$Be) and particle exclusive knockout (^{11}Be$(Z, pn)^{10}$Be) reactions where Z is either a CH_2 and carbon targets, and comparison to literature.

Experimental Cross Sections

The reaction cross sections for the two studies performed in this work are presented in Table 6.6 together with the data found in the literature. One would expect the values to be similar as the efficiency correction was determined and applied to the ^{11}Be$(p, pn)^{10}$Be reaction. The main source of error is the uncertainty of the 2-nucleon detection efficiency. However, the results lay inside the error bar.

The reaction cross section can only be compared to literature for the case of a nuclear breakup in a carbon target. The ^{11}Be+ C→^{10}Be +n+X reaction was studied at 70A MeV by Fukuda *et al.* [55]. The cross section obtained required the detection of the incident projectile ^{11}Be, outgoing ^{10}Be and a neutron in coincidence, and was of $93.3^{(+5.6)}_{(-10.3)}$(syst) mb. When compared to the present work this value lays very close to the 92±37 mb found for the exclusive knockout reaction.

Cross Section (mb)			
Target	p.Inclusive	p.Exclusive	Ref. [55]
Proton	52 ± 5	37 ± 15	
Carbon	189 ± 6	92 ± 37	$93.3 \pm^{(+5.6)}_{(-10.3)}\ (syst)$

TABLE 6.6: Comparison of experimental reaction cross sections of the inclusive (^{11}Be(p,X)^{10}Be) and exclusive neutron knockout (^{11}Be(p,pn)^{10}Be) reactions, on a proton and carbon targets.

Theoretical Interpretation

Using the Faddeev/AGS calculations for the different halo knockout components, both inclusive and exclusive knockout measurements were investigated. The theoretical calculations were fitted to the experimental results.

Particle Exclusive Knockout Reaction

The result of the MIGRAD minimization procedure is shown in Figure 6.9. For the exclusive knockout, with a=1.07±0.7 and b=0.44±0.5.

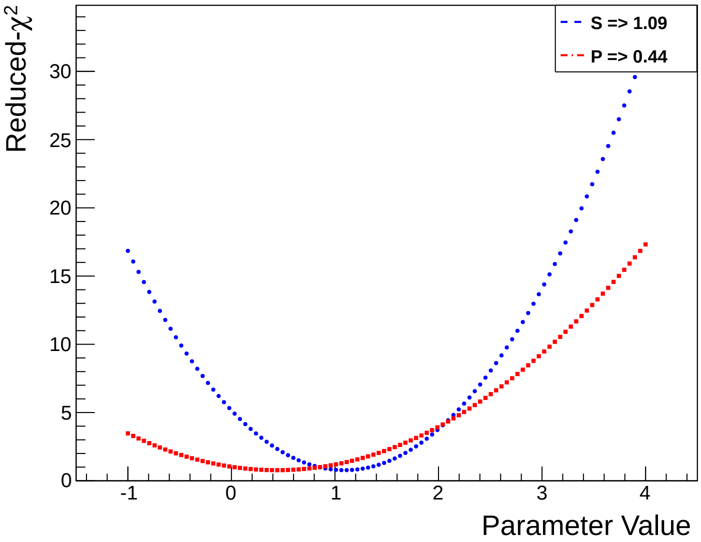

FIGURE 6.9: Correlation of the a (S) and b (P) parameters and the reduced-χ^2 function. The minimum value of a and b indicate the weight of the valence (S) and inner (P) core knockout contributions.

These parameters were applied to valence and inner core distributions and the total theoretical momentum differential cross section distribution was obtained. Figure 6.10 presents the good agreement between experiment and theory for the parameters a and b that resulted from the minimization of the χ^2 function.

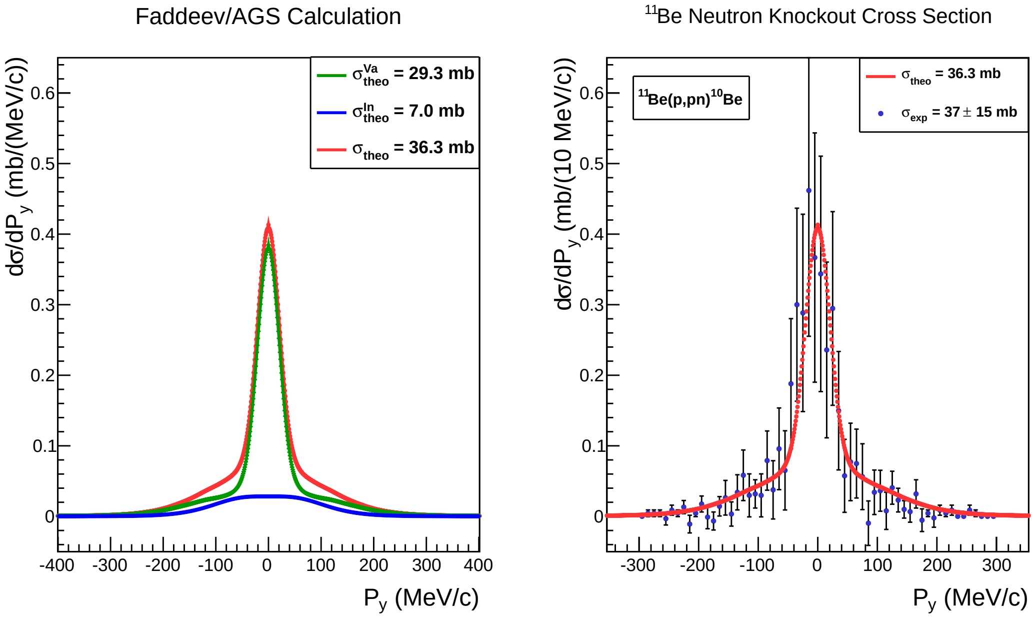

FIGURE 6.10: Theoretical interpretation of the **exclusive** neutron knockout cross section. The total theoretical cross section, result of the sum of the valence and inner core removal cross sections, describes the experimental data, revealing a not negligible contribution from a inner core removal. The calculated curves are corrected by the parameters extracted from the minimization procedure.

Based on the results of the adjustment of the theoretical curves, removing a neutron in a p state contributes to about 20% of the total cross section. Taking into account the different components calculated and used in the minimization, the spectroscopic factors for the particle exclusive knockout for the s, d and p components are α=(0.9±0.6), β=(0.2±0.1) and γ=(0.4±0.5), respectively.

Particle Inclusive Knockout Reaction

The previous procedure was also applied to study the inclusive knockout reaction. The results are shown in Figure 6.11.

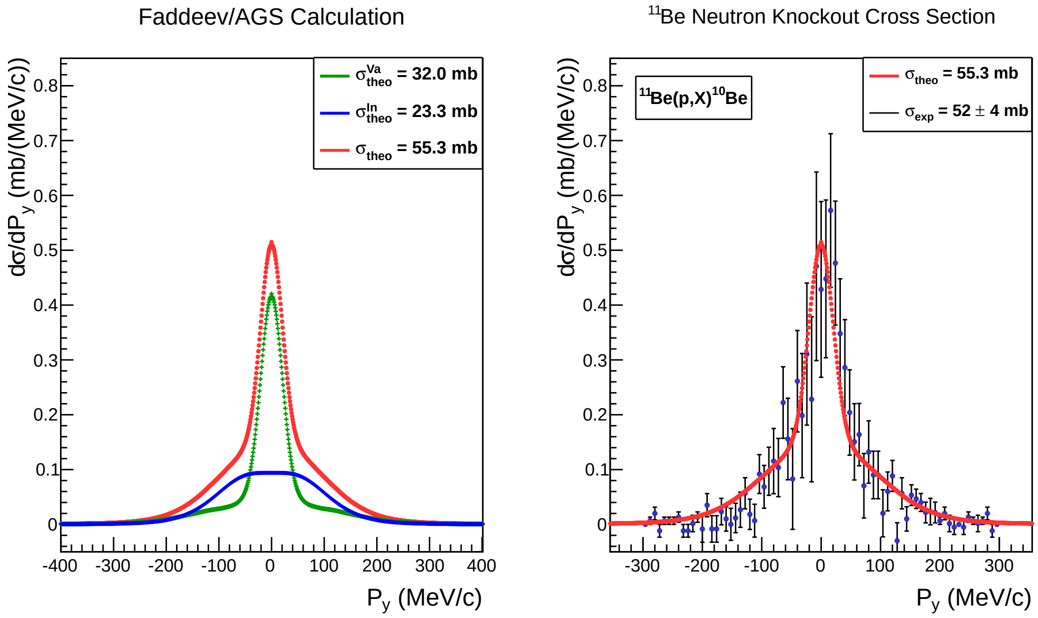

FIGURE 6.11: Theoretical interpretation of the **inclusive** neutron knockout cross section. The total theoretical cross section, result of the sum of the valence and inner core removal cross sections, describes the experimental data, revealing a strong contribution from a inner core removal.

For the inclusive knockout, however, removing a neutron from a p-state corresponds to 42% of the total cross section. Therefore, in addition to the discrepancy in the cross section value, the analysis of the heavy fragment momentum distribution of the inclusive neutron removal reaction (^{11}Be$(p, X)^{10}$Be) revealed a larger contribution of the removal of an inner core neutron.

The spectroscopic factors were also extracted for the particle exclusive knockout, α=(1.0±0.6), β=(0.2±0.2) and γ=(1.5±0.6). Between particle exclusive and inclusive knockout only the inner core contribution (γ) is affected significantly, reinforcing the considerable contribution of the removal of an inner core neutron.

A comparison of spectroscopic factors for $|^{10}\ Be(0^+) \times \nu 2s_{1/2} >$ can be found in Table 6.7 for different reactions.

Reaction	E/A (MeV)	Ref.	Spec. Factor	
			p.Inclusive	p.Exclusive
Knockout	457	Present	1.0 ± 0.6	0.9 ± 0.6
	60	[57]	0.85 ± 0.13	
Coulomb	69	[55]	0.72 ± 0.04	
	72	[49]	0.80 ± 0.20	
	520	[63]	0.61 ± 0.05	

Table 6.7: Comparison of spectroscopic factors obtained from different reactions.

The spectroscopic factors α obtained in the present study and found in the literature are listed in Table 6.7. The values reveal a discrepancy, indicating the possible dependence of the this observable on the reaction, reaction theory and model description of the ^{11}Be assumed.

Comparison between the Particle Exclusive and Inclusive Knockout Reactions

The results of the theoretical interpretation of the inclusive (Figure 8.5) and exclusive neutron knockout (Figure 8.4) cross sections are summarized in Table 6.8.

	Cross Section (mb)	
	p.Inclusive	p.Exclusive
$a \cdot \sigma_{sp}^{theo}$(valence)	32.0 (58%)	29.3 (81%)
$b \cdot \sigma_{sp}^{theo}$(inner)	23.3 (42%)	7.0 (19%)
Total^{theo}	55.3	36.3
Total^{exp}	52±5	37±15

Table 6.8: Reaction cross sections of the ^{11}Be one neutron removal (^{11}Be$(p, X)^{10}$Be) and neutron knockout (^{11}Be$(p, pn)^{10}$Be) reactions, on a proton target.

The cross section for the valence knockout is similar in both particle inclusive and exclusive measurements. The main difference resides on the dominance of the removal of a neutron from an inner shell. In the case of the neutron removal this mechanism can account for 42% of the total reaction cross section while considering a neutron knockout this accounts for 19%.

The contribution of the transfer channel was estimated using the Faddeev/AGS framework and was found to be neglible. Therefore, this channel cannot explain the difference between the measured particle inclusive and exclusive cross sections.

The analysis of the γ-ray spectrum may shed some light on this topic. It can be possible that we are excluding some information when pursuing for the detection of two nucleons in coincidence with a heavy fragment (^{11}Be(p,pn)^{10}Be).

6.5 Gamma Spectrum

To access the populated states of the ^{10}Be core after the neutron break-up, the gamma rays emitted during the reaction were measured in coincidence with the reaction fragments (2 nucleons and the ^{10}Be core). The known level scheme of ^{10}Be, depicted in Figure 6.12, has been studied in several experiments considering different energies and targets [57, 62] and theoretically described in [104].

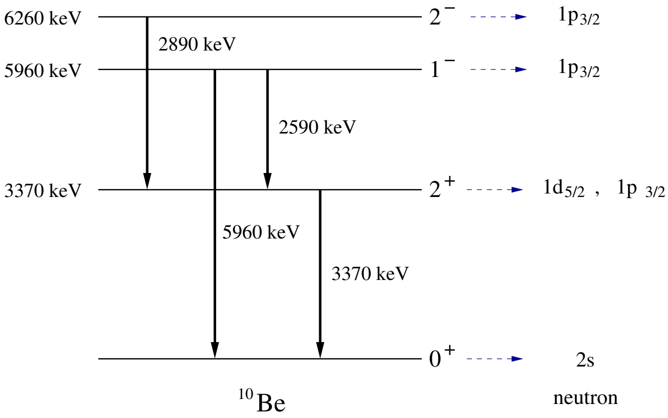

FIGURE 6.12: Picture of the main expected contributions of the level scheme of the ^{10}Be nucleus [62].

The presented level scheme indicates that the transition to the ground state is from the decay of a 2^+ state or a direct decay from the 1^- state, evidenced by a 5.96 MeV gamma ray. The 2^+ state can be fed directly revealing a neutron is emitted from a $1d_{5/2}$ state. It can also result from the cascade of two other decays, the 1^- and 2^- states, indicating the emitted neutron stemmed from the ^{10}Be core, from a $1p_{3/2}$ or $1s_{1/2}$. Therefore, the expected number of gamma rays ($2^+ \rightarrow 0^+$) should be larger than the sum of number of gamma rays from the ($2^- \rightarrow 2^+$) and ($1^- \rightarrow 2^+$) decays [105].

6.5.1 Gamma Spectrum from Exclusive Neutron Knockout

The gamma-ray spectrum measured in coincidence with the ^{10}Be core and two emitted nucleons, characterizing the ^{11}Be(p,pn)^{10}Be reaction is shown in Figure 6.13. In this figure is also drawn a fit to the background (BG), revealing the main expected decay modes, E_γ= 2.59, 2.89, 3.37 MeV.

The gamma-ray spectrum for the ^{11}Be(p,pn)^{10}Be was obtained using the low energy readout of Crystal Ball. After applying the addback algorithm and considering only four or less gamma clusters composed by a maximum of two crystals. A Doppler correction was applied to account for the velocity of the ^{10}Be core.

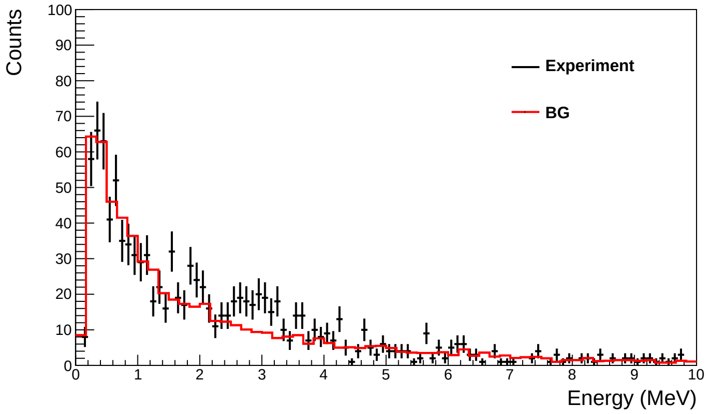

FIGURE 6.13: ^{11}Be(p,pn)^{10}Be gamma spectrum in coincidence with the detection of two nucleons in Crystal Ball and considering a CH_2 target. The background (BG) is drawn in red.

The gamma spectrum of ^{10}Be for the particle exclusive knockout considering a CH_2 target is shown in Figure 6.13. A peak can be seen around the 3 MeV region. In addition, a gamma background was fitted to the spectrum. The background was estimated as the proton and neutron contribution to the gamma spectrum. Therefore, it consists on the reconstructed gamma spectrum obtained from the (p,pn) simulations, where only the proton and neutron are directed to the Crystal Ball detector.

After performing the subtraction of the carbon contribution in the CH_2 target measurement, it was seen that the statistics were quite low. Before pursuing this issue, the gamma-ray spectrum resulting from the inclusive neutron knockout was studied.

6.5.2 Gamma spectrum from Inclusive Neutron Knockout

The gamma-ray spectrum measured in coincidence in Crystal Ball considering the ^{11}Be inclusive neutron knockout reaction (^{11}Be(p,X)^{10}Be) is presented in Figure 6.14, i.e. events leaving a signal in the low energy branch of Crystal Ball associated also with the particle inclusive neutron removal process from ^{11}Be. This study was performed in order to investigate the gamma spectrum disregarding the detection of two nucleons in the Crystal Ball forward hemisphere.

Using the low energy readout of Crystal Ball, the gamma-ray spectrum for the ^{11}Be(p,X)^{10}Be was reconstructed via the addback algorithm. Similar to the previous analysis, the reconstruction only considered four or less gamma clusters composed by a maximum of two crystals and a Doppler correction was applied to account for the relativistic velocity of the ^{10}Be heavy fragment.

In the gamma-ray spectrum for neutron removal shown in Figure 6.14 one can identify the contribution from the expected four peaks located at 2.59 ($1^-\rightarrow2^+$), 2.89 ($2^-\rightarrow2^+$), 3.37 ($2^+\rightarrow0^+$), 5.96 ($1^-\rightarrow0^+$) MeV in the polypropylene target.

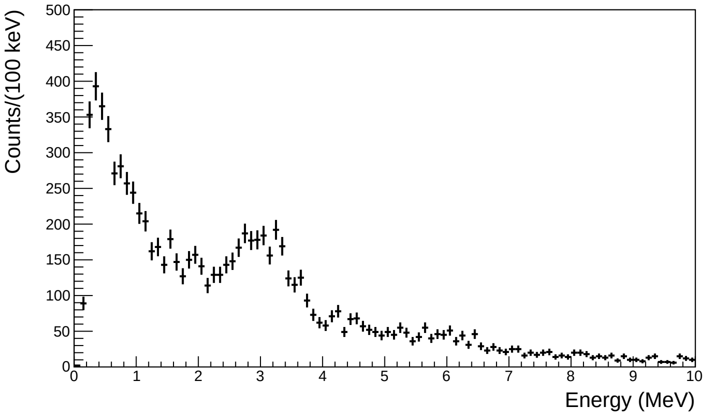

Figure 6.14: Inclusive 1-neutron removal gamma spectrum detected using Crystal Ball and considering a CH_2 target, disregarding the detection of two nucleons in Crystal Ball forward hemisphere.The background (BG) is drawn in red.

Compared to the gamma spectrum arising from the ^{11}Be(p,pn)^{10}Be reaction (Figure 6.13), there is an increase of statistics in the 3 MeV region.

This result suggests the process to remove one neutron from a inner shell, $1p_{3/2}$ results in a different reaction kinematics as the one considered in the simulations performed in this work, and that a non-negligible fraction of the events emits one of the nucleons in regions not covered by the Crystal Ball detector. The analysis of other detectors systems present in the setup like the LAND neutron detector or the proton branch detectors, shown in Figure 2.3, was beyond the scope of this work.

The subtraction of the contribution of the carbon present in the polypropylene target results in the gamma spectrum due to H_2. The result is shown in Figure 6.15.

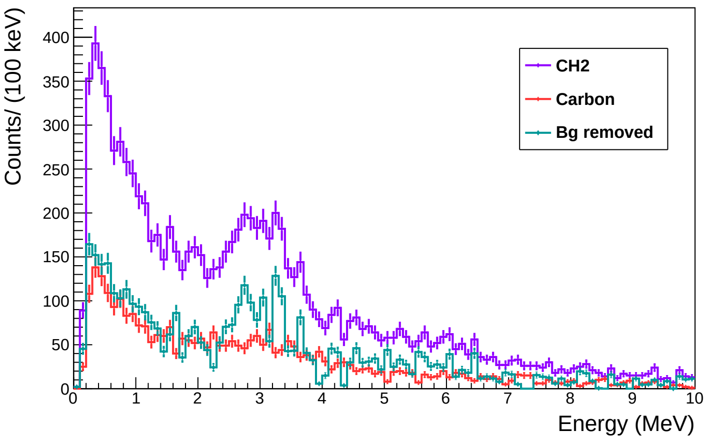

FIGURE 6.15: Inclusive 1-neutron removal gamma spectrum detected using Crystal Ball, considering a CH_2 and carbon target and background subtraction.

A reduced-χ^2 minimization was performed using the MIGRAD algorithm. The minimization was used to determine the different weights of the 2.59, 2.89, 3.37, 5.96 MeV gamma rays. These were simulated using R3BRoot. The simulations included not only the gamma rays in Crystal Ball but also the background, considered as the photons resulting from the interaction of protons and neutrons only.

The minimization was first performed taking into account the CH_2 and carbon individual spectra. After determining the number of photons measured at each state and removing the number of photons due to carbon target nuclei, the fitting parameters were extracted. These were applied and the result is shown in Figure 6.16. This procedure was adopted in order to overcome the effects of low statistics.

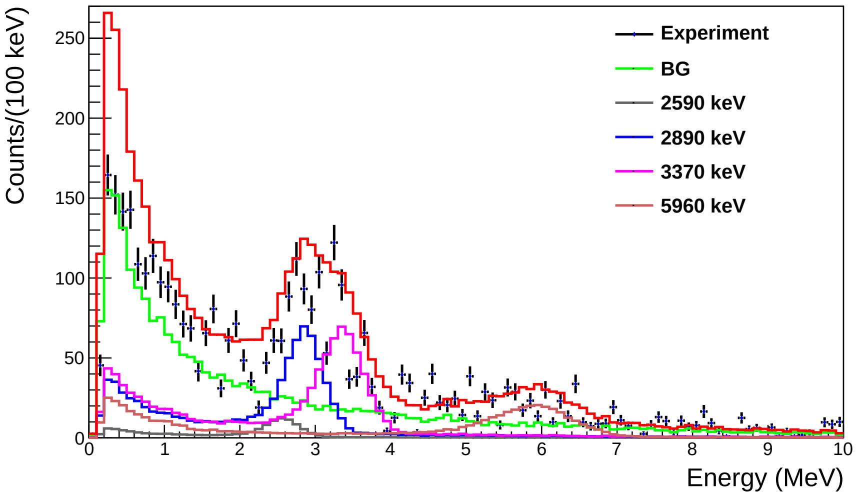

FIGURE 6.16: Inclusive 1-neutron knockout gamma energy spectrum detected using Crystal Ball.

One should notice the contribution of the ($1^- \to 0^+$) decay may be misleading and an artifact of the fitting. It must be considered carefully.

From the analysis of the different gamma decay contributions the relative intensities were determined. The values obtained in the present analysis and the values taken from the literature for the case of [104] are presented in Table 6.9. The systematic errors estimated for the intensity the present work is given by the variation of one of the χ^2.

Gamma decay	Energy (MeV)	I_γ (%) This work	I_γ (%) Ref [104]
$2^- \to 2^+$	2.89	86 ± 27	99
$1^- \to 2^+$	2.59	14 ± 68	17
$2^+ \to 0^+$	3.37	100 ± 68	100
$1^- \to 0^+$	5.96	55 ± 47	83

Table 6.9: Relative intensities of the different gamma decays for the one neutron breakup.

Similar to the results obtained previously for the ^{11}Be(p,pn)^{10}Be reaction, the direct feeding of the 2^+ state is negligible and the cascade decays that may populate the 2^+ state is dominant.

The results obtained from the relative intensities show a major contribution from the removal of an inner core neutron, corresponding to a $1p_{3/2}$ shell. This shell is expected to present a broader momentum distribution.

The differences seen for the inclusive and exclusive studies in the previous sections led us to investigate possible correlations with the emission features of the two nucleons for the exclusive knockout reaction.

6.5.3 Coplanarity study of the two emitted nucleons

The emission of the two light particles is expected to show evidence of the QFS features, the opening angle between the two nucleons peaks at about 90° and the difference in azimuthal angle (≈180°) indicates that the neutron and the proton are emitted back-to-back, in coplanarity.

In this section, we investigate the particular case of detecting two nucleons in Crystal Ball for two particular kinematic conditions: a) coplanar and b) non-coplanar emission of the nucleons emerging from the ^{11}Be(p,pn)^{10}Be reaction, the proton from the target and the neutron from the projectile.

The nucleon angular correlations of the opening angle as a function of the azimuthal angle and the gamma ray spectrum of ^{10}Be obtained in coincidence with the detection of a ^{10}Be core and two nucleons are shown in Figure 6.17a and 6.17b, respectively.

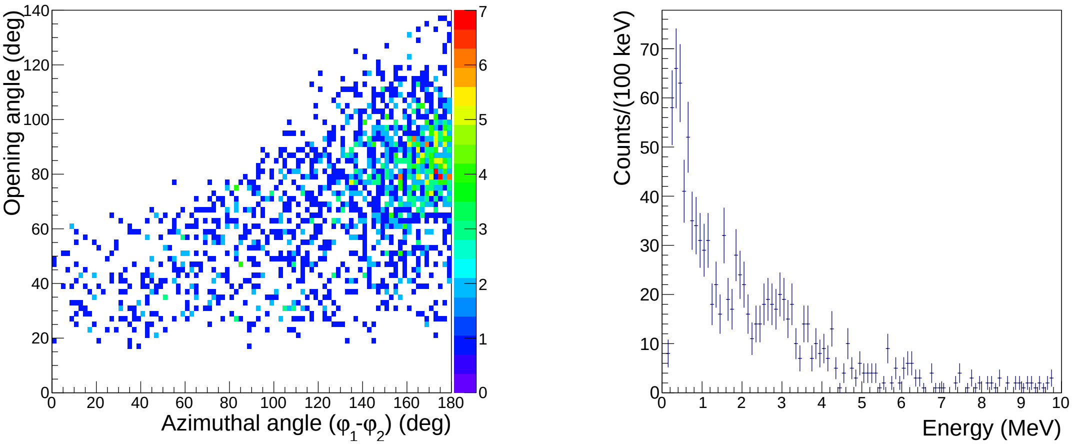

(a)

(b)

FIGURE 6.17: Angular correlation of the opening angle as a function of the azimuthal angle (a) and associated gamma spectrum (b) for the measurement of a ^{10}Be core in coincidence with two nucleons.

Two different kinematic cuts were then applied to the angular correlation plot presented in Figure 6.17a. The first considered the events that presented a strong quasi-free correlation, i.e that are inside a 2-sigma interval of the individual opening angle and azimuthal distributions as presented in Figure 6.18a. These events are characterized by the coplanar emission of the two nucleons. The other selection (non-coplanar) included all the events of the ^{11}Be(p,pn)^{10}Be reaction that lay outside the strong angular correlation as presented in Figure 6.19a. For both cases, the gamma spectra is also presented in Figure 6.18b and 6.19b.

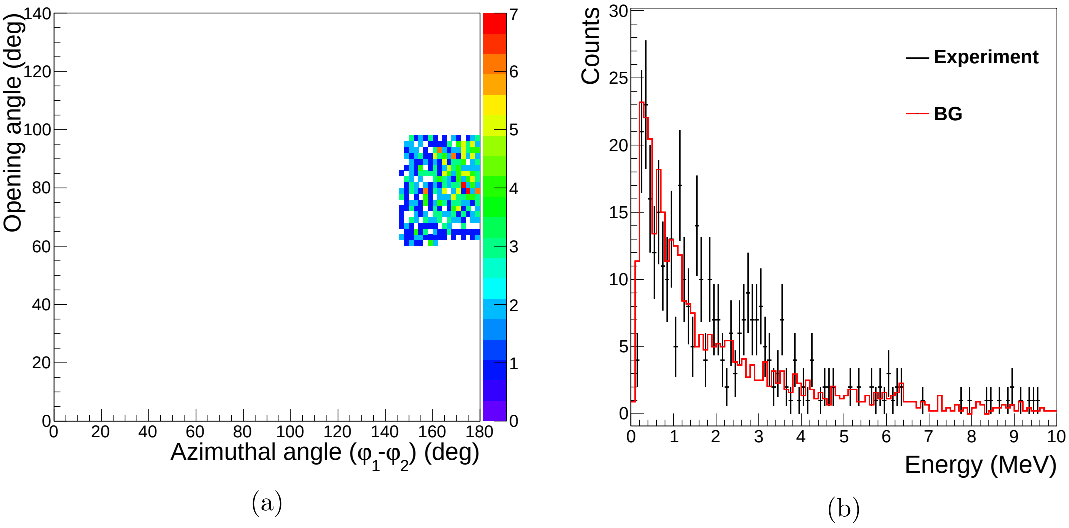

FIGURE 6.18: Angular correlation and associated gamma spectrum for the measurement of a ^{10}Be heavy fragment in coincidence with two nucleons in **coplanar** conditions. a) Tagging considered on the angular correlations of the nucleons emitted. b) Gamma spectrum measured in Crystal Ball.

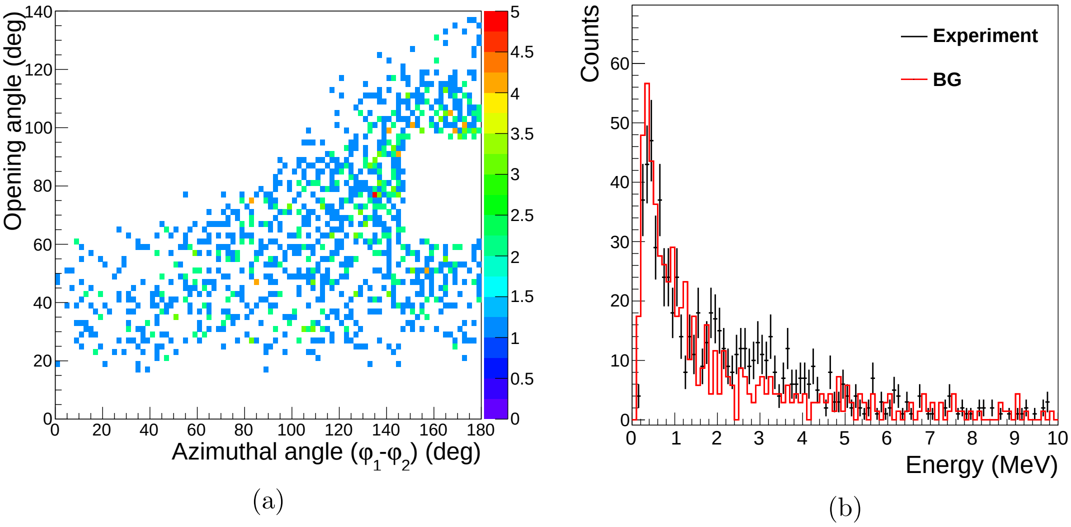

FIGURE 6.19: Angular correlation and associated gamma spectrum for the measurement of a ^{10}Be heavy fragment in coincidence with two nucleons in **non-coplanar** conditions.a) Tagging considered on the angular correlations of the nucleons emitted. b) Gamma spectrum measured in Crystal Ball.

Although the statistics are not abundant, it is possible to observe in Figure 6.18b a non-negligible contribution to the energy region around 3 MeV. This is not the case when analysing the photon spectrum for the non-coplanar emission of the two hadrons. However, the overall number of photon signals registered in the latter case is twice as much as in the coplanar case. These facts indicate that the reaction process investigated presents two clear and differentiable components even when measuring the two nucleons with Crystal Ball.

Taking into account the ^{11}Be(p,X)^{10}Be reaction in coincidence with a signal in Crystal Ball (trigger pattern tpat&8), the gamma spectrum and the associated momentum distributions are presented i) for all the events (a)and c)) ii) applying the event selection shown in Figure 6.20b (b) and d)). The cut is such that selects the major expected gamma decays (E$_{\gamma}$=2.59, 2.89 and 3.37 MeV) comprehended between 2.2 to 4.0 MeV.

From the ^{11}Be(p,X)^{10}Be reaction in coincidence with a signal in Crystal Ball, the gamma spectrum and the associated momentum distributions are presented i) for all the events (Figure 6.20a and Figure 6.20c) ii) applying the event selection shown in Figure 6.20b. The cut is such that selects the expected contribution of the main gamma decays (E$_{\gamma}$=2.59, 2.89 and 3.37 MeV) comprehended between 2.2 to 4.0 MeV.

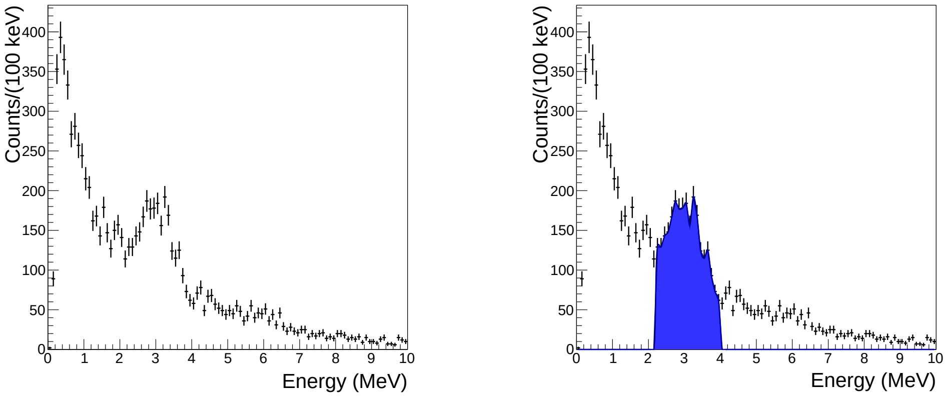

(a) Gamma spectrum, ^{11}Be(p,X)^{10}Be reaction

(b) Gamma spectrum, gamma energy tagging

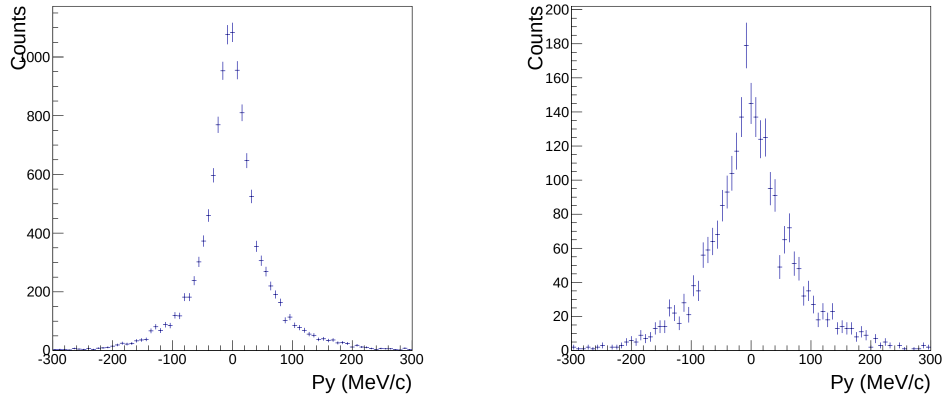

(c) Momentum distribution, ^{11}Be(p,X)^{10}Be reaction

(d) Momentum distribution, gamma energy tagging

FIGURE 6.20: Gamma spectrum of the ^{11}Be(p,X)^{10}Be reaction (a) and corresponding core momentum distribution (c) presenting a FWHM of 67.4 MeV/c. A broader heavy fragment momentum distribution (FWHM=84.4 MeV/c) (d) is observed when selecting the events that deposited 2.2-4.0 MeV in Crystal Ball (b).

Chapter 7

Conclusions

The neutron breakup of the ^{11}Be one-neutron halo nucleus has been studied in inverse kinematics at the R3B/LAND setup at the GSI-Helmholtz Centre for Heavy Ion Research (Darmstadt, Germany). The S393 experiment allowed to investigate the nuclear structure of ^{11}Be.

A primary beam of ^{40}Ar impinged on a beryllium production target, producing several lighter fragments, among them the one-neutron halo ^{11}Be. The different fragments were directed to the experimental hall. Using the time-of-flight and energy loss information provided by several detectors placed before the target, the different nuclei present in the secondary beam could be identified. Surrounding the target, the Crystal Ball detector, a 162-NaI crystal array was used for γ ray and proton detection and, a box consisting of four silicon strip detectors allowed to determine the angle of the projectile and ejectile. The later passed through the ALADIN magnet and was identified using the position, energy and time information given by silicon detectors and a time-of-flight wall.

Several targets were used in order to study different reaction channels, among them were a polypropylene target (CH_2) and a carbon target which allowed the subtraction of carbon and background in the CH_2 measurements.

After calibrating part of the setup and defining the reaction channel selection method, the analysis of the data was possible. In this work we have considered two types of analysis procedures that are related with the detected particles emerging from the collision process: (i) particle inclusive neutron knockout where only the heavy fragment is detected, ^{11}Be(p,X)^{10}Be, often referred neutron removal ^{11}Be(-1n); (ii) particle exclusive neutron knockout where the light particles and heavy fragments are detected, ^{11}Be(p,pn)^{10}Be.

First, we tackled the results stemming from the reaction in which only the projectile and heavy fragment are detected, ^{11}Be(p,X)^{10}Be. For this study the FWHM of the momentum width was determined (44±2) MeV/c for the CH$_2$ target. After the proper background subtraction of the events due to carbon, the total inclusive cross section was obtained for a proton and carbon targets, (52±5) mb and (189±6) mb, respectively.

The second approach considered the neutron knockout measured in coincidence with two nucleons, ^{11}Be(p,pn)^{10}Be, in the high energy branch of the Crystal Ball detector. The measured reaction cross section is (37±15) mb, considering a reaction efficiency of (15±6)%. This value is far from the (52±5) mb value measured when taking into account the particle inclusive neutron removal.

The detection efficiency of the proton and neutron emerging from the reaction was evaluated using the standard R^{3}B/LAND Event Generator [86] and the FairRooT [88] framework. The efficiency adopted was (15±6)%, corresponding to the standard and Bertini physics lists and the error was determined as the relative difference to the efficiency obtained from using the INCL++ physics list. In addition, some studies were performed in order to distinguish between a proton and a neutron using Crystal Ball. It was seen, that for a neutron, the number of crystals in a reconstructed cluster was much larger. No further conclusions could be taken, possibly comparing with information provided by the SSTs this subject could be further developed.

The measured and calculated cross sections were compared using the Faddeev/AGS reaction formalism assuming that other channels are negligible. This interpretation allowed to evaluate the contribution from the valence and deeply bound nucleon knockout, for both particle inclusive and exclusive measurements. For the inclusive knockout, removing a neutron from a p-state corresponds to 42% of the total cross section. Therefore, in addition to the discrepancy in the cross section value, the analysis of the heavy fragment momentum distribution of the particle inclusive neutron removal reaction (^{11}Be$(p,X)^{10}$Be) revealed a larger contribution of the removal of an inner core neutron. Nevertheless, one must point out that the cross section corresponding to the valence knockout is similar in both particle inclusive and exclusive measurements.

The previous contribution was also evident in the ^{11}Be gamma spectrum, a larger number of events around 3 MeV is clearly seen when considering the particle inclusive analysis methodology.

We have also studied the effects of emitting the two nucleons detected for the ^{11}Be(p,pn)^{10}Be reaction in co-planarity. A more clear signature of the gamma-rays stemming from the reaction was observed when the hadron were emitted back-to-back, as the number of counts in the 3 MeV region is larger. Nevertheless, the number of counts is larger in the non-coplanar case, indicating that the reaction process has two clear and differentiable components. The individual cross sections were not extracted because it was not possible to evaluate the detection efficiency in this case.

Halo nuclei such as ^{11}Be are unique systems to study the knockout of neutrons from valence and inner shells and compare particle inclusive and exclusive observables. The comparison between particle inclusive and exclusive measurements needs to be further investigated. Not only for ^{11}Be but other nuclei. It would be very interesting to investigate this issue considering the possibility to distinguish the proton and the neutron, using the Silicon detector array around the target. Also, the contributions of the two signatures of the reaction process should also be evaluated quantitatively.

Chapter 8

Synopsis

The unique features of the ^{11}Be neutron halo, a closed shell structure with an additional loosely binded neutron, allows us to study the neutron knockout of loosely bound valence and deeply bound nucleons. In this work we shall present the first experimental comparison between total cross sections and momentum distributions for particle inclusive (where only the heavy fragment is measured) and particle exclusive where light and heavy fragments are measured. The measured and calculated cross sections are compared using the Faddeev/AGS reaction formalism assuming that other channels are negligible. The study of the ^{11}Be(p,pn)^{10}Be[1] reaction was performed in inverse kinematics at 457 MeV/u at the R^{3}B setup [66] at the the GSI laboratory [64].

Experimental Setup

At the entrance of the experimental hall, the beam is characterized by several detectors which measure time, position and energy loss, allowing to distinguish the different nuclei present, among them the ^{11}Be nucleus.

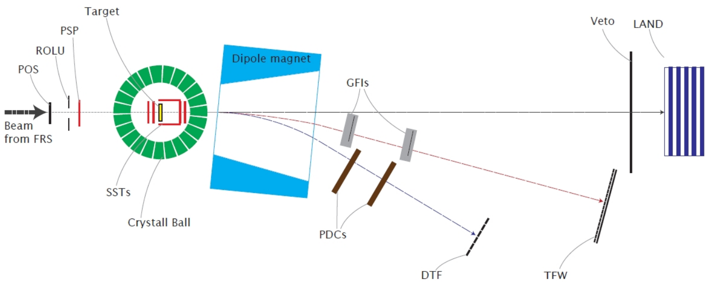

FIGURE 8.1: Schematic view of the LAND/R^{3}B setup for the S393 campaign

---

[1] For simplicity, we shall use the same notation for both direct and inverse kinematics, $A + a \rightarrow B + b$ or $A(a, b)B$.

The target is surrounded by the Crystal Ball [76], a 4π NaI gamma detector. This detector is also prepared to measure the energy deposit of scattered protons in its forward hemisphere, with respect to the beam direction. Enclosed by the Crystal Ball are eight Silicon Strip Detectors (SSTs) [77, 78] used to track charged particles. After the collision with the target, the resulting fragments (mostly focused along the direction of the beam) will go through the dipole magnet ALADIN (A Large DIpole magNet) and will be deflected according to their magnetic rigidity into different branches. Considering the production of heavy fragments, these are deflected to approximately 15° with respect to the incoming beam direction,and are detected by the GFI (Grosse FIber Detektor) detectors [79], scintillating fiber detectors used for position determination. and a scintillator TOF Wall, the TFW (Time of Flight Wall).

This work considered two types of analysis procedures that are related with the detected particles emerging from the collision process: (i) particle inclusive neutron knockout where only the heavy fragment is detected, (^{11}Be(p,X)^{10}Be), often referred neutron removal ^{11}Be(-1n); (ii) particle exclusive neutron knockout where the light particles and heavy fragments are detected, (^{11}Be(p,pn)^{10}Be). For this case, the light particles emitted from the reaction are detected using the Crystal Ball detector.

Detection Efficiency in Crystal Ball

The detection efficiency of the proton and neutron emerging from the reaction was evaluated using the standard R^{3}B/LAND Event Generator [86] and the FairRooT [88] framework. The efficiency adopted was (15.2±6.1)%, corresponding to the standard and Bertini physics lists and the error was determined as the relative difference to the efficiency obtained from using the INCL++ physics list.

Theoretical Approach

In the ^{11}Be(p,pn)^{10}Be reaction, the neutron is expected to be removed from the valence shell (s shell) or from an inner shell (p shell, associated to the ^{10}Be core) [94]. In this work we aim to compare the experimental results for the ^{10}Be momentum distributions and total cross sections with the theoretical results from the Faddeev/AGS reaction framework [95] that has been applied for the study of neutron knockout of light particles from the collision with a proton target [96–98, 100, 102, 106, 107].

Within the Faddeev/AGS formalism it is assumed that ^{11}Be is described by an inert core (either in the ground state or in a excited state) and a particle. This formalism considers on equal footing all reaction channels and takes into account all interactions within all 3 particles (Core(^{10}Be), neutron and proton) when considering a full calculation.

The ground state of ^{11}Be is assumed to be described as $|^{11}\text{Be}_{g.s.}>= \alpha\cdot\, |^{10}\text{Be}(0^+) \times \nu 2s_{1/2}> +\beta\cdot\, |^{10}\text{Be}^*(2^+) \times \nu 1d_{5/2} >$. We also consider the removal of an neutron for a $p_{3/2}$ shell, assuming the ^{11}Be is described as an inert core coupled with a $1p_{3/2}$ neutron. Figure 8.2 is a schematic representation of the possible reaction mechanism, and the corresponding calculated Faddeev/AGS ^{10}Be momentum distributions normalized to the unit are shown in Figure 8.3 for a valence neutron and an inner core neutron.

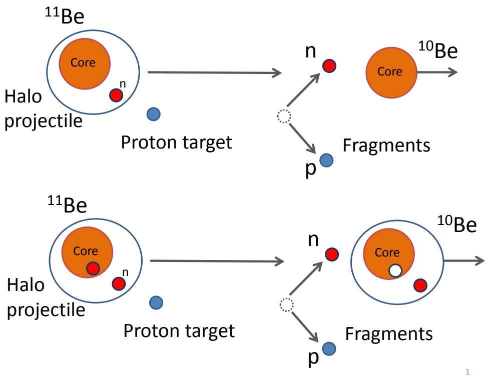

FIGURE 8.2: Schematic view of the reaction mechanism. The knocked out neutron can be from the valence shell or the inner shell.

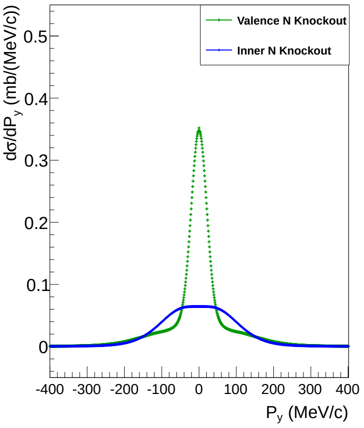

FIGURE 8.3: Theoretical curves for different neutron shells of ^{11}Be. The narrow distribution is characteristic of an s-shell and the broad of a p-shell.

Results

The study of the neutron knockout reaction of the ^{11}Be with a proton target at relativist energies was performed considering two approaches to which we named: a) inclusive neutron knockout (^{11}Be(p,X)^{10}Be) and b) exclusive neutron knockout (^{11}Be(p,pn)^{10}Be). Using the Faddeev/AGS calculations for the different halo knockout components, both inclusive and exclusive knockout measurements were investigated, and the results are shown in Figure 8.4 and Figure 8.5. The theoretical calculations were fitted against the experimental results.

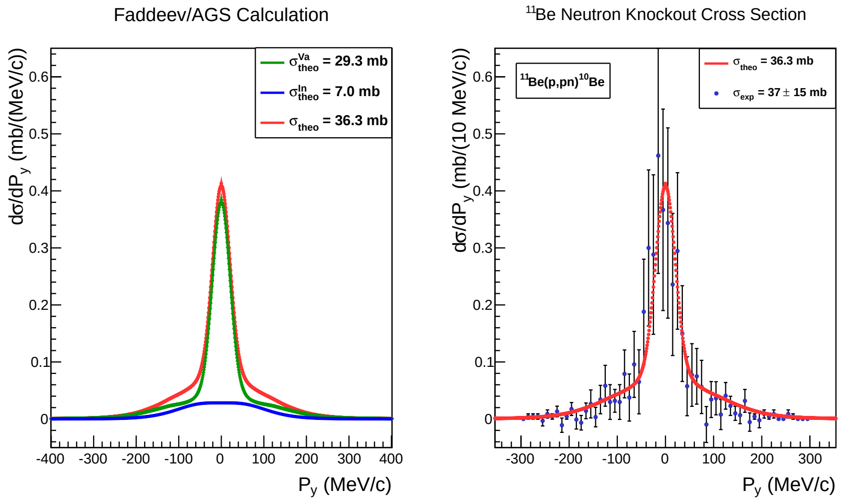

FIGURE 8.4: Theoretical interpretation of the particle **exclusive** neutron knockout cross section.

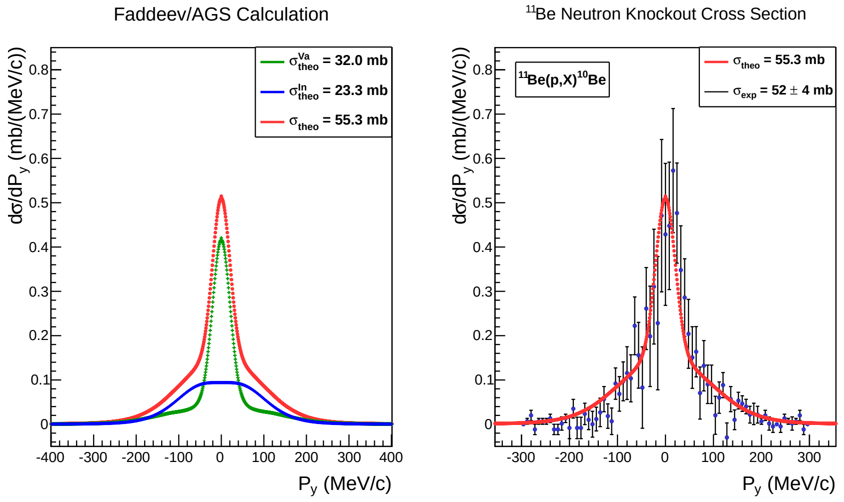

FIGURE 8.5: Theoretical interpretation of the particle **inclusive** neutron knockout cross section.

The results of the theoretical interpretation of the inclusive (Figure 8.5) and exclusive neutron knockout (Figure 8.4) cross sections are summarized in Table 8.1.

	Cross Section (mb)	
	p.Inclusive	p.Exclusive
a · σ_{sp}^{theo}(valence)	32.0 (58%)	29.3 (81%)
b · σ_{sp}^{theo}(inner)	23.3 (42%)	7.0 (19%)
Total^{theo}	55.3	36.3
Total^{exp}	52±5	37±15

TABLE 8.1: Reaction cross sections of the ^{11}Be one neutron removal (^{11}Be$(p, X)^{10}$Be) and neutron knockout (^{11}Be$(p, pn)^{10}$Be) reactions, on a proton target.

The cross section for the valence knockout is similar in both particle inclusive and exclusive measurements. The main difference resides on the dominance of the removal of a neutron from an inner shell. In the case of the neutron removal this mechanism can account for 41% of the total reaction cross section while considering a neutron knockout this accounts for 19%. The contribution of the transfer channel was estimated using the Faddeev/AGS framework and was found to be negligible. Therefore, this channel cannot explain the difference between the measured particle inclusive and exclusive cross sections.

The analysis of the γ-ray spectrum may shed some light on this topic. The reconstructed gamma spectrum of ^{10}Be is shown for the CH$_2$ target considering the particle exclusive and inclusive knockout in Figure 8.6 and Figure 8.7, respectively.

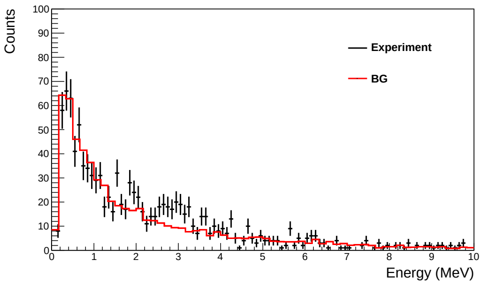

FIGURE 8.6: ^{11}Be(p,pn)^{10}Be gamma spectrum considering a CH$_2$ target. The background (BG) is drawn in red.

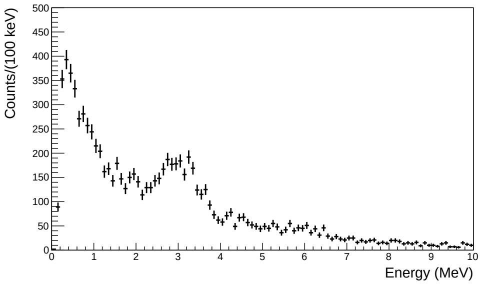

FIGURE 8.7: Inclusive 1-neutron removal gamma spectrum for a CH$_2$ target, disregarding the detection of two nucleons in Crystal Ball.

The differences seen led us to investigate possible correlations with the emission features of the two nucleons for the exclusive knockout reaction.

The emission of the two light particles is expected to show evidence of the QFS features, the opening angle between the two nucleons peaks at about ≈90° and the difference in azimuthal angle (≈180°) indicates that the neutron and the proton are emitted back-to-back, in coplanarity.

Figure 8.8 and Figure 8.9 show the results of detecting two nucleons in Crystal Ball for two particular kinematic conditions: a) coplanar and b) non-coplanar emission of the nucleons emerging from the ^{11}Be(p,pn)^{10}Be reaction, the proton from the target and the neutron from the projectile.

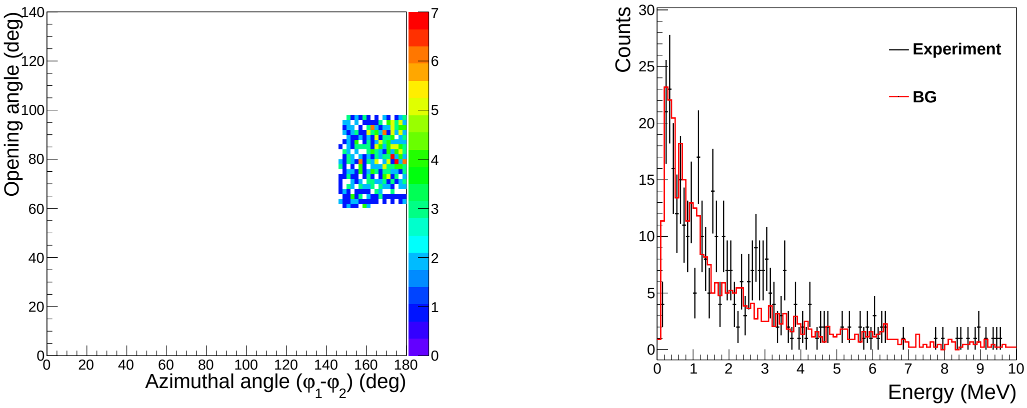

(a) (b)

Figure 8.8: Angular correlation and associated gamma spectrum for the measurement of a ^{10}Be heavy fragment in coincidence with two nucleons in **coplanar** conditions. a) Tagging considered on the angular correlations of the nucleons emitted. b) Gamma spectrum measured in Crystal Ball.

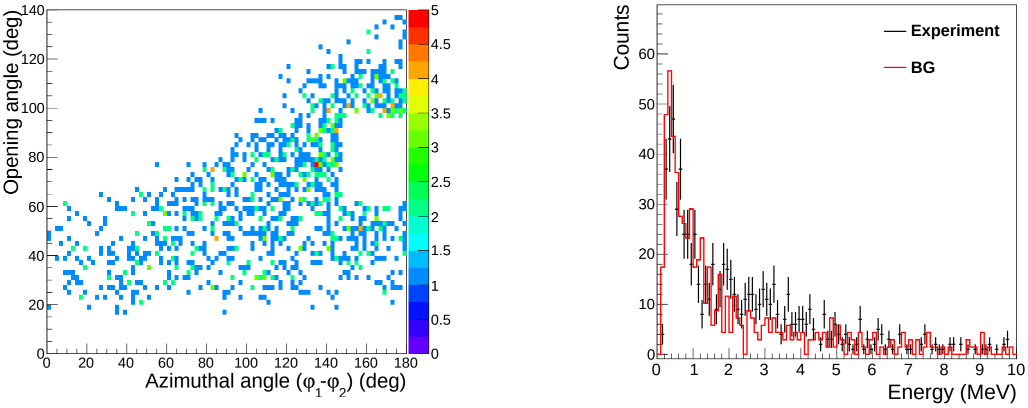

(a) (b)

Figure 8.9: Angular correlation and associated gamma spectrum for the measurement of a ^{10}Be heavy fragment in coincidence with two nucleons in **non-coplanar** conditions.a) Tagging considered on the angular correlations of the nucleons emitted. b) Gamma spectrum measured in Crystal Ball.

Although the statistics are not abundant, it is possible to observe in Figure 8.8b a non-negligible contribution to the energy region around 3 MeV. This is not the case when analysing the photon spectrum for the non-coplanar emission of the two hadrons. However, the overall number of photon signals registered in the latter case is twice as much as in the coplanar case. These facts indicate that the reaction process investigated presents two clear and differentiable components even when measuring the two nucleons with Crystal Ball. The contributions of the two signatures of the reaction process should also be evaluated quantitatively.

From the ^{11}Be(p,X)^{10}Be reaction in coincidence with a signal in Crystal Ball, the gamma spectrum and the associated momentum distributions are presented i) for all the events (Figure 8.10a and Figure 8.10c) ii) applying the event selection shown in Figure 8.10b. The cut is such that selects the major expected gamma decays (E_γ=2.59, 2.89 and 3.37 MeV) comprehended between 2.2 to 4.0 MeV.

The momentum distribution of the ^{10}Be core shown in Figure 8.10c revealed a FWHM of 67.4 MeV/c. While a broader heavy fragment momentum distribution (FWHM of 88.4 MeV/c) is observed when selecting the events that deposited 2.2-4.0 MeV in Crystal Ball gamma-ray branch, shown in Figure 6.20d. Providing the evidence of a knockout of an inner core neutron, from a $p_{3/2}$-shell.

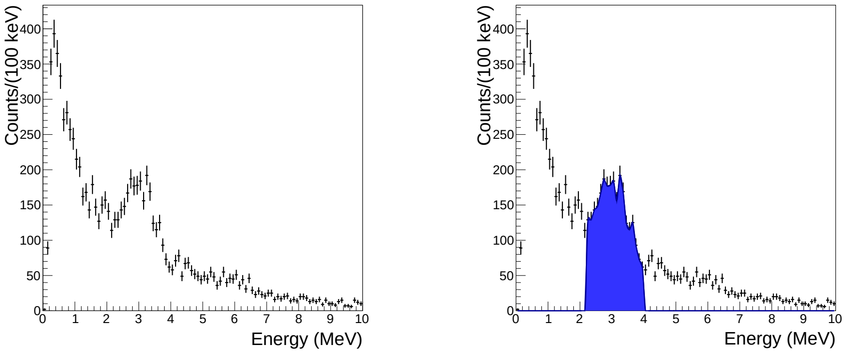

(a) Gamma spectrum, ^{11}Be(p,X)^{10}Be reaction

(b) Gamma spectrum, gamma energy tagging

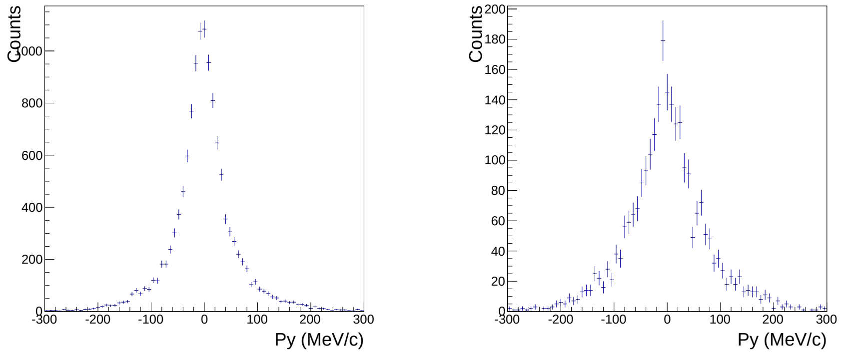

(c) Momentum distribution, ^{11}Be(p,X)^{10}Be reaction

(d) Momentum distribution, gamma energy tagging

FIGURE 8.10: Gamma spectrum of the ^{11}Be(p,X)^{10}Be reaction (a) and corresponding core momentum distribution (c) presenting a FWHM of 67.4 MeV/c. A broader heavy fragment momentum distribution (FWHM=84.4 MeV/c) (d) is observed when selecting the events that deposited 2.2-4.0 MeV in Crystal Ball (b).

The comparison between particle inclusive and exclusive measurements needs to be further investigated. Not only for ^{11}Be but other nuclei. It would be very interesting to investigate this issue considering the possibility to distinguish the proton and the neutron, using the Silicon detector array around the target.

Appendix A

Summary of studies performed on ^{11}Be

^{11}Be beam energy, MeV/u	**Target**	**Observable**	**Reference**
29.9	^{9}Be	Neutron angular dist. energy spectrum	[108]
30, 60	^{28}Si	Reaction, neutron removal σ	[109]
31, 42	C	Neutron removal σ, cluster breakup	[110, 111]
33	^{12}C,^{27}Al	Reaction σ	[53]
35-81	^{1}H	Reaction σ	[112]
38.5	^{9}Be	Neutron $P_{\parallel}$ dist.	[113]
41	^{9}Be,Ti ^{197}Au	Neutron angular distributions	[114, 115]
41	^{9}Be,^{197}Au	^{10}Be energy and angular dist., energy spectrum	[116]
41	^{48}Ti	^{10}Be energy and angular dist., energy spectrum	[62]
$\leq$60	^{28}Si	Breakup σ, neutron angular momentum dist., fragment energy and angular dist.	[117, 118]
60	^{9}Be	$P_{\parallel}$ distribution, ^{10}Be levels populated	[57, 58]
63	^{9}Be,^{27}Al ^{181}Ta,^{238}U	$P_{\parallel}$ distribution	[56]
68	Pb,C	n+^{10}Be rel. energy spectra	[46, 55, 119]
72	Pb	n+^{10}Be rel. energy dipole strength dist.	[46, 120]
520	Pb	^{10}Be$_{gs}$ spectroscopic factors dipole exc. function	[54, 63, 121, 122]
800	^{9}Be,C,^{27}Al	Interaction σ	[52]

Appendix B

Detectors measured quantities

The measured quantities in the detectors of the LAND/R^{3}B setup are summarized in Table B.1.

Detector	**Measurement**
S2 and S8	Tof measurement
PSP	Beam tracking/ ΔE measurement
PIXEL	PSP calibration
ROLU	Beam spot size accepted
POS	Tof of incoming beam
Crystal ball	E measurement for γ and protons
Silicon	Tracking (ΔE and position)
LAND	Tof of neutrons
GFI	Tracking
TFW	Tof, charge and position measurement of fragments
NTF	Tof (with TAQUILA)
Drift cambers	Trajectories of protons
DTF	Tof, charge and measurement of protons

Table B.1: Detectors and corresponding measured quantities in the LAND/R^3B setup.

Appendix C

^{11}Be Momentum Distributions

The momentum distributions of ^{11}Be were obtained for the different targets used in the S393 experiment and are presented in Figure C.1 and C.2. These distributions were obtained selecting the ^{11}Be isotope using the beam diagnostic detectors and also imposing the detection of Z=4 and A=11 (^{11}Be) in the detectors after the target, in this case, SST3, SST4 and the plastic scintillator, TFW.

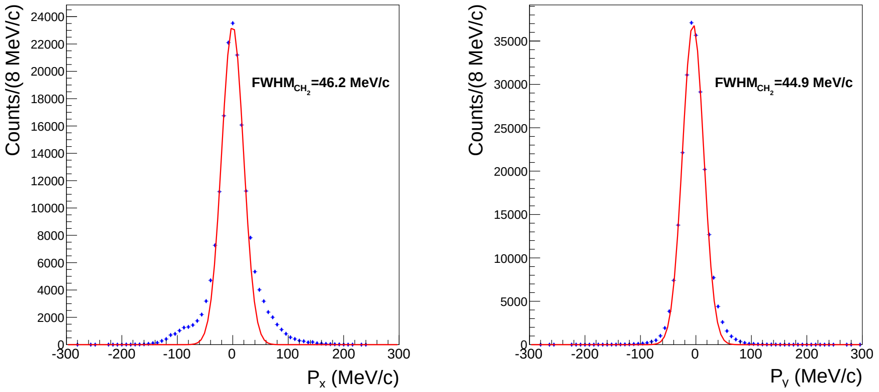

(a) CH$_2$, x-projection (b) CH$_2$, y-projection

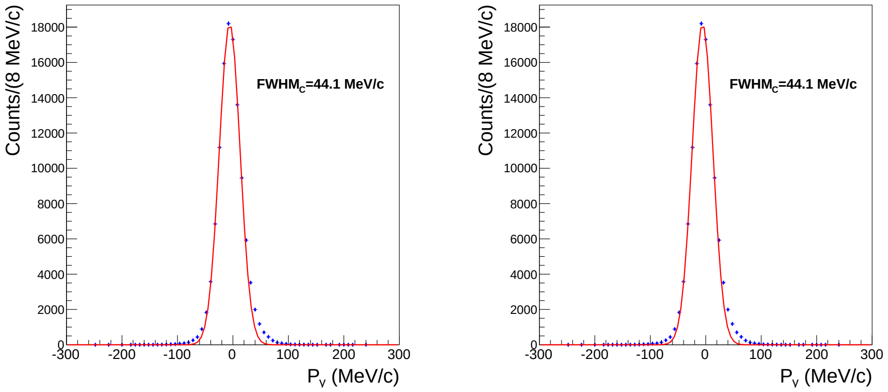

(c) Carbon, x-projection (d) Carbon, y-projection

FIGURE C.1: ^{11}Be transversal momentum distributions for the CH$_2$, carbon target runs of the ^{22}O setting. The FWHM value is also presented.

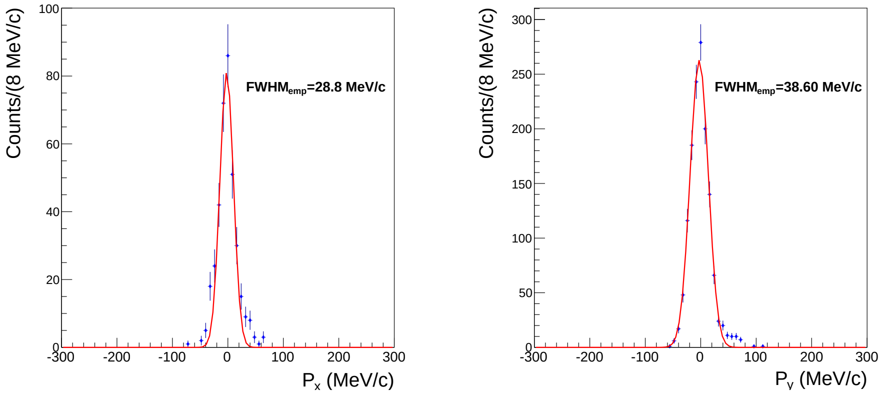

(a) Empty, x-projection

(b) Empty, y-projection

FIGURE C.2: ^{11}Be transversal momentum distributions for the empty target runs of the ^{22}O setting.

Bibliography

[1] E. Rutherford. Phil. Mag., **21**, (1911) 669–688.

[2] *http://www.nndc.bnl.gov/*. National Nuclear Data Center website.

[3] H. Bethe and R. Bacher. Rev. Mod. Phys., **8**, (1936) 82–229.

[4] M. Mayer. Phys. Rev., **74**, (1948) 235–239.

[5] E. Gapon and D. Ivanenko. Die Naturwissenschaften, **20**, (1932) 792–793.

[6] R. Woods and D. Saxon. Phys. Rev., **95**, (1954) 577–578.

[7] M. Mayer. Phys. Rev., **78**, (1950) 22–23.

[8] O. Sorlin. EPJ Web Conf., **66**, (2014) 01016.

[9] K. Wimmer, T. Kröll, R. Krücken, *et al.* Phys. Rev. Lett., **105**, (2010) 252501.

[10] A. Ozawa, T. Suzuki, and I. Tanihata. Nucl. Phys. A, **693**, 1, (2001) 32 – 62.

[11] R. Casten. Nucl. Phys. A, **693**, 1, (2001) 105 – 115.

[12] E. Warburton, J. Becker, and B. Brown. Phys. Rev. C, **41**, (1990) 1147–1166.

[13] T. Otsuka, R. Fujimoto, Y. Utsuno, *et al.* Phys. Rev. Lett., **87**, (2001) 082502.

[14] I. Tanihata, H. Hamagaki, O. Hashimoto, *et al.* Phys. Rev. Lett., **55**, (1985) 2676–2679.

[15] P. Hansen and B. Jonson. EPL (Europhysics Letters), **4**, (1987) 409.

[16] L. Chulkov, B. Jonson, and M. Zhukov. European Physical Journal A, **51**.

[17] P. Hansen and B. Sherrill. Nucl. Phys. A, **693**, (2001) 133–168.

[18] P. Hansen and J. Tostevin. Annual Review of Nuclear and Particle Science, **53**, (2003) 219–261.

[19] D. Cortina-Gil. In C. Scheidenberger and M. Pfützner, eds., *Lecture Notes in Physics, Berlin Springer Verlag*, vol. 879 of *Lecture Notes in Physics, Berlin Springer Verlag*. 183.

[20] A. Gade and T. Glasmacher. Progress in Particle and Nuclear Physics, **60**, 1, (2008) 161 – 224.

[21] G. Jacob and T. A. J. Maris. Rev. Mod. Phys., **38**, (1966) 121–142.

[22] T. Aumann, C. A. Bertulani, and J. Ryckebusch. Phys. Rev. C, **88**, (2013) 064610.

[23] R. Crespo, A. Deltuva, M. Rodríguez-Gallardo, *et al.* Phys. Rev. C, **79**, (2009) 014609.

[24] O. Chamberlain and E. Segrè. Phys. Rev., **87**, (1952) 81–83.

[25] P. Kitching, W. McDonald, T. Maris, *et al.* In J. Negele and E. Vogt, eds., *Advances in Nuclear Physics*, vol. 15 of *Advances in the Physics of Particles and Nuclei*. Springer US (1985). 43–83.

[26] P. Hansen, A. Jensen, and B. Jonson. Annual Review of Nuclear and Particle Science, **45**, (1995) 591–634.

[27] I. Tanihata. Journal of Physics G: Nuclear and Particle Physics, **22**, 2, (1996) 157.

[28] B. Jonson. In *American Institute of Physics Conference Series*, vol. 495 of *American Institute of Physics Conference Series*. 3–8.

[29] M. Zhukov. Physica Scripta, **2000**, T88, (2000) 203.

[30] J. Al-Khalili. In J. Al-Khalili and E. Roeckl, eds., *The Euroschool Lectures on Physics with Exotic Beams, Vol. I*, vol. 651 of *Lecture Notes in Physics*. Springer Berlin Heidelberg (2004). 77–112.

[31] A. Jensen, K. Riisager, D. Fedorov, *et al.* Rev. Mod. Phys., **76**, (2004) 215–261.

[32] K. Riisager. *Nuclear Halos and Experiments to Probe Them*. Springer Berlin Heidelberg, Berlin, Heidelberg (2006).

[33] K. Riisager. Physica Scripta, **2013**, T152, (2013) 014001.

[34] I. Tanihata, H. Savajols, and R. Kanungo. Progress in Particle and Nuclear Physics.

[35] I. Tanihata, H. Hamagaki, O. Hashimoto, *et al.* Phys. Lett. B, **160**, 6, (1985) 380 – 384.

[36] A. Ozawa, O. Bochkarev, L. Chulkov, *et al.* Nucl. Phys. A, **691**, 3, (2001) 599 – 617.

[37] D. Lunney, J. M. Pearson, and C. Thibault. Rev. Mod. Phys., **75**, (2003) 1021–1082.

[38] M. Smith, M. Brodeur, T. Brunner, *et al.* Phys. Rev. Lett., **101**, (2008) 202501.

[39] W. Geithner, S. Kappertz, M. Keim, *et al.* Phys. Rev. Lett., **83**, (1999) 3792–3795.

[40] T. Nilsson, G. Nyman, and K. Riisager. Hyperfine Interactions, **129**, (2000) 67–81.

[41] B. Jonson and K. Riisager. Nucl. Phys. A, **693**, 1, (2001) 77 – 89.

[42] M. Borge, L. Fraile, H. Fynbo, *et al.* J. Phys. G, **40**, (2013) 035109.

[43] T. Kobayashi, O. Yamakawa, K. Omata, *et al.* Phys. Rev. Lett., **60**, (1988) 2599–2602.

[44] N. Orr. Nucl. Phys. A, **616**, (1997) 155–168.

[45] T. Nilsson, T. Blaich, M. Borge, *et al.* EPL (Europhysics Letters), **30**, (1995) 19.

[46] T. Nakamura and N. Fukuda. Nucl. Phys. A, **738**, (2004) 283 – 287. Proceedings of the 8th International Conference on Clustering Aspects of Nuclear Structure and Dynamics.

[47] T. Otsuka, M. Ishihara, N. Fukunishi, *et al.* Phys. Rev. C, **49**, (1994) R2289–R2292.

[48] T. Kobayashi, S. Shimoura, I. Tanihata, *et al.* Phys. Lett. B, **232**, (1989) 51 – 55.

[49] T. Nakamura, S. Shimoura, T. Kobayashi, *et al.* Phys. Lett. B, **331**, (1994) 296 – 301.

[50] *http://www.nndc.bnl.gov/.* The Lund/LBNL Nuclear Data Search website.

[51] D. J. Millener, J. W. Olness, E. K. Warburton, *et al.* Phys. Rev. C, **28**, (1983) 497–505.

[52] I. Tanihata, T. Kobayashi, O. Yamakawa, *et al.* Phys. Lett. B, **206**, (1988) 592–596.

[53] M. Fukuda *et al.* Phys. Lett. B, **268**, (1991) 339–344.

[54] R. Palit, P. Adrich, T. Aumann, *et al.* Nucl. Phys. A, **738**, (2004) 45 – 51.

[55] N. Fukuda, T. Nakamura, N. Aoi, *et al.* Phys. Rev. C, **70**, (2004) 054606.

[56] J. Kelley, S. M. Austin, R. Kryger, *et al.* Phys. Rev. Lett., **74**, (1995) 30–33.

[57] T. Aumann, A. Navin, D. P. Balamuth, *et al.* Phys. Rev. Lett., **84**, (2000) 35–38.

[58] J. A. Tostevin, D. Bazin, B. A. Brown, *et al.* Phys. Rev. C, **66**, (2002) 024607.

[59] R. Crespo, A. Deltuva, and A. M. Moro. Phys. Rev. C, **83**, (2011) 044622.

[60] A. M. Moro and R. Crespo. Phys. Rev. C, **85**, (2012) 054613.

[61] K. Schmitt, K. Jones, A. Bey, *et al.* Phys. Rev. Lett., **108**, (2012) 192701.

[62] V. Lima, J. Scarpaci, D. Lacroix, *et al.* Nucl. Phys. A, **795**, (2007) 1 – 18.

[63] R. Palit *et al.* Phys. Rev. C, **68**, (2003) 034318.

[64] *http://www.gsi.de/.* GSI Helmholtzzentrum für Schwerionenforschung GmbH website.

[65] T. Aumann. *Neutron-rich nuclei at and beyond the dripline in the range z=4 to z=10 studied in kinematically complete measurements of direct reactions at relativistic energies* (2009).

[66] *http://www-land.gsi.de.* Land Collaboration website.

[67] C. Caesar, J. Simonis, T. Adachi, *et al.* Phys. Rev. C, **88**, (2013) 034313.

[68] C. Caesar. *Beyond the Neutron Drip-Line: Superheavy Oxygen Isotopes.* Ph.D. thesis, Technische Universität Darmstadt (2012).

[69] A. Najafi. *Quasi-free proton and neutron knockout reactions in* ^{20}O. Ph.D. thesis, University of Groningen (2013).

[70] P. Fernndez. *An investigation into quasi-free scattering of light neutron-rich nuclei around N=14.* Ph.D. thesis, Universidade de Santiago de Compostela (2013).

[71] M. Holl. *Quasi-Free Scattering from Relativistic Neutron-Deficient Carbon Isotopes.* Ph.D. thesis, Technische Universität Darmstadt (2014).

[72] M. Heine. *Measurement of (n,γ)-Rates of Light Neutron-Rich Nuclei for the r-Process Nucleosynthesis.* Ph.D. thesis, Technische Universität Darmstadt (2015).

[73] G. Ribeiro. *Studies Beyond the Neutron Dripline using Quasifree (p,2p) reactions: the case of 13Be.* Ph.D. thesis, CSIC - Instituto de Estructura de la Materia (2015).

[74] H. Geissel. NIM B, **70**, (1992) 286–297.

[75] K. Olive *et al.* Chin. Phys. C, **38**, (2014) 090001.

[76] V. Metag. Proc. Geiger Memorial Meeting.

[77] J. Alcaraz, B. Alpat, G. Ambrosi, *et al.* NIM A: Accelerators, Spectrometers, Detectors and Associated Equipment, **593**, 3, (2008) 376 – 398.

[78] P. Zuccon. NIM A: Accelerators, Spectrometers, Detectors and Associated Equipment, **596**, (2008) 74 – 78. Proceedings of the 8th International Conference on Large Scale Applications and Radiation Hardness of Semiconductor Detectors.

[79] J. Cub. NIM A, **402**, (1998) 67–74.

[80] T. Blaich. NIM A, **314**, (1992) 136–154.

[81] K. Mahata, H. Johansson, S. Paschalis, *et al.* NIM A: Accelerators, Spectrometers, Detectors and Associated Equipment, **608**, (2009) 331.

[82] H. Johansson. *Hunting Tools Beyond the Driplines Performing large-scale nuclear physics experiments.* Ph.D. thesis, Chalmers University of Technology (2010).

[83] R. Brun and F. Rademakers. NIM A: Accelerators, Spectrometers, Detectors and Associated Equipment, **389**, 1-2, (1997) 81 – 86. New Computing Techniques in Physics Research V.

[84] J. Alcaraz, B. Alpat, G. Ambrosi, *et al.* NIM A: Accelerators, Spectrometers, Detectors and Associated Equipment, **593**, 3, (2008) 376 – 398.

[85] F. Wamers. *Quasi-Free-Scattering and One-Proton-Removal Reactions with the Proton-Dripline Nucleus 17Ne at Relativistic Beam Energies.* Ph.D. thesis, Institut fuer Kernphysik Technische Universitaet Darmstadt (2011).

[86] V. Panin. *Fully exclusive measurements of quasi-free single-nucleon knockout reactions in inverse kinematics.* Ph.D. thesis, Technische Universität, Darmstadt (2012).

[87] R. Crespo, E. Cravo, and A. Deltuva. Submitted for publication (2016).

[88] *https://fairroot.gsi.de/.* FairRoot website.

[89] J. A. et al. NIM A: Accelerators, Spectrometers, Detectors and Associated Equipment, **835**, (2016) 186 – 225.

[90] M. Asai, A. Dotti, M. Verderi, *et al.* Annals of Nuclear Energy, **82**, (2015) 19 – 28. Joint International Conference on Supercomputing in Nuclear Applications and Monte Carlo 2013, {SNA} + {MC} 2013. Pluri- and Trans-disciplinarity, Towards New Modeling and Numerical Simulation Paradigms.

[91] S. Qingbiao. *Systematics of nucleon-nucleon total, elastic and inelastic scattering cross sections and elastic scattering angular distributions up to 10 gev.* Tech. rep., China Nuclear Information Centre, Beijing (China) (2000).

[92] A. J. Hartzler and R. T. Siegel. Phys. Rev., **185**, 95.

[93] Geant4 Users' Documents. *Physics Reference Manual*, 10.2 ed. (2015).

[94] W. A. Peters *et al.* Phys. Rev. C, **83**, (2011) 057304.

[95] L. Faddeev. Theor. Fiz., **1459**.

[96] A. Deltuva, A. M. Moro, E. Cravo, *et al.* Phys. Rev. C, **76**, (2007) 064602.

[97] R. Crespo, E. Cravo, A. Deltuva, *et al.* Phys. Rev. C, **76**, (2007) 014620.

[98] R. Crespo, A. Deltuva, E. Cravo, *et al.* Phys. Rev. C, **77**, (2008) 024601.

[99] E. Cravo, R. Crespo, A. Deltuva, *et al.* Phys. Rev. C, **79**, (2009) 064610.

[100] R. Crespo, A. Deltuva, M. Rodríguez-Gallardo, *et al.* Phys. Rev. C, **79**, (2009) 014609.

[101] E. Cravo, R. Crespo, A. M. Moro, *et al.* Phys. Rev. C, **81**, (2010) 031601.

[102] R. Crespo, M. Rodríguez-Gallardo, A. M. Moro, *et al.* Phys. Rev. C, **83**, (2011) 054613.

[103] M. Zhukov, Y. Parfenova, and J. Vaagen. Physics of Atomic Nuclei, **65**, 4, (2002) 746–751.

[104] D. Tilley, J. Kelley, J. Godwin, *et al.* Nucl. Phys. A, **745**, 3, (2004) 155 – 362.

[105] J. Al-Khalili and K. Arai. Phys. Rev. C, **74**, (2006) 034312.

[106] M. Arnould and S. Goriely. Phys. Rep., **384**.

[107] M. Arnould, S. Goriely, and K. Takahashi. Physics Reports, **450**, (2007) 97 – 213.

[108] S. Grévy, L. Axelsson, J. C. Angélique, *et al.* Nucl. Phys. A, **650**, (1999) 47–61.

[109] R. E. Warner, M. H. McKinnon, J. S. Needleman, *et al.* Phys. Rev. C, **64**, (2001) 044611.

[110] N. I. Ashwood and M. Freer. Phys. Lett. B, **580**, (2004) 129–136.

[111] M. Freer and N. Ashwood. Nucl. Phys. A, **738**, (2004) 10 – 16.

[112] A. de Vismes *et al.* Nucl. Phys. A, **706**, (2002) 295–312.

[113] L. Axelsson, J. Anglique, R. Anne, *et al.* Nucl. Phys. A, **679**, 3, (2001) 215 – 230.

[114] R. Anne *et al.* Phys. Lett. B, **304**, (1993) 55–59.

[115] R. Anne *et al.* Nucl. Phys. A, **575**, 1, (1994) 125–154.

[116] J. Bush, P. Hausladen, D. Balamuth, *et al.* Phys. Rev. Lett., **81**, (1998) 61–64.

[117] F. Negoita *et al.* Phys. Rev. C, **59**, (1999) 2082–2096.

[118] N. Skobelev. Bull RusAcad SciPhys, **63**, (1999) 014609.

[119] T. Nakamura, N. Fukuda, N. Aoi, *et al.* Nucl. Phys. A, **722**, (2003) 301 – 307.

[120] T. Nakamura, S. Shimoura, T. Kobayashi, *et al.* Nucl. Phys. A, **588**, (1995) 81 – 84.

[121] T. Aumann, A. Leistenschneider, U. D. Pramanik, *et al.* Nucl. Phys. A, **687**, 1, (2001) 103 – 110.

[122] R. Palit, P. Adrich, T. Aumann, *et al.* Nucl. Phys. A, **731**, (2004) 235 – 248.

Acknowledgements

I would like to thank all the people who contributed in some way to the work described in this thesis. First and foremost, I thank my supervisor, Professor Daniel Galaviz. I have been working with his group in Lisbon since 2009. I would like to thank for the opportunities given, the advice, the support for all this years. I am also thankful for always encouraging to question everything. I am grateful for all the patience, for all the "hours of physics"! Additionally, I would like to thank my co supervisor Professor Raquel Crespo for always showing interest and giving extra motivation for my work. I greatly appreciate the theoretical discussions and the mediation with the rest of the theory group.

Every result described in this thesis was accomplished with the help and support of the group colleagues Pamela Teubig and Paulo Velho. Although their path only crossed mine for a while, I can not forget to thank Jorge Machado, André Ornelas, Pablo Cabanelas and Angel Benitez.

I really appreciated the discussions with the theoretical group and their effort in providing calculations for my particular case of study. I greatly benefit from the collaboration with Arnas Deltuva and Edgar Cravo.

I would like to thank the various members of the R3B collaboration which were always open to discuss this work and others.

Por fim, gostaria de agradecer à minha família e aos meus amigos que me apoiaram durante este tempo todo. Em primeiro lugar à minha mãe, pai e irmão que serão sempre o meu apoio e a quem eu dedico este trabalho. Agradeço também aos meus amigos que sempre estiveram ao meu lado e tiveram palavras de encorajamento que nunca esquecerei: André Ornelas, Cláudia Santos, Andreia Cardoso, Catarina Duarte, Miriam Moreno. A amigos que sempre me souberam resgatar quando necessário: Sílvia Lopes, Sofia Silva e Suse Fernandes.

Quero ainda agradecer aos meus colegas e amigos do IPO. Receberam-me de braços abertos, ensinaram-me muito e fazem-me sentir parte de uma equipa todos os dias.